Alejandra Cristina Rueda Urdaneta

Critical temperature of welded 25Cr duplex stainless steel in seawater

Master's thesis in Chemical Engineering and Biotechnology
Supervisor: Otto Lunder
Co-supervisor: Roy Johnsen

June 2019

Master's thesis

NTNU

Norwegian University of
Science and Technology

Alejandra Cristina Rueda Urdaneta

Critical temperature of welded 25Cr duplex stainless steel in seawater

NTNU

Norwegian University of
Science and Technology

Preface

This master's thesis was carried out at the Department of Materials Science and Engineering in the Norwegian University of Science and Technology (NTNU) as a culmination of the integrated master's degree Chemical Engineering and Biotechnology. The work was done in collaboration with Statens vegvesen (Norwegian Public Roads Administration) for the bridge crossing at Bjørnafjorden as a part of the project Coastal Highway Route E39. The project was supervised by Professor Roy Johnsen[1], Professor Otto Lunder[2], Ole Øystein Knudsen[3], and Rune Pedersen[4].

The work has been performed by the author, with the exception of the XPS experimental work, which was carried out and analyzed by Amin Hossein Zavieh[5], the SEM, EDS and BSE imaging, which was performed by the author and assisted by Cristian Torres Rodríguez[1], and the EBSD imaging, which was performed by the author and assisted by Nousha Kheradmand[1]. The experimental work was performed at the Department of Mechanical and Industrial Engineering at NTNU, except for the XPS which was performed at NTNU Nano Lab.

Trondheim, Norway
25.06.2019

Alejandra Cristina Rueda Urdaneta

---

[1]Department of Mechanical and Industrial Engineering, NTNU
[2]Department of Materials Science and Engineering, NTNU
[3]SINTEF Industri
[4]Statens Vegvesen
[5]NTNU NanoLab

Acknowledgements

Abstract

The Norwegian Public Roads Administration (NPRA) is planning to build the world's longest pontoon bridge to cross Bjørnafjorden as a part of the project Coastal Highway Route E39. One of the favored design alternatives involves carbon steel pontoons with a 25Cr super duplex stainless steel (SDSS) section surrounding the pontoon in the splash zone. It is important that the right materials are used in the bridge to fulfill its required lifetime of 100 years. Although SDSS is a strong material with excellent corrosion resistance, its temperature limits in seawater are still a subject of debate. In addition, other design specifications such as welding, coatings and cathodic protection (CP) further challenge the material in this environment.

The aim of this thesis is to determine the effect of welding on the corrosion resistance of SDSS in seawater, focusing on critical corrosion temperature (T_{crit}). In order to do so, a literature survey summarizing previous work on the corrosion properties of SDSS base material in marine/seawater environments was presented together with a review of literature on the T_{crit} of welded SDSS in seawater. Experimental work was also carried out to determine the T_{crit} of welded SDSS in natural seawater, as well as how it is affected by different surface conditions, welding procedures and potential polarization of the sample. Therefore, critical corrosion temperature tests partially based on the ASTM G150 standard were carried out in natural seawater, where TIG- or laser-welded samples, pickled or not pickled, bare or coated, were either exposed at OCP or polarized to +400 mV vs. Ag/AgCl (simulating the presence of biofilm on the surface). In the same tests, after corrosion initiation, the temperature was decreased to determine the repassivation temperature of the samples. Some samples were also pre-cathodically polarized to -1100 mV vs. Ag/AgCl for a week to simulate the effects of disconnecting CP during service. Long term exposure tests in natural seawater at 40 °C with coated welded samples, pickled or not, at OCP or anodically polarized to +400 mV vs. Ag/AgCl were also carried out to further assess the T_{crit} of the welded samples and the effect of anodic polarization and pickling. Additionally, the nature of the corrosion attacks was characterized with a scanning electron microscope (SEM) and with energy-dispersive X-ray spectroscopy (EDS). The quality of the TIG-welds was characterized by investigating the presence of deleterious phases with SEM-backscattered electron (BSE), and by examining the distribution of the different phases in the different areas of the welded sample with electron backscatter diffraction (EBSD). In addition, the passive layer of TIG-welded samples, pickled or not, was characterized with X-ray photoelectron spectroscopy (XPS) in order to assess the effect of welding and pickling on the passive layer of SDSS.

The literature survey suggests welded SDSS have T_{crit} between 40 and 50 °C according to laboratory tests, while experiences in seawater environments suggest that welded SDSS can still corrode in an environment similar to Bjørnafjorden. As for the experimental work, the long-term exposure test showed that 40 °C is a safe temperature for pickled coated welds at OCP but it is not a safe temperature for any coated welded sample polarized anodically. In addition, the critical corrosion temperature tests and the long-term exposure tests indicate the T_{crit} of the welded samples were highly affected by anodic polarization, pickling and the introduction of crevices formed by the coating. Furthermore, pre-cathodic polarization in seawater was shown to have the largest deleterious effect on T_{crit}, causing the samples to initiate corrosion at 24 °C.

Some samples did not manage to repassivate during the critical temperature tests as the seawater temperature was decreased from T_{crit} to 23 °C. Propagation of corrosion at low temperatures and disconnecting CP during service are thus the most crucial aspects for application at Bjørnafjorden.

The characterization of the corrosion attacks with SEM showed that the attacks were not phase-selective, and the EDS analysis showed that the corrosion-attacked sites were able to build a highly resistant passive layer upon repassivation. Moreover, the BSE, EBSD and XPS characterizations showed that the TIG-welds were of good quality, so even lower T_{crit} than the ones determined in the present work can be achieved if the welding parameters are not chosen appropriately.

Sammendrag

Statens Vegvesen planlegger å bygge verdens lengste flytebro over Bjørnafjorden som en del av Ferjefri E39-prosjektet. En av de foretrukne alternativene involverer karbonstål-pontonger med et belte rundt skvalpesonen laget av 25Cr super dupleks rustfritt stål (SDSS). Det er avgjørende at de rette materialene blir brukt for å oppfylle kravet om 100 års levetid. Selv om SDSS er et sterkt materiale med utmerket korrosjonsresistanse, er temperaturgrensene i sjøvann fortsatt et tema som er oppe til debatt. Dessuten er andre designspesifikasjoner som sveising, belegg og katodisk beskyttelse (CP) utfordringer for materialet i et slikt miljø.

Hensikten med denne oppgaven er å fastslå effekten av sveising på korrosjonsbestandigheten til SDSS i sjøvann, med fokus på kritisk korrosjonstemperatur (T_{crit}). For å gjøre det, har en litteraturundersøkelse som oppsummerer tidligere arbeid på korrosjonsegenskapene til SDSS grunnmateriale i marine omgivelser og sjøvannsomgivelser, blitt presentert sammen med en undersøkelse av litteratur om den kritiske korrosjonstemperaturen til sveiset SDSS i naturlig sjøvann, i tillegg til hvordan det blir påvirket av ulike overflateforhold, sveiseprosedyrer og potensialpolarisering av prøven. Tester av kritisk korrosjonstemperatur delvis basert på ASTM G150 standarden ble derfor gjort i naturlig sjøvann hvor TIG- eller lasersveisede prøver, beiset eller ikke, med eller uten belegg, ble eksponert ved OCP eller polarisert til +400 mV vs. Ag/AgCl (for å simulere tilstedeværelsen av biofilm på overflaten). I de samme testene, etter korrosjonsinitiering, ble temperaturen senket for å fastslå repassiveringstemperaturen til prøvene. Noen prøver ble også pre-katodisk polarisert til -1100 mV vs. Ag/AgCl i en uke for å simulere effektene av å koble fra CP under levetiden. Langtidseksponering av tester i naturlig sjøvann ved 40 °C med sveisede prøver med belegg, beisede eller ikke-beisede, ved OCP eller anodisk polarisert til +400 mV vs. Ag/AgCl, ble også utført for å videre vurdere T_{crit} av de sveisede prøvene og effekten av anodisk polarisasjon og beising. I tillegg ble typen korrosjonsangrep karakterisert med et skanning elektronmiskroskop (SEM) og med energidispersiv røntgenspektroskopi (EDS). Kvaliteten på TIG-sveisene ble karakterisert ved å undersøke forekomsten av skadelige faser med SEM-tilbakespredte elektroner (BSE) og ved å undersøke fordelingen av ulike faser i de ulike områdene av sveiseprøven med diffraksjon av tilbakespredte elektroner (EBSD). I tillegg ble det passive sjiktet av TIG-sveisede prøver, beisede eller ikke, karakterisert ved røntgenfotoelektronspektroskopi (XPS) for å vurdere effekten av sveising og beising på det passive sjiktet av SDSS.

Litteraturundersøkelsen antyder at sveiset SDSS har en T_{crit} på mellom 40 og 50 °C i følge laboratorietester, mens erfaringer fra sjøvannomgivelser antyder at en sveiset SDSS fortsatt kan korrodere i omgivelser som ligner Bjørnafjorden. Når det gjelder det eksperimentelle arbeidet, viste langtidseksponeringstestene at 40 °C var en trygg temperatur for beisede sveiser med belegg ved OCP, men ikke for noen av de sveisede prøvene med belegg som var anodisk polarisert. I tillegg indikerer de kritiske korrosjonstemperaturtestene og langtidseksponeringstestene at T_{crit} av de sveisede prøvene ble svært påvirket av anodisk polarisasjon, beising og tilstedeværelsen av spalter dannet av belegget. Dessuten ble det vist at pre-katodisk polarisasjon i sjøvann hadde størst skadelig effekt på T_{crit}, som gjorde at prøvene initierte korrosjon ved 24 °C.

Noen prøver repassiverte ikke under de kritiske temperaturtestene ved avkjøling fra T_{crit} til 23 °C. Korrosjonspropagering ved lave temperaturer og frakobling av CP under levetiden er derfor de mest avgjørende aspektene for bruk ved Bjørnafjorden.

Karakteriseringen av korrosjonsangrepene ved SEM viste at angrepene ikke var fase-selektive og EDS-analysen viste at de korrosjonsangrepne områdene utviklet et resistant passivt sjikte ved repassivering. Videre viste EBSD-, BSE- og XPS-karakterisering at TIG-sveiser var av god kvalitet slik at ennå lavere T_{crit} enn de bestemt i nåværende arbeid kan oppnås hvis sveiseparameterne ikke er valgt rett.

Contents

List of Tables

List of Figures

Abbreviations

ASS	=	Austenitic Stainless Steel
BSE	=	Backscattered Electron
CCT	=	Critical Crevice corrosion Temperature
CE	=	Counter Electrode
CP	=	Cathodic Protection
CPT	=	Critical Pitting corrosion Temperature
DSS	=	Duplex Stainless Steel
EBSD	=	Electron Backscatter Diffraction
EDS	=	Energy Dispersive X-ray Spectroscopy
FSS	=	Ferritic Stainless Steel
GTAW	=	Gas-Tungsten Arc Welding
HAZ	=	Heat Affected Zone
IFM	=	Infinite Focus Microscope
MMA	=	Manual Metal Arc
NPRA	=	Norwegian Public Roads Administration
OCP	=	Open Circuit Potential
PRE_N	=	Pitting Resistance Equivalent
PRE_N*	=	Modified Pitting Resistance Equivalent
PWHT	=	Post Weld Heat Treatment
RE	=	Reference Electrode
SCC	=	Stress Corrosion Cracking
SCE	=	Saturated Calomel Electrode
SDSS	=	Super Duplex Stainless Steel
SEM	=	Scanning Electron Microscopy
TIG	=	Tungsten Inert Gas
TTT	=	Time Temperature Transformation
WE	=	Working Electrode
XPS	=	X-ray Photoelectron Microscopy

Symbol list

α	=	Ferrite
γ	=	Austenite
γ_2	=	Secondary austenite
E	=	(Applied) potential
E_{crit}	=	Critical pitting potential
E_p	=	Critical potential
E_{pp}	=	Passivation potential
E_t	=	Transpassive potential
HV5	=	Vickers hardness with a 5 kp load
i_a	=	Anodic current density
i_{pass}	=	Passivation current
i_{pass}	=	Passivation current
IR (drop)	=	Ohmic drop
R	=	Resistance
T_{crit}	=	Critical corrosion temperature
T_{repass}	=	Repassivation temperature

Chapter 1

Introduction

The Norwegian Public Roads Administration (NPRA) is planning to build the world's longest floating bridge to cross Bjørnafjorden [1, 2]. The fjord crossing is part of the ambitious project *Ferjefri E39* (Ferry free E39 a.k.a. Coastal Highway Route E39), whose goal is to reduce traveling time in the coastal route between Trondheim and Kristiansand. Seven ferry routes are planned to be replaced with bridges and tunnels. To cross Bjørnafjorden, it takes 40 min with the current ferry route whereas, with the Bjørnafjorden bridge, it will take 11 minutes driving [3].

Bjørnafjorden is located south of the city of Bergen, between the municipalities of Tysnes, Os, Fusa and Austevoll. This fjord is particularly challenging to the project due to its 5-kilometer length and depths up to approximately 600 meters [1]. Such demanding dimensions led to the proposal of a floating bridge where pontoons support the bridge structure due to buoyancy. One of the proposed solutions involves pontoons designed to be 58 m long, 9 m high and 12 m deep, as shown in Appendix A. The pontoons are designed to be made of carbon steel with 25Cr super duplex stainless steel (SDSS) in the section surrounding the pontoon at the splash zone. The choice of SDSS for this section was made based on the fact that the splash zone is a critical area in the pontoon due to periodic immersion in seawater. 25Cr SDSS was chosen because of its excellent corrosion resistance and because the bridge is required by the NPRA to have a lifetime of 100 years.

The combination of strength and excellent corrosion resistance of SDSS has led to its frequent use by the oil and gas industry for seawater applications. Nevertheless, its maximum operation temperature in seawater is still debated [4]. The NORSOK M-001 [5] and ISO 21457 [6] standards specify a limit of 20 °C for SDSS in seawater, however, the limits stated by standards are meant to be conservative and safe. In the end, it is often the operators themselves the ones to define their own user limits [4].

Some of the environmental challenges experienced by the SDSS section in the splash zone of the pontoons involve heating due to radiation from the sun, crevice formation due to macrofouling, and periodical evaporation of seawater at the water line resulting in the concentration of salts. In addition, some challenges in terms of design involve welding, cathodic protection of the submerged carbon steel and coatings that can form crevices.

The author investigated the corrosion properties of SDSS in seawater and marine environments, focusing on critical crevice corrosion temperature, as a part of a specialization project [7]. Both a literature survey and experimental work were carried out to identify the main causes of corrosion failure in SDSS and how different parameters, such as potential, affect its critical crevice corrosion temperature. This work is explained in more detail in Section 3.

Based on the results from the specialization project, this master's thesis focuses on the corrosion properties of welded SDSS in seawater. Although the main focus will be welding of SDSS only, the pontoon design involves welding SDSS to carbon steel and coating the welded area. In that case, if the welds are exposed to seawater due to damage to the coating, the corrosion problems relate to galvanic corrosion rather than just localized corrosion. Moreover, immersion in seawater was chosen to be the condition to be examined since it is important to first understand the corrosion behavior of welded SDSS in this condition before addressing the challenges associated with the periodical wetting and drying at the splash zone.

The main objective of this work is, thus, to document the critical corrosion temperature of welded SDSS in seawater. In order to achieve this, available literature on the critical corrosion temperature of welded SDSS in seawater and similar environments will be investigated. Additionally, experimental work will be performed to determine the critical corrosion temperature of welded SDSS in natural seawater and how different surface conditions (pickling and coating), welding procedures, cathodic protection and polarization of the sample affect the critical corrosion temperature. The experimental work involves critical corrosion temperature tests partially based on the ASTM G150 standard carried out in natural seawater, as well as a long-term exposure test in natural seawater which has been heated to the fixed temperature of 40 °C to simulate the effect of sudden heating. Furthermore, the welds will be characterized in order to understand the nature and possible causes of the corrosion attacks. This will be done by examining the nature of the corrosion attacks with a scanning electron microscope (SEM) and with energy-dispersive X-ray spectroscopy (EDS). In addition, the welds will also be characterized by examining the presence of deleterious phases with SEM-backscattered electron (BSE) and examining the distribution of the different phases in the different areas of the welded sample with electron backscatter diffraction (EBSD), and, finally, by characterizing the passive layer of the welded samples through X-ray photoelectron spectroscopy (XPS).

Chapter 2

Theory

2.1 Duplex and super duplex stainless steel

Duplex stainless steels (DSSs) are alloys whose two constituent phases, austenite (γ) and ferrite (α), are present in approximately equal proportions [8]. These alloys have a higher tensile and yield strength than their single-phase austenitic counterparts, as well as improved resistance to stress corrosion cracking (SCC), particularly in chloride-containing media [9]. They derive their high strength, which is almost twice that of austenitic stainless steels, from the presence of ferrite, as well as from the grain refinement that results from having two phases preventing their mutual growth during heat treatment [10, 11]. However, the toughness and ductility of DSS lay between those of austenitic and ferritic stainless steels (ASS and FSS, respectively) [9]. Nevertheless, DSSs have excellent corrosion resistance almost equal to those of ASSs with similar alloy compositions [9], in addition to having an improved resistance to transgranular SCC provided by the ferritic phase [11]. The limitations of DSS arise with higher Cr contents, mostly after prolonged exposure at higher temperatures, which may lead to embrittlement and loss of toughness due to the precipitation of intermetallic phases [9].

The SDSSs are higher-alloyed DSS, whose PRE_N (defined in Section 2.1.3) are above 40. SDSSs were originally developed to meet the demands of the Norwegian offshore industry operating in the North Sea, but are now also used in the chemical and petrochemical process industries [12]. These alloys have a higher resistance to pitting and crevice corrosion due to the higher amounts of Cr, Mo and N. [13]

More recently developed DSS alloys include the lean and hyper DSS, whose compositions are shown in Table 2.1. The former was developed to compete with the traditional AISI 304 and AISI 316 austenitic stainless steels while the latter competes with titanium and Ni-based alloys. In terms of composition, the lean grades contain less Ni and Mo but are higher in N, Mn and Cr compared to conventional DSS, while the hyper DSS are highly alloyed especially in terms of N which gives them a PRE_N of about 49. [8]

2.1.1 Metallurgy

The duplex microstructure is a result of increasing the Cr content of stainless steels to above 20 wt% and heat treatment in the $\alpha + \gamma$ field. Figure 2.1 shows a phase diagram for a DSS based on a pseudo-binary phase diagram for an alloy with 65 % Fe [13]. This figure illustrates DSSs solidify as 100 % ferrite before reaching the solvus line. Austenite then nucleates and grows, first at the ferrite grain boundaries and later within the ferrite grains along preferred crystallographic directions [9]. As the $\alpha \to \gamma$ transformation takes place, alloying elements diffuse with γ-stabilizers such as C, N, Ni and Cu, concentrating in the austenite and α-stabilizers such as Cr, Mo and W, concentrating in the ferrite [9].
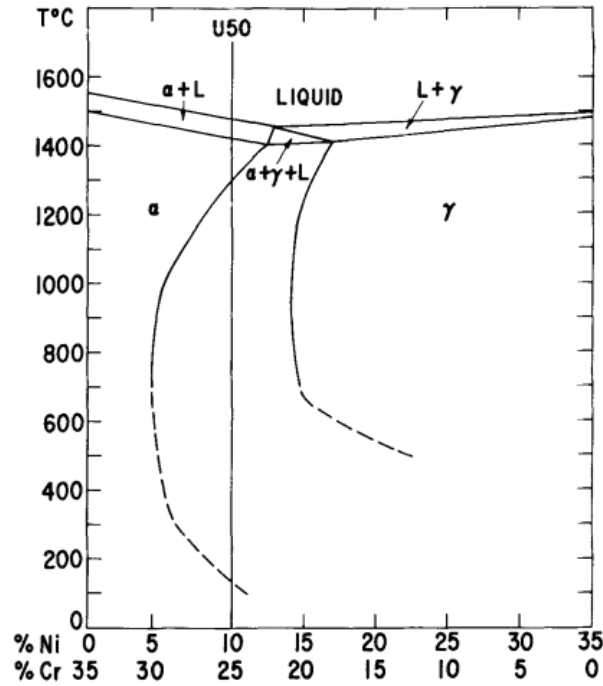
Figure 2.1: Pseudo-binary phase diagram of 65%Fe-Cr-Ni [14].

2.1.2 Microstructure

The microstructure of DSSs consists of austenite islands in a ferrite matrix. The resulting microstructure is highly dependent on the heat treatment cycle [10]. Prolonged heat treatment at a high temperature produces equiaxed grains, while cooling at intermediate rates produces a Widmannstätten-type structure [10]. It is also possible to produce an almost fully ferritic microstructure if the DSS is quenched from near the solidification temperature. Figure 2.2 shows the microstructure of a wrought and a cast DSS.
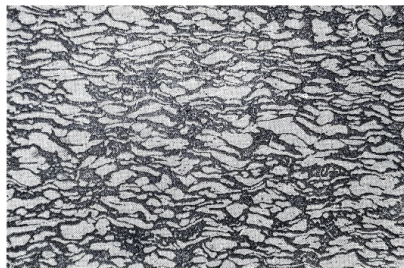
(a) Wrought duplex stainless steel Fe-22Cr-5.5Ni-3Mo-0.15N etched in 40% NaOH
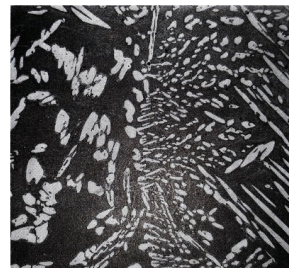
(b) Cast duplex stainless steel Fe-22Cr-5.5Ni-3Mo-0.15N etched in 40% NaOH

Figure 2.2: Microstructure of DSS made of austenite islands (lighter phase) in a ferrite matrix (darker phase) [15].

2.1.3 Composition

The composition of different DSS grades is shown in Table 2.1 together with three ASS grades for comparison. The table includes the pitting resistance equivalent, PRE_N, of each alloy. The PRE_N is a measurement that uses the alloy's composition to predict its susceptibility to pitting corrosion in chloride-containing media. Equation 2.1 shows the most widely used formula to calculate the PRE_N, which is specified by NORSOK [5].

$$PRE_N = \%Cr + 3.3(\%Mo) + 16(\%N) \tag{2.1}$$

Table 2.1: Alloy composition and PRE$_N$ for various duplex and austenitic stainless steels [9, 16].

UNS no.	Type	Composition, wt% max										PRE$_N$
		C	Mn	Si	P	S	Cr	Ni	Mo	N	Other	
S32205	Standard duplex	0.030	2.00	1.00	0.030	0.020	22.0-23.0	4.50-6.50	3.00-3.50	0.14-0.20	-	30.5-37.8
S32304	Lean duplex	0.030	2.5	1.0	0.04	0.04	21.5-24.5	3.0-5.5	0.05-0.60	0.05-0.20	0.05-0.60 Cu	22.5-29.7
S32707	Hyper duplex	⩽0.030	⩽1.5	⩽0.5	⩽0.035	⩽0.010	27	6.5	4.8	0.4	1.0 Co	⩾48
S32750	Super duplex	0.030	1.2	1.0	0.035	0.02	24.0-26.0	6.0-8.0	3.0-5.0	0.24-0.32	0.5 Cu	37.7-47.6
S32760	Super duplex	0.030	1.0	1.0	0.03	0.01	24.0-26.0	6.0-8.0	3.0-4.0	0.30	0.5-1.0 Cu 0.5-1.0 W	⩾40
S30400	304 austenitic	0.08	2.0	1.00	0.045	0.03	18.0-10.0	8.00-10.5	-	0-0.1	-	17.5-20.8
S31600	316 austenitic	0.08	2.0	1.00	0.045	0.03	16.0-18.0	10.0-14.0	2.0-3.0	0-0.1	-	23.1-28.5
S31254	6%Mo super austenitic	0.20	1.00	0.80	0.030	0.010	19.50-20.50	17.50-18.50	6.00-6.50	0.180-0.220	0.50-1.00 Cu	42-44

2.1.4 Passivity

Stainless steels have a characteristic minimum Cr content of approximately 11 % which leads to the formation of a chromium-rich oxide surface film [17]. The formation of this film reduces the reaction rate between the steel and the environment by several orders of magnitude [18]. This process, called *passivation*, can be explained by means of a polarization curve where the change in anodic current density, i_a, as a function of potential applied, E, is illustrated. At lower potentials, active dissolution of the metal takes place, where the anodic current density increases with the potential applied until the passivation potential, E_{pp}, where the current suddenly drops significantly to the passivation current i_{pass} [19, 20]. At higher, i.e. more noble, potentials the current density can rise again as a result of film oxidation above the transpassive potential, E_t, or due to film breakdown above the critical potential, E_p in this case, due to the presence of certain anions such as chlorides [19, 20]. Figure 2.3 illustrates an example of a polarization curve.

Increasing the Cr content of Fe-Cr alloys lowers the E_{pp} and, in chloride-containing environments, increases E_p to more noble values, widening the passive range, in addition to reducing i_{pass} [19].

The passive film on stainless steels is usually 1–3 nm thick and able to regenerate itself in the presence of oxygen [17, 20]. The outermost part of this film has been suggested to be made out of trivalent Fe and Cr hydroxides on top of a Cr_2O_3 layer which is only sparingly soluble and acts as an effective barrier protecting the metal from dissolution [18, 20]. Cr_2O_3 is considered to produce a continuous Cr-O-Cr-O network which prevents the dissolution of iron [20, 22]. Moreover, the passive film also includes a Ni-enriched layer at the interface between the oxy-hydroxide outer layer and the bulk metal [18, 23, 24].

One important characteristic of passive films is their dynamic nature [18]. A material's passive film changes its thickness and composition with the environment as a result of a constant exchange of species with the surrounding electrolyte [18]. These changes are influenced by factors such as potential, the presence of aggressive species in the electrolyte e.g. chlorides, pH and temperature [18].

Although research dealing with the nature of the passive films of the austenitic and ferritic phases in DSS is limited, much of the literature point out a disparity in composition of the passive film in DSS at the different phases due to the preferential partitioning of elements such as N, Ni and Cr to either austenite or ferrite [24].
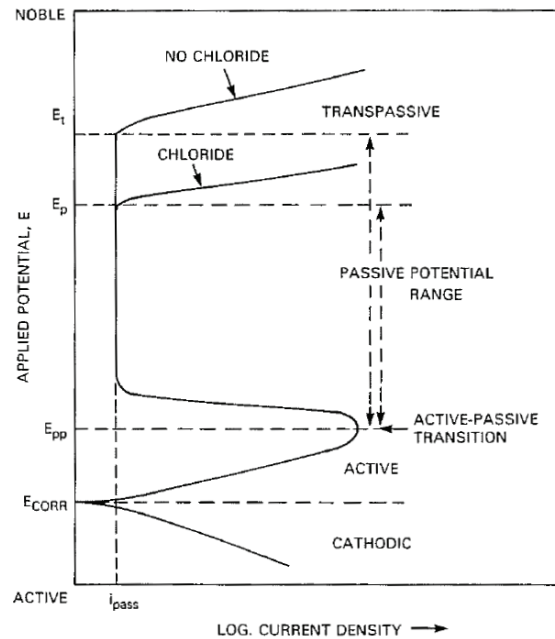
Figure 2.3: Schematic illustration of a polarization curve for a stainless steel showing the potential vs. current behavior during passivity [21].

2.1.5 Secondary phases

Prolonged exposure in the temperature range 300–1000 °C, such as during heat treatment or welding, leads to the undesirable precipitation of intermetallic phases in DSS due to high alloy content and the presence of ferrite [9, 25, 26]. SDSSs are therefore more susceptible to intermetallic phase formation than normal DSSs. Figure 2.4 shows a time temperature transformation (TTT) diagram illustrating the possible precipitations that can take place in SDSS and how different alloying elements affect their occurrence.
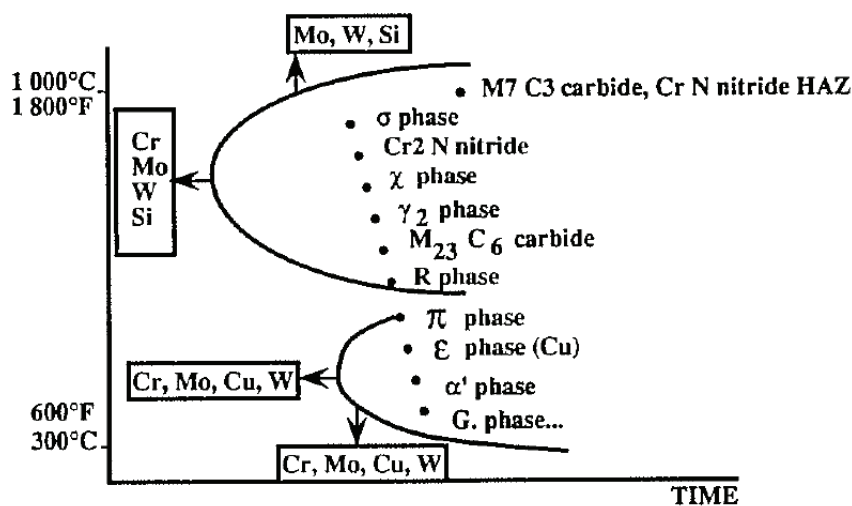
Figure 2.4: TTT diagram illustrating the effect of different alloying elements in the precipitation of various species [27].

Several precipitates have been observed in DSS such as sigma (σ) phase, chi (χ) phase, η (Laves) phase, Cr_2N, CrN, secondary austenite (γ_2), M_7Cr_3 and $M_{23}Cr_6$. However, the σ phase is by far the most prominent since it affects toughness and corrosion resistance [26], and because DSSs are more susceptible to its precipitation than ASSs or FSSs [8].

The σ phase is known to form rapidly (in a matter of 2–15 minutes in some cases [9]) in DSSs. The precipitation of σ phase is also enhanced by deformation such as hot rolling at 800–900 °C [28]. As it can be seen in Figure 2.4, the high amounts of Cr and Mo make SDSS more susceptible to the precipitation of this phase. Triple junctions or α/γ phase boundaries are the preferred sites of nucleation for the σ phase [26]. The precipitation of this phase causes the depletion of Cr in the adjacent ferrite, also called sensitization, rendering it more susceptible to localized corrosion attacks [28].

The χ phase often coexists with the σ phase and, since it also decreases toughness and corrosion resistance, it is difficult to isolate its effects [28]. Figure 2.5 shows the σ and χ precipitates in S39274, a W-containing SDSS [29].
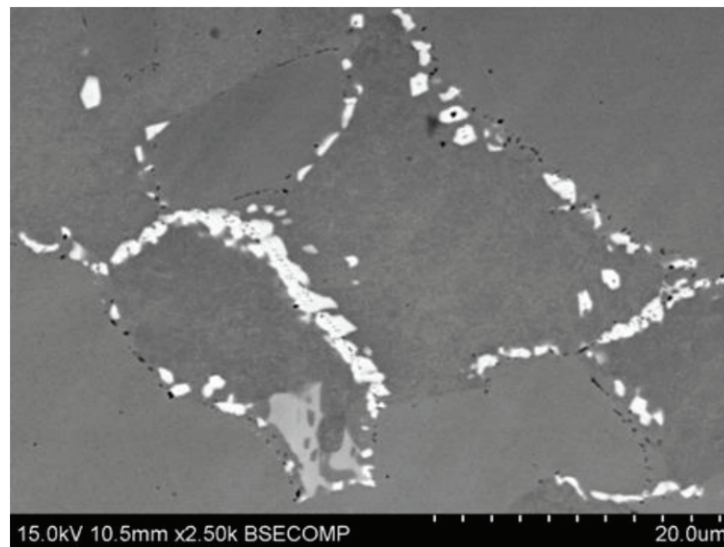
Figure 2.5: σ (light gray particles) and χ (white particles) precipitates in S39274 imaged by SEM/BSE [30].

Chromium nitrides precipitation is also common due to alloying with N. Nitrides can form due to long aging times or due to quenching from solution treatment temperatures [29]. The latter is due to the solubility of N in ferrite at high temperatures which then leads to intragranular precipitation upon quenching. Intergranular precipitation occurs as a result of heat treatments at elevated temperatures where the precipitates will decorate the α/γ or α/α phase boundaries [26] as imaged by Llorca-Isern et al. [31] for DSSs and SDSSs. The subsequent depletion of Cr in grains and grain boundaries then decreases corrosion resistance.

The low C content in SDSS compared to DSS makes them less susceptible to Cr-carbide precipitation, in addition to DSSs in general having a higher resistance to sensitization due to carbide precipitation than ASSs [13, 26].

2.2 Welding SDSS

2.2.1 Welding metallurgy

Solidification structure

For DSS (including SDSS), the weld metal is fully ferritic upon solidification and remains as such until around 1200 to 1300 °C. As temperature decreases, the ferrite solvus is crossed, entering the dual-phase field where austenite begins to form [32, 33]. The phase transformation sequence taking place upon cooling DSS is shown in Equation 2.2.

$$\text{Liquid} \longrightarrow \text{liquid} + \text{ferrite} \longrightarrow \text{ferrite} \longrightarrow \text{ferrite} + \text{austenite} \tag{2.2}$$

Due to its diffusional nature, the solid-state phase transformation from austenite to ferrite is affected by both time and temperature [32]. For the weld, this means that a lower cooling rate will promote the transformation to austenite. SDSSs enter the dual-phase field at higher temperatures than DSSs, resulting in more time for the diffusion-driven solid-state transformation to austenite [32].

The microstructure in the weld is closer to that of a cast microstructure than that of the wrought base material. Austenite starts forming preferentially along the ferrite grain boundaries and may also form as intragranular austenite within the ferrite grains or as Widmannstätten side plates from grain boundary austenite [33]. Precipitates such as the σ phase, although much more difficult to observe, are of high importance due to their highly detrimental effect on corrosion resistance and toughness of DSS. The σ phase first forms at the ferrite grain boundaries and then grows into the ferrite grain. The mechanical and corrosion properties of the material can be reduced even by a small amount of precipitates. [32]

At the heat affected zone (HAZ) adjacent to the weld, the temperature of the base metal increases approaching the ferrite solvus as the austenite transforms to ferrite until achieving a fully ferritic microstructure, at the same time as most precipitates begin to dissolve. Above the solvus temperature the ferrite grains grow in the absence of austenite or precipitates which could stifle this process. Finally, as the temperature decreases, austenite and precipitates form again. SDSSs have the advantage of experiencing coarsening in the area immediately adjacent to the weld only. This is due to the higher solvus temperature seen in Figure 2.1. [33]

Ferrite-austenite balance

The alloy composition and the thermal conditions during welding can be tailored to yield a ferrite content within the required limit of approximately 35 to 65 % in the weld and HAZ [32]. For DSS, a higher content of Ni and/or N increase the solvus temperature, allowing austenite to form at higher temperatures. Moreover, a low heat input during welding results in smaller amounts of austenite formed, whereas too high heat input is linked to the formation of intermetallic phases, particularly of sigma phase [32]. For 6-mm S32760 plates, the recommended heat input for the root pass is of $1.0 \, \text{kJ} \, \text{mm}^{-1}$ [34]. However, the difference in alloying content between, for example, a S32205 with a low N content and S32750 has a more significant impact on the amount of ferrite retained than the weld heat input [33]. Furthermore, the cooling rate after welding also affects the final microstructure as too high cooling rates are related to lower austenite content and abundant precipitation of Cr_2N. The latter is linked to nitrogen not being able to partition to austenite [33].

2.2.2 Welding procedures

Processes

The American Welding Society in its *"Master Chart of Welding and Allied Processes"* [35] classifies welding processes into arc welding, brazing, oxyfuel gas welding, resistance welding, soldering, solid-state welding and other welding processes. Arc welding processes such as shielded-metal, submerged, gas-tungsten and gas metal, are among the most commonly used procedures for stainless steels.

Gas-tungsten arc welding (GTAW), also known as tungsten inert gas (TIG) welding, is a welding procedure which uses a permanent, non-consumable tungsten electrode to create an arc to a workpiece [36]. The electrode is protected against degradation through an inert gas, called a shielding gas, such as argon. The welding procedure can be performed with a filler or without (autogenous welding) [36]. Using TIG welding in the root pass of DSS pipes, where only one side is accessible, provides a controllable, high quality root bead that dictates the final corrosion performance of the weld [32]. Additionally, this process eases the close control of backing gases employed [32].

Other welding processes include the high-energy-density beam processes such as electron-beam and laser-beam welding, both of which have much higher power densities than arc [37]. A deep, narrow keyhole is formed during welding with a laser or electron beam, and a deep, narrow penetration weld can be effectively produced [37]. The application of laser welding has been increasing as a result of its high quality, precision, performance, speed and flexibility [37, 38, 39]. The most predominant laser welding processes have been solid-state lasers such as Nd:YAG and gas lasers such as CO_2, but fiber lasers have become an attractive alternative to these [39, 40]. Moreover, it

has been shown that DSSs have good weldability using fiber laser without filler material [38] even when compared to CO_2 lasers [41].

Welding Consumables

The welding consumables are chosen in order to produce the proper phase balance in the weld and good corrosion resistance [33]. Filler materials for DSS are often overalloyed compared to the base material to ensure a satisfactory ferrite and austenite phase balance [42]. "Boosting" the Ni content of nominally matching filler materials and/or the N content promotes the formation of austenite during the cooling of the weld [33, 43].

The choice of shielding and backing gases depends on the welding process used and also affects the final properties of the weld. Backing gases used for the internal protection of one-side welded pipes can be industrial pure Ar or high purity N, although some manufacturers recommend the use of 90 % N_2 and 10 % H_2 ("Formier" gas) [42]. The presence of N in the shielding and backing gasses can prevent the loss of N from the weld metal; more specifically for SDSS, root runs are protected against a decrease of 0.01–0.05 % N when the shielding and backing gasses contain approximately 5 % N_2 [42].

2.2.3 Post weld heat treatment

For DSS, welded structures are put in service in the "as welded" condition [42]. Post weld heat treatment (PWHT) is usually performed for autogenous welds or welds whose filler material composition matches the base material perfectly, or when weldments are highly stained or deteriorated by other phases [42, 44]. The PWHT temperatures needed vary according to the material grade, for example, the annealing temperatures for SDSS are in the range of 1050–1120 °C [42]. The heating should be done as fast as possible and water quenching should be performed immediately after annealing [42].

2.2.4 Cleaning and passivation

High temperature oxides can form on the surface of the material during welding, even if good shielding/backing is employed [45]. These oxides interfere with the formation of a proper passive layer, leading to an increased susceptibility to pitting corrosion [46]. Cleaning practices can be followed as specified by the ASTM A380/A380M standard [47]. The best method to remove surface oxides and restore the pitting resistance of the welded material has proven to be post-weld cleaning through pickling, using a bath or a paste, made of a mixture of HNO_3 and HF, followed by passivation through immersion in aqueous HNO_3 [46, 48].

2.2.5 Weld mechanical properties

Welds whose compositions match those of the base material, even those boosted with Ni, have matching tensile properties. Annealed welds, however, have reduced yield strength which may not reach the required levels of the base material. Additionally, base metal and welds may show a ductile-to-brittle transition if the proportion of ferrite is high enough. [33]

The high amounts of ferrite at the weld and HAZ also produce an increase in hardness compared to the base material [49].

2.3 Corrosion of SDSS

As passive materials, stainless steels (including SDSSs) are susceptible to localized corrosion attacks due to break-down of the passive layer. These corrosion attacks can be, among others, in the form of pitting or crevice corrosion. Moreover, the presence of aggressive anions, microbes, pH, temperature and other environmental factors, as well as heat treatment, like welding, influence the susceptibility of passive metals to localized corrosion attacks.

2.3.1 Pitting corrosion

Pitting is a type of localized corrosion which produces cavities, called pits, on the surface of the material. This form of localized corrosion may lead to the perforation of equipment and subsequent destructive damage, or may be shallow and, thus, allowed [50].

The pitting corrosion phenomenon can be divided into four equally critical stages: breakdown of the passive film, metastable pitting, pit growth, and pit stifling or death [51]. Although much research has been carried out, the mechanisms involved during the passive film break down and pit initiation are not yet fully understood [20]. However, three possible mechanisms have been postulated to explain the first stage: the penetration mechanism, film-breaking mechanism and the adsorption mechanism [52]. According to the penetration mechanism, aggressive anions are transferred through the passive layer to the metal-oxide interface [52]. The film-breaking mechanism, on the other hand, is based on defects (cracks, pores, etc.) in the passive film which lead to direct contact between the bulk metal surface and aggressive anions which prevent repassivation [52]. Moreover, the adsorption mechanism differs since it is based on the locally enhanced dissolution of the passive film due to the adsorption of aggressive anions replacing hydroxyl groups [20, 52]. All of these mechanisms consider a pure metal while, in reality, the occurrence of pits is linked to inclusions or secondary phase particles [51].

When the pits are short-lived and shallow, they are referred to as metastable pits. These pits are at most micron-sized and exist only for a few seconds, but are still important as they can continue to grow and form large pits under certain circumstances. [51].

Stable pitting and pit growth take place during the propagation stage of pitting corrosion. The rate of pit growth is dictated by the material composition, pit chemistry and potential at the bottom of the pit [51]. In the propagation stage in chloride-containing environments, anodic dissolution of the metal according to Equation 2.3 takes place at the bottom of the pit and it is balanced by the cathodic reaction taking place on the surface of the material adjacent to the pit according to Equation 2.4 [50]. As the concentration of M^+ increases within the pit, Cl^- ions in the electrolyte migrate to maintain electroneutrality [50]. A metal chloride then forms which is hydrolyzed, creating a metal hydroxide and free acid as shown in Equation 2.5 [50]. Finally, the pit can repassivate and die, if the conditions at the bottom are not kept sufficiently aggressive [51].

$$M \longrightarrow M^{n+} + ne^- \tag{2.3}$$

$$O_2 + 2\,H_2O + 4e^- \longrightarrow 4\,OH^- \tag{2.4}$$

$$M^+Cl^- + H_2O \longrightarrow MOH + H^+Cl^- \tag{2.5}$$
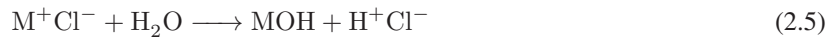
While various environmental factors such as chloride ions, chlorine, certain microbial activity, dissolved gasses and flow have been described to have an effect on pitting corrosion [50], temperature is a prominent factor that has been used to rank a material's susceptibility to pitting corrosion [53, 54]. Resistance against localized corrosion decreases as temperature increases, and, for any steel, a critical pitting temperature (CPT) can be determined below which pits die [55].

As it can be appreciated from the PRE_N formula (Equation 2.1), Cr, Mo and N have a positive effect in pitting corrosion resistance. However, due to secondary phase precipitation, their contents cannot be increased indefinitely [43].

The microstructure of DSSs influences different pitting behaviors, starting with the occurrence of MnS inclusions which are known to dissolve in chloride-containing media and subsequently create a site of initiation for pitting [50]. For DSSs specifically, these inclusions are found at the α/γ phase boundaries and pits will then propagate into austenite or ferrite. Moreover, the precipitation of the aforementioned secondary phases create Cr-depleted areas which are more susceptible to pit initiation.

2.3.2 Crevice corrosion

Crevice corrosion accounts for most of the corrosion failures of SDSS in seawater systems [56]. This form of localized corrosion occurs due to occluded areas creating stagnant conditions for the electrolyte, resulting in a drastic change in the chemistry of the solution locally. Crevice corrosion occurs mainly in passive materials, but not exclusively [57].

Similar to pitting corrosion, the exact mechanism of crevice corrosion is unknown, but many theories have been presented [58]. The basic mechanism of crevice corrosion is based on the deoxygenation-acidification of the crevice prior to initiation [59]. It is assumed that, even in the passive state, there is still some uniform corrosion taking place at the surface of the material which also means that O_2 is consumed as shown in Equation 2.4. As oxygen cannot enter the crevice area, this area gets depleted of oxygen, causing the reduction of oxygen to take place outside of the crevice while the anodic dissolution of the metal continues inside the crevice. Similar to the case of pitting corrosion, the concentration of M^+ increases within the crevice and Cl^- ions then migrate to the occluded area to maintain electroneutrality. The metal cations then become hydrolyzed, acidifying the local environment. A galvanic cell between the crevice and the outside material is established, which leads to a difference in corrosion potential inside and outside of the crevice due to the electrolyte resistivity called IR (ohmic) potential drop [57]. Following this mechanism is the initiation due to passive film breakdown and propagation of crevice corrosion [59]. In the propagation stage, the corrosion current gets limited by the IR drop, the corroded area in the crevice grows, and rapid corrosion ensues as the corrosion reaches the crevice entrance until the corrosion rate decreases again due to the accumulation of salts [59].

It is worth noting that crevice corrosion is a highly stochastic process that is influenced by many factors including, but not limited to, crevice geometry, temperature, electrolyte composition, flow, crevice type (metal/metal, metal/non-metal, etc.) [59]. In the same way as a CPT temperature can be determined, a critical crevice corrosion temperature (CCT) can be determined [60], although with lower accuracy due to the aforementioned factors.

Cr, Mo and N increase the resistance to crevice corrosion of DSS, as in the case for pitting corrosion. Results from research of DSS in seawater suggests N improves the corrosion resistance of the austenite phase as well as aiding Cr retention in this phase [61]. Although the role of W in crevice corrosion has been researched without a general agreement in its effect on crevice corrosion [62, 63], recent work [64] suggests there is a composition range at which W is beneficial. Moreover, the precipitation of secondary phases has also been shown to increase the susceptibility to crevice corrosion [65].

2.3.3 Marine environments

Free-flowing natural seawater is a complex dynamic system containing, among others, gasses, living organisms, and dissolved inorganic material such as salts [66]. The presence of some of these species explain the corrosivity of seawater and affect the materials differently.

High dissolved salt content (salinity) has two actions, the first one being the deterioration of passive films due to chlorides which are the main constituent of the dissolve salts, and the second one being an increase in electrical conductivity resulting in larger currents for a given potential difference [66]. Moreover, presence of Ca and Mg cations in seawater, in combination with a high pH (e.g. from cathodic protection) causes the formation of more or less protective layers on metals called calcareous deposits [66].

In terms of living organisms, different types of bacteria can have different effects on the material [50]. Most notable is the formation of microbial slime layer called biofilm that can increase the cathodic efficiency of the material [60] and cause ennoblement of the stainless steel [12, 56]. To mitigate biological activity the seawater is often chlorinated, which also causes the ennoblement of stainless steels. For seawater systems, ISO 21457 mentions a typical residual chlorine level for continuous use of 0.3–0.7 ppm [6].

Shifting the corrosion potential of stainless steels to higher values due to ennoblement by biofilms or chlorination makes the material more susceptible to localized corrosion attacks. For SDSS, ennoblement due to biofilm reaches values above +300 mV vs. SCE after a few weeks of exposure [12, 56], whereas in chlorinated seawater these values can reach +600 mV vs. SCE [12, 67]. The corrosion potentials of SAF 2507 (S32750) in different types of seawater environments are shown in Figure 2.6.
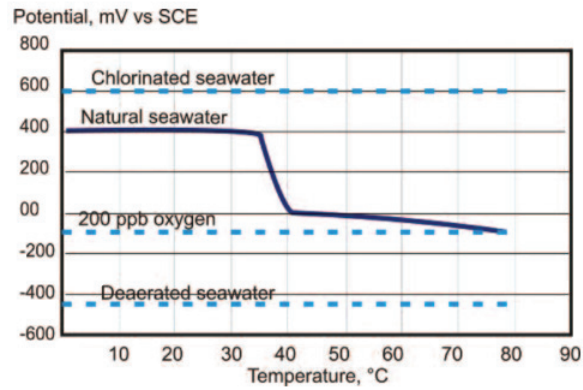
Figure 2.6: Corrosion potentials of Sandvik SAF 2507 in different types of seawater environments [68].

2.3.4 Test methods for localized corrosion

Several test methods have been developed to characterize the resistance to localized corrosion of stainless steels [50, 65], which notably include the ASTM G48 [69] and ASTM G150 [70] standards.

The ASTM G48 standard is used to determine the pitting and crevice corrosion resistance of stainless steels and related alloys in chloride containing environments through immersion in a 6 wt% $FeCl_3$ solution. The test methods are classified into six categories from A to F. Methods A and B determine the localized corrosion of the material through immersion at a fixed temperature, recommended to be 22 ± 2 °C or 50 ± 2 °C for 72 hours. Methods C – F are meant to rank alloys by determining the CPT or CCT by immersing a sample at a certain temperature and testing for 24 or 72 hours, if no localized corrosion is seen, the temperature of the bath is increased by 10 °C and a new sample is tested, if localized corrosion initiated, the temperature is decreased by 5 °C and a new sample is tested. For welded material, a modified version of this standard has been used where the same sample is used as the temperature is increased until the corrosion potential of the sample drops [71, 72].

The ASTM G150 standard is used to evaluate the resistance to pitting corrosion of stainless steels by determining the CPT in a 1 M NaCl solution during a potentiostatic test. In this test, the temperature of the solution is increased at 1 °C min^{-1} and the CPT is then defined as the temperature at which the current density increases rapidly above 100 µA cm^{-2} for 60 seconds. This test can be modified to determine the CCT as well [73].

Chapter 3

Literature survey

The corrosion properties of stainless steels in seawater have been thoroughly documented through years of research. The corrosion properties of SDSS base material in seawater specifically were investigated as part of the author's specialization project. The following literature survey thus focuses on the corrosion properties of welded SDSS in seawater with special attention to critical corrosion temperature (T_{crit}). The term T_{crit} will be used hereafter to refer to both the CPT and CCT.

3.1 Corrosion properties of SDSS base metal

Results from specialization project

In the specialization project, the author investigated the corrosion properties of SDSS in seawater and marine environments [7]. The report included a literature survey on the experiences with SDSS in seawater/marine environments with special focus on crevice corrosion, and experimental work testing SDSS base material. The literature survey revealed that the bacteriological activity in seawater causes the ennoblement of stainless steels [74], to values up to +350 mV vs. SCE for S32750 after a few weeks of exposure [12, 56]. In addition, the cathodic efficiency was increased in the potential range from open circuit potential (OCP) to approximately -500 mV vs. Ag/AgCl [75, 60]. At temperatures above 30-40 °C (depending on geographical location), however, the bacteria is killed, so the effect of ennoblement is eliminated [76, 56]. It was also found that while it has been suggested that S32750 can be used in natural seawater successfully at temperatures up to 40 °C [12, 56], tests have documented that initiation of corrosion can occur at 28-32 °C [77]. Additionally, after initiation, repassivation tests have shown that corrosion can continue to propagate at temperatures as low as 15 °C for high-alloyed rolled, welded and cast stainless steel [78]. Poor quality welds were found to be able to decrease the T_{crit} of S32750 by approximately 20 °C [79] (these results are explained in detail in the next section). Moreover, cathodic protection (CP) of SDSS will affect the T_{crit} of SDSS when the CP system is disconnected during service [80]. The differences in T_{crit} are attributed to adsorbed hydrogen during CP. The effect of CP on the T_{crit} of S32750 base material in chlorinated seawater was examined using a method similar to the ASTM G150 by Olavesen [80]. The samples were charged with hydrogen using different cathodic current densities, for a day or a week, in 3.5 % NaCl aqueous solution. After hydrogen charging, the CCT in simulated chlorinated seawater was determined by immersing the samples in 3.5 % NaCl aqueous solution at 25 °C, and polarizing the samples to + 600 mV vs. Ag/AgCl after one hour immersed at OCP. The temperature was then increased by 4 °C every 24 hours. The results indicate that hydrogen charging decreased the CCT. An uncharged sample had a CCT of 65 °C while both samples charged for 24 hours at -0.1 $mA\,cm^{-2}$ initiated corrosion at 37 °C. Welded S32750 was also investigated under the same conditions and the results are shown in the next section together with follow-up work carried out in natural seawater.

The experimental work performed last Autumn involved immersing S32750 in an aqueous solution of 3.5 wt% NaCl. The experiment included coated specimens and specimens with an artificial crevice, some of which were exposed at OCP while others where polarized. For samples with artificial crevices exposed at OCP corrosion

initiated at temperatures as low as 47 °C while for coated samples polarized to +300 mV vs. Ag/AgCl corrosion initiated at 65 and 77 °C.

The specialization project concluded that similar experimental work should be carried out with welded SDSS in natural seawater in order to determine the effect of welding and CP on T_{crit}.

3.2 Literature review of the T_{crit} of welded SDSS in seawater

Johnsen [81] reports results from determining the T_{crit} of TIG-welded S32750 and S32760 with filler metal in a modified version of the ASTM G48 and by potentiostatic polarization to + 400 mV vs. SCE in 3 % NaCl solution. The temperature in both tests was raised in steps of 2.5 °C every 24 hours. In the modified G48 test, the same specimen and electrolyte were used throughout the test, and the T_{crit} obtained were 45 and 40 °C for S32750 and S32760 respectively. In the potentiostatic polarization test the T_{crit} obtained were 47.5 and 42.5 °C for S32750 and S32760 respectively.

Fager and Ödegård [82] tested TIG-welded S32750 according to a modified version of the ASTM G48 where the same sample was used throughout the test if corrosion did not initiate. TIG-welded SDSS reached a T_{crit} of 50 °C when welded with filler metal using argon as shielding and backing gas, whereas welding without filler metal initiated at 40 °C. The attacks on the TIG-weld with filler occurred at the root and top (opposite side of the root), whereas without the filler metal the attacks occurred at the top only. Moreover, TIG-welded dissimilar joining between Zeron 100 and SAF 2507 (S32750) resulted in initiation at 40 and 45 °C, 5 °C lower than with butt-welding SAF 2507. The attacks took place on the topside of the HAZ of SAF 2507 and the weld at Zeron 100.

As De Marco et al. [83] point out it is worth remembering that the G48 test is meant to be more of a quality control test than a fitness-for-purpose test, given how it often resembles a more severe environment than the one intended during service, such as unchlorinated seawater. Passive stainless steels reach a potential in the range +600 to +650 mV vs. SCE in 6 % $FeCl_3$ which makes the results from this test more suitable for applications in oxidizing environments such as chlorinated seawater [84]. The results from the ASTM G48 mentioned thus far are only meant to illustrate the difference in corrosion resistance between SDSS welds of different grades and qualities. Furthermore, Rogne et al. [84] mention that results from G48 have been misunderstood and welds have been approved due to pitting not being detected by visual inspection, even if the material has shown a significant weight loss. Thus, the use of a scriber to reveal pits was recommended, as well as testing the stainless steel welds to be used in natural seawater in similar Cl^- solutions. They argue that 6 wt% $FeCl_3$ is much more severe of an environment, so the T_{crit} obtained will be lower than in the actual environment. Additionally, it is mentioned that a more realistic T_{crit} is obtained during potentiostatic testing at +400 mV vs. SCE for applications below 35 °C [84].

Johnsen and Vingsand [79] tested simulated welds on S32750 with artificial crevices at fixed potentials ranging from +200 to +800 mV vs. SCE and fixed temperatures in the range 20-80 °C. The test was performed for up to 72 hours in artificial seawater according to ASTM D-1141 [85]. It was found that 30 °C was a safe temperature for the simulated welds for 72 hours in the potential range +400 to +800 mV vs. SCE.

Johnsen [86] also documented the effect of insufficient backing during welding of S32750 and S32760 with the ASTM G150 test. The samples were exposed in 3.5 % NaCl solution and polarized to +600 mV vs. Ag/AgCl to simulate the effect of chlorinated seawater. Some samples were exposed to natural seawater at 10 °C for 14 days before testing, to simulate the effect of building a better passive layer during a "soft" start-up. The temperature was increased in steps of 5 °C every 24 hours. The results showed that T_{crit} was reduced in the absence of backing gas. Also, the T_{crit} of the welded S32750 were in the range 40-50 °C while for S32760 the range was 25-35 °C. The corrosion attacks in both SDSSs occurred in the HAZ and weld metal when pure argon was used as backing gas. When a mixture of argon and 1000 ppm O_2 was used, the corrosion attacks took place at the weld metal for both SDSSs. When no backing gas was used, the corrosion attacks took place at the weld metal in both materials and the T_{crit} was the lowest of all samples tested.

Petterson et al. [87, 88] compared the differences in CPT according to ASTM G150 between different root side TIG weld qualities with filler metal and unwelded base material of S32750. It was found that the as-welded condition, which used argon as backing and shielding gas, had a CPT of approximately 50 °C which was the lowest CPT obtained according to weld quality. The pickled condition, which used argon as backing and shielding gas, and

the as welded condition, which used 90 % N$_2$ + 10 % H$_2$ as backing gas and Ar + 2 % N$_2$ as shielding gas, both had a CPT of approximately 70 °C. The best results were obtained by the pickled condition using 90 % N$_2$ + 10 % H$_2$ as backing gas and Ar + 2 % N$_2$ as shielding gas which had a CPT close to that of the base material (>90 °C). This work concluded that a CPT close to that of base material is attainable and that pickling is a key aspect for this. In addition, the effect of secondary phase precipitation in S32750 welds on CPT by heat treating the base material at either 700 or 850 °C for 1, 10 or 30 min was also investigated. The results showed that the largest CPT differences were due to heat treatment at 850 °C with a significant decrease for holding times of 10 and 30 min. The base material heat treated at 850 °C for 30 min had a CPT of 35 °C. It is assumed the precipitates present are intermetallic phases, predominantly σ, nitrides and carbides, although the amounts precipitated are not mentioned.

The influence of adsorbed hydrogen in the T$_{\text{crit}}$ of welded SDSS in aqueous 3.5 % NaCl solution was examined by Olavesen [80] using a method similar to ASTM G150. The samples were charged with hydrogen for 24 hours with a cathodic current density of -0.1 mA cm^{-2} followed by an hour exposed at OCP in the electrolyte with an artificial crevice. During the test, the samples with the artificial crevice were polarized to + 600 mV vs. Ag/AgCl and the temperature was increased by 4 °C/day. The samples initiated at 49 °C, which was 8–12 °C lower than the uncharged welded samples. Follow-up investigations about the effect of CP on the CCT of S32750 base material [89] used the same procedure used for the welded samples except the material was charged with hydrogen by polarizing the samples to -1100 mV vs. Ag/AgCl for 336 and 720 hours, and the samples were immersed in natural seawater instead. The S3250 base material in this investigation initiated at 25 °C in both cases.

Considering a more realistic environment, Kivisäkk [12] exposed S32750 butt-welded tubes to natural seawater located at the Swedish West Coast. The tubes were placed so that the welds were constantly immersed and only the upper part of each tube was in the splash zone. The tubes were removed from the water for examination after two, four, six and eight years respectively. None of the S32750 tubes corroded after two and four years. After six years, however, TIG-welds presented minor corrosion attacks in the root of 0.03 mm corresponding to a corrosion rate of 0.005 mm/year. After eight years, corrosion of 0.015 mm was seen on manual metal arc (MMA) and TIG welds corresponding to 0.002 mm/year. Both corrosion attacks were deemed to be insignificant. The base material, on the other hand, did not suffer any corrosion attacks despite being covered with hard biological species, such as mussels, which can act as crevices. Moreover, Kvisäkk discusses NORSOK standard M-001 addressing the fact that the recommended limit for use of the different alloys makes no distinction in terms of material quality (base, weld, etc.) and that the recommendations are made based on chlorinated seawater.

Knudsen from SINTEF Industry [90] carried out a field test from the 21st of June to the 16th of November of 2018 of welded S32750 in natural seawater in Oslofjorden. The summer of 2018 was considered to be warmer than usual, so it was assumed the samples experienced temperatures above 20 °C. The samples were TIG-welded manually using Zeron 100X [91] as filler metal. Artificial crevices were placed on the HAZ of four different welded plates which had four different weld qualities; two welded under normal heat input, of which one was pickled after welding and the other was not, and two welded under high heat input, of which one was pickled after welding and the other was not. None of the welding procedures, however, precipitated σ phase. Crevice corrosion attacks initiated on all not pickled samples while the pickled samples showed no signs of corrosion. It was then concluded that pickling reduces the risk of crevice corrosion initiation significantly in an environment similar to Bjørnafjorden. Figure 3.1 shows a corrosion attack on one of the samples and Figure 3.2 shows two of the weld qualities tested after exposure. The holes in the samples on the HAZ correspond to the spots where the artificial crevices were located, not to be confused with the holes at the corners which were used to secure the samples.

Figure 3.1: Corrosion attack under an artificial crevice former on the HAZ [90].
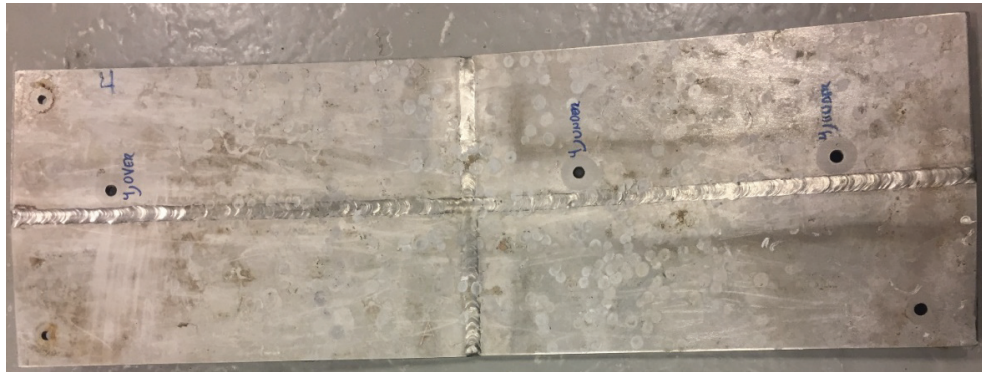
(a) Sample welded under normal heat input and pickled.

(b) Sample welded under high heat input without pickling.

Figure 3.2: Welded samples of different qualities after exposure [90].

Conclusions

The results from ASTM G48 tests should not be used to evaluate the fitness of welded SDSS for the Bjørnafjorden bridge. It is more appropriate to test the sample in seawater and polarized to a fixed potential of +400 mV vs. SCE.

Laboratory results show SDSSs can have a T_{crit} in the range 40–50 °C in seawater or solutions with a similar chloride content, but the exact temperature is highly dependent on the welding procedure and parameters used. This range is at least 20 °C higher than what is stated by NORSOK M-001 and ISO 21457. Nevertheless, T_{crit} as low as 25 °C can be obtained for base material that has been pre-cathodically polarized. Also, experiences in environments similar to Bjørnafjorden show that welds can initiate corrosion if they are not pickled but that pickling may be enough to prevent corrosion initiation of SDSS welds.

None of the laboratory tests or field experiences reviewed attempted to determine a temperature of repassivation for welded SDSS.

Chapter 4

Experimental work

Electrochemical critical temperature testing in natural seawater based on the ASTM G150 standard [70] was carried out on TIG-welded and laser-welded samples, as well as long-term exposure testing. The damage in a few selected samples was further assessed with an IFM and SEM/EDS. In addition, untested TIG-welded not pickled sample surfaces were examined with XPS, and an untested TIG-welded pickled sample cross-section was examined with SEM/BSE and EBSD. Finally, the hardness across the weld cross-section was determined.

4.1 Materials and methods

4.1.1 Material selection and sample preparation

- **Electrolyte:** Natural seawater obtained from 80 m water depth in the Trondheim fjord outside NTNU Centre of Fisheries and Aquaculture (SeaLab)

- **Counter electrode**: Graphite rod for critical temperature testing and platinum mesh for long-term exposure testing

- **Reference electrode**: Ag/AgCl electrode in saturated KCl

The reference electrode was placed in a separate beaker containing saturated KCl, in order to keep it at room temperature throughout the test. A salt bridge connected the reference electrode to the electrolyte used in each test.

All samples were attached to the test cell through thin platinum wires which are assumed to not produce any galvanic effect during the tests. The wires had a diameter of 0.35 mm making the total area exposed negligible compared to the area from the test samples.

The sides and edges of the samples were wet-ground with SiC paper down to #500 grit in order to avoid initiation of corrosion attacks in these areas. The samples were ground at least 24 hours prior to testing to allow for sufficient repassivation. Each sample was rinsed with distilled water and immersed in acetone in an ultrasonic cleaner before testing to get rid of all grease and dirt, except for the coated samples which were only rinsed in distilled water and acetone without the ultrasonic cleaner.

For the base material and TIG-welded samples, Outokumpu Forta SDX 2507 (UNS S32750), hot rolled plate with a 1D finish was used (Apprendix B). For the laser-welded samples, Outokumpu Forta SDX 2507 (UNS S32750) [92], cold rolled, heat treated, pickled was used as the plate material. The alloy composition of the different samples and TIG-welding filler material are shown in Table 4.1.

Before grinding the edges, the base material sample dimensions were 35 mm x 35 mm x 6 mm, while the TIG-welded samples were 40 mm x 40 mm x 6 mm, and the laser-welded samples were 40 mm x 40 mm x 3 mm. All the samples had a Ø 3 mm hole in one corner to secure the sample with the platinum wire.

Table 4.1: Alloy composition and PRE$_N$ for the super duplex stainless steel used for the different experimental samples and filler material. More detailed information is described in the material certificate in Appendix B for the base and TIG-welded samples, and in the material suppliers' own website for the laser-welded samples [92] and filler wire [91].

Samples	UNS no.	Composition [wt%]											PRE$_N$
		C	Mn	Si	P	S	Cr	Ni	Mo	N	Cu	W	
Base and TIG-welded	S32750	0.012	0.81	0.37	0.031	0.001	24.94	6.88	3.79	0.283	0.28	-	42
Laser-welded (typ.)	S32750	0.02	-	-	-	-	25.0	7.0	4.0	0.27	-	-	43
Zeron® 100X wire (typ.)	S32760	0.015	0.7	0.4	0.02	0.002	25	9.3	3.7	0.23	0.7	0.6	41

Welding procedure

Two different welding procedures were tested, laser welding and TIG welding. The TIG welding was performed by SINTEF Industry. More specifically, the plates were welded together through manual TIG welding using $2.4\,\text{mm}$ Zeron 100X TIG wire [91] as filler and argon as shielding gas. The weld consists of four passes: the root, filler (on both sides of the root), and cap. The welding parameters are specified in Appendix C. In addition, some of the TIG-welded samples were pickled after welding and some were not. The laser welding was performed by Skala Fabrikk with a laser welding machine by Mosman Laser BV, and a Ytterbium Multi-Mode Fiber laser (YLS – 3000) unit by IPG, where the welding was performed at 2200 W with argon as backing gas. These samples are shown in Figure 4.1 together with the pickled and not picked TIG-welded samples.

(a) Cap side of TIG-welded sample without pickling.

(b) Cap side of pickled TIG-welded sample.

(c) Top side of laser-welded sample.

(d) Back side of TIG-welded sample without pickling.

(e) Back side of pickled TIG-welded sample.

(f) Back side of laser-welded sample.
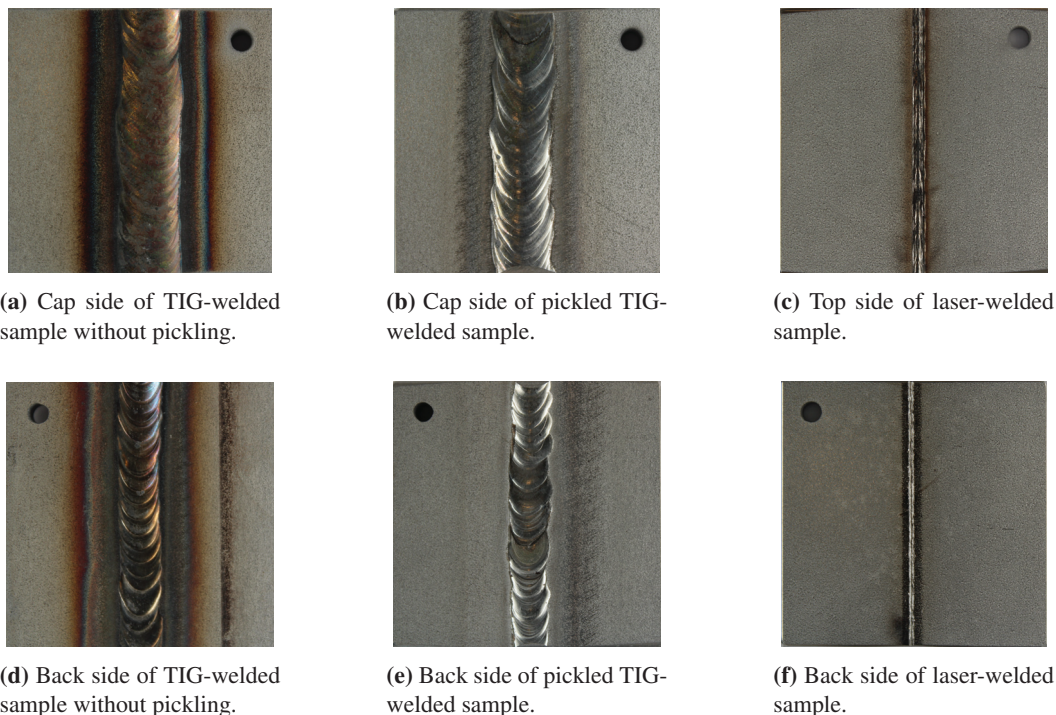
Figure 4.1: Samples showing all three different welded conditions tested.

Coated samples

Some of the welded samples were coated in order to simulate the effect of a "poor" coating which may act as a crevice former during service. The samples were rinsed with distilled water and immersed in acetone in an ultrasonic cleaner before coating. The coating used is Jotun's standard grade Jotamastic 87 [93]. The coating was applied on the cap or top side of the samples in an area of approximately 30x15 mm as shown in Figure 4.2.

Figure 4.2: Coated TIG pickled sample.

4.1.2 Methodology

Critical corrosion temperature

The method to determine the critical corrosion temperature of the samples is partly based in the ASTM G150 standard [70].

After the samples were wet-ground, degreased and, when necessary, coated, the samples were immersed in natural seawater. No more than two samples were placed in a cell simultaneously. Some of the samples were exposed freely, i.e. at OCP, while others were polarized to +400 mV vs. Ag/AgCl. Applying a potential of +400 mV vs. Ag/AgCl was done to simulate the ennoblement due to biofilm discussed in Chapter 3. The samples to be polarized were connected in a three-electrode system with a graphite rod counter electrode and an Ag/AgCl reference electrode in saturated KCl. These samples were first exposed freely in the electrolyte for an hour to stabilize their OCP before being polarized anodically.

For the samples at OCP, the potential development with respect to the time elapsed was measured while, for the polarized samples, the anodic current density with respect to time elapsed was measured. The temperature of the electrolyte was increased, from room temperature (22 ± 1 °C), in increments of 2 °C every 4 hours through the use of a temperature regulator connected to a heat plate. T_{crit} of the samples exposed at OCP is the temperature at which the OCP experiences a sharp drop. For the polarized samples, T_{crit} is the temperature at which the anodic current density exceeded a value of $100\,\mu A\,cm^{-2}$ for at least 60 seconds. In order to confirm corrosion initiation, a visual inspection was also carried out to check for any signs of corrosion products, e.g. brown rust, on the samples or in the electrolyte.

After initiation, the temperature of the electrolyte was decreased to room temperature in stepwise decreases of 2 °C every 2 hours. This was done in order to determine a repassivation temperature, T_{repass}, for the samples. The repassivation temperature is the temperature at which the samples exposed at OCP showed an increase in potential roughly back to the OCP before initiation and, for the polarized samples, when the anodic current density reached a value of $10\,\mu A\,cm^{-2}$. After reaching room temperature the samples were dismounted, inspected to locate the attacks and cleaned by rinsing the sample with distilled water, then ethanol before rinsing again with distilled water and let to air dry. On the other hand, if corrosion did not initiate, the temperature increases would cease at approximately 90 °C before dismounting the sample and cleaning it in the same manner.

As previously mentioned, adsorbed hydrogen has been shown to lower the critical corrosion temperature of SDSS [80]. In order to examine the effect cathodic polarization may have on welded SDSS, some samples were polarized cathodically to $-1100\,$mV vs. Ag/AgCl for a week at room temperature prior to critical corrosion temperature testing. The polarization was carried out by placing the sample in natural seawater, connected as the working electrode in a three electrode arrangement including a graphite rod counter electrode and an Ag/AgCl reference electrode in saturated KCl. After one week of cathodic polarization, the samples were rinsed with natural seawater and the Pt wires were changed, due to the formation of calcareous deposits, all of which took less than 5 minutes. The samples were then immersed in fresh natural seawater, where they were exposed at OCP for an hour. After one hour at OCP, the samples were polarized to +400 mV vs. Ag/AgCl and the critical corrosion temperature test was started.

Figure 4.3 shows the experimental setup used to determine the critical temperature of polarized and freely-exposed samples. In these figures, WE, CE and RE stand for working electrode, counter electrode and reference electrode respectively, while R symbolizes the resistances the samples were connected to and which are equal to 1 Ω.
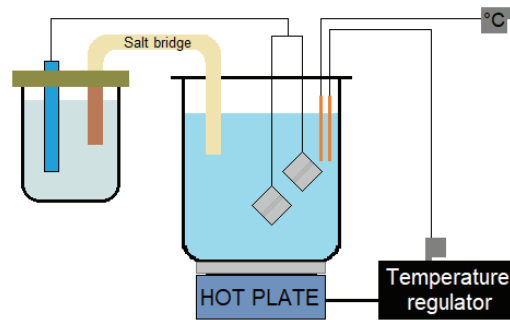
(a) Schematic diagram of the experimental setup for freely-exposed samples.
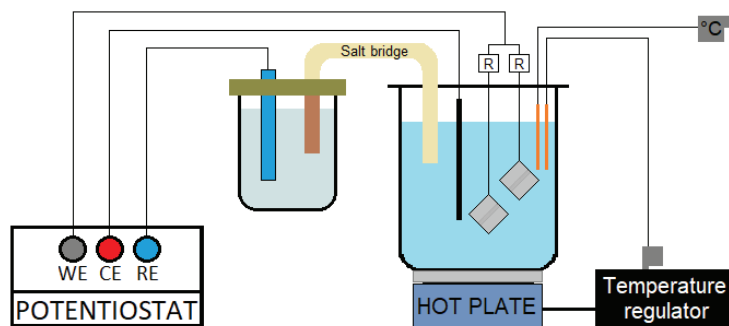
(b) Schematic diagram of the experimental setup for polarized samples.

Figure 4.3: Experimental setup to determine critical corrosion temperature.

Table 4.2 shows the test matrix including all different sample conditions tested and number of parallel samples for each. The base material was also tested anodically polarized as a baseline and corresponds to the last line in the test matrix.

Table 4.2: Test matrix for critical corrosion temperature experiments.

Polarization [mV vs. Ag/AgCl]	Welding technique	Pickling	Coating	1 week cathodic polarization	No. of parallel samples
OCP	TIG	-	-	-	2
OCP	Laser	-	-	-	2
OCP	TIG	-	Yes	-	2
OCP	TIG	Yes	Yes	-	2
OCP	Laser	-	Yes	-	2
+400	TIG	-	-	-	2
+400	TIG	Yes	-	-	1
+400	Laser	-	-	-	2
+400	TIG	-	Yes	-	2
+400	TIG	Yes	Yes	-	2
+400	Laser	-	Yes	-	2
+400	TIG	Yes	-	Yes	1
+400	TIG	Yes	Yes	Yes	1
+400	-	-	-	-	2

Long-term exposure

To simulate the effects of a sudden increase in temperature, coated samples with different weld qualities were immersed in natural seawater at room temperature for a day before increasing the temperature of the electrolyte to a fixed temperature equal to 40 °C where it was kept until experiment completion. The electrolyte was drained and fresh seawater heated to 40 °C was added while keeping the samples submerged. This process was done at most every two weeks, to freshen up the electrolyte to resemble the chemistry and biology of free-flowing natural seawater.

Similarly to the critical corrosion temperature test, some samples were polarized to +400 mV vs. Ag/AgCl using the same three-electrode system but with a Pt-mesh counter electrode while others were exposed at OCP. The polarized samples were exposed at OCP for an hour during immersion before being polarized. Starting from immersion at room temperature, the potential development with respect to the time elapsed was measured for the samples at OCP, while, for the polarized samples, the anodic current density with respect to time elapsed was measured. Once initiation took place similarly to the critical temperature test, the polarized samples were dismounted in order to avoid significantly polluting the water.

The sample matrix for the long-term exposure test is presented in Table 4.3.

Table 4.3: Test matrix for long-term exposure experiments.

Polarization [mV vs. Ag/AgCl]	Welding technique	Pickling	Coating
OCP	TIG	-	Yes
OCP	TIG	Yes	Yes
OCP	Laser	-	Yes
+400	TIG	-	Yes
+400	TIG	Yes	Yes
+400	Laser	-	Yes

Infinite Focus Microscope

The samples from the critical corrosion temperature test were examined with an Infinite Focus Microscope (IFM), Alicona's InfiniteFocus, after testing. This instrument has a vertical resolution of up to 10 nm and can both perform 3D micro coordinate measurements as well as surface roughness measurements [94].

The samples were examined with a magnification down to 20X in order to locate the corrosion attacks. When appropriate, the depth of the attack was measured, and the attack was imaged in 3D.

Scanning electron microscope/energy-dispersive X-ray spectroscopy

The corrosion attacks on the not pickled, TIG-welded, coated samples exposed at OCP and polarized, as well as the attacks on the not pickled, TIG-welded, not coated polarized sample were examined with a SEM and using EDS. The SEM used was Quanta FEG 650 (ESEM) and the program used for the EDS analysis was EDAX's TEAM. The SEM was used for imaging the corrosion attacks to determine the nature of the attack, e.g. if a selective attack initiated on either γ or α. The EDS analysis was performed to determine the chemical composition at different spots of the corrosion damage expressed as relative weight percentage.

In order to estimate how the different spots compare in terms of corrosion resistance, a modified version of the PRE_N was calculated only taking into account the amounts of Cr and Mo in the sample. This modified PRE_N, referred to as PRE_N* in this work, does not take into account the amount of N in the sample as it cannot be detected through EDS. Equation 4.1, formulates the modified version of the PRE_N.

$$PRE_N* = \%Cr + 3.3(\%Mo) \tag{4.1}$$

Backscattered electron and Electron backscatter diffraction

BSE imaging was used to detect the presence of secondary phases in a TIG-welded pickled untested sample. Then, the phase distribution and grain size of the weld, HAZ and base material of the same sample was investigated with EBSD. The sample's cross-section was wet-ground with SiC paper down to # 1200 grit, polished with diamond suspension down to a 1 μm finish, electropolished in a solution made out of 5.3 vol.% $H_2SO_4 \cdot$ 94.7 vol.% CH_3OH, then rinsed with ethanol and stored in a desiccator prior to the analysis.

The same SEM as in the previous analysis was used for the BSE and EBSD analysis. The program used to index the diffraction patterns was TSL OIM Data Collection 7 and the diagrams were generated by the program TSL OIM Analysis 7. The phases investigated were γ and α.

X-ray photoelectron spectroscopy

The surfaces of the pickled and not pickled welds, HAZ and base material were characterized by depth profiling with XPS in order to determine the elemental composition of each surface and the Cr-species present. The samples were cut into 10 mm x 5 mm x 3 mm specimens retaining the surfaces of each sample. The samples were then rinsed with distilled water, cleaned in ethanol in an ultrasonic cleaner, and stored in a desiccator prior to the analysis.

The XPS measurements were performed using a Kratos Axis Ultra DLD instrument with a monochromatic Al K_α source (10 mA and 10 kV) where argon-ion sputtering was used to obtain the depth profiles. The analysis chamber pressure during the operation was 1×10^{-9} Torr. The data was then processed using Shirley background subtraction and the CasaXPS software for curve fitting, where Gaussian/Lorentzian asymmetry was employed with parameters of standard peaks. For oxide components belonging to the same element, the full width at half maximum was kept constant, as well as the peak area ratio of the Mo doublets.

Hardness across the weld

The hardness along the cross-section of a welded sample was also determined to further describe the weld properties. The results obtained will not be discussed as they are not strictly related to the main goal of the present work. The Vickers hardness measurements with a 5 kp load (HV5) were performed with Matsutawa's DVK-1S indenter.

4.2 Results

4.2.1 Critical corrosion temperature

The results from all critical corrosion temperature tests are summarized in Table 4.4, where T_{crit} and T_{repass} correspond to the critical corrosion temperature and temperature of repassivation respectively. When initiation did not take place on a sample, the maximum temperature achieved in the test is shown preceded by a greater-than sign, $>$, indicating the critical temperature exceeds the temperatures tested. Similarly, when the sample was not able to repassivate, the minimum temperature achieved after initiation is shown preceded by a less than sign, $<$. The diagrams showing the evolution of the OCP or anodic current density as a function of time and temperature for each sample are shown below, together with IFM images of the samples when relevant.

Table 4.4: Summary of results from critical corrosion temperature test for all samples, where T_{crit} and T_{repass} correspond to critical corrosion temperature and temperature of repassivation respectively.

Polarization [mV vs. Ag/AgCl]	Welding technique	Pickling	Coating	1 week cathodic polarization	Sample	T_{crit} [°C]	T_{repass} [°C]
OCP	TIG	-	-	-	A	> 90	[1]N/A
OCP	TIG	-	-	-	B	> 90	[1]N/A
OCP	Laser	-	-	-	A	> 80	[1]N/A
OCP	Laser	-	-	-	B	> 80	[1]N/A
OCP	TIG	-	Yes	-	A	42	38
OCP	TIG	-	Yes	-	B	40	< 26
OCP	TIG	Yes	Yes	-	A	> 88	[1]N/A
OCP	TIG	Yes	Yes	-	B	> 88	[1]N/A
OCP	Laser	-	Yes	-	A	52	< 25
OCP	Laser	-	Yes	-	B	36	< 25
+400	TIG	-	-	-	A	53	23
+400	TIG	-	-	-	B	53	23
+400	TIG	Yes	-	-	A	72	24
+400	Laser	-	-	-	A	46	< 25
+400	Laser	-	-	-	B	48	25
+400	TIG	-	Yes	-	A	47	23
+400	TIG	-	Yes	-	B	50	22
+400	TIG	Yes	Yes	-	A	44	< 23
+400	TIG	Yes	Yes	-	B	51	30
+400	Laser	-	Yes	-	A	41	< 24
+400	Laser	-	Yes	-	B	45	< 24
+400	TIG	Yes	-	Yes	A	24	< 21
+400	TIG	Yes	Yes	Yes	A	24	< 21
+400	-	-	-	-	A	> 89	[1]N/A
+400	-	-	-	-	B	> 89	[1]N/A

[1]N/A: Corrosion initiation did not take place

There were some technical faults with the temperature regulator during the test which caused some of the temperature curves to differ from the planned temperature run. This also lead to the test not starting exactly at room temperature or not ending exactly at 90 °C. However, the general temperature increase/decrease was followed. Additionally, in some cases the temperature was not decreased after initiation until several hours later if, for example, corrosion initiated during the night. The temperature would then continue to increase at the same rate after initiation.

Samples exposed at OCP

The TIG-welded, not pickled, not coated samples exposed at OCP did not initiate corrosion during the test which ran until 90 °C as it can be seen from the lack of a potential drop in Figure 4.4. Additionally, brown rust was not seen on the samples during the test and corrosion attacks were not detected with the microscope.

Figure 4.4: Open circuit potential development as a function of time and temperature for the TIG-welded, not pickled, not coated samples exposed at OCP.

Similarly, for the laser-welded not pickled, not coated samples exposed at OCP, no corrosion attack seems to have taken place as it can be seen in Figure 4.5 where the only drops are a product of noise in the data. Also, brown rust was not seen on the samples during the test and corrosion attacks were not detected with the microscope. However, some faults with the temperature regulator made the temperature stay at 80 °C for the remainder of the test instead of increasing all the way to 90 °C. Another similar fault took place after approximately 57 hours which explain the abrupt change in temperature from 52 °C to 60 °C.

Figure 4.5: Open circuit potential development function of time and temperature for the laser-welded, not pickled, not coated samples exposed at OCP.

Figure 4.6 shows the OCP development for the TIG-welded, not pickled, coated samples exposed at OCP. Also, the first temperature decrease is larger than the planned 2 °C due to faults with the temperature regulator. Nevertheless, it is possible to see that the potential of Sample B begins to drop at 40 °C which was confirmed by the presence of orange rust before the temperature was increased to 42 °C. For Sample A, however, the T_{crit} was less evident due to a more gradual decrease in potential. Very small amounts of brown rust were seen as the temperature was 42 °C, therefore, this temperature was later chosen to be T_{crit} for Sample A, even though the OCP had stayed approximately constant since the temperature change to 40 °C. Because the potential drop happened gradually as the samples began to corrode, the temperature regulator was not adjusted to decrease the temperature until the day after, when the presence of brown rust was more visible for Sample A. Moreover, it can also be seen in Figure 4.6 that only Sample A managed to repassivate during the test.
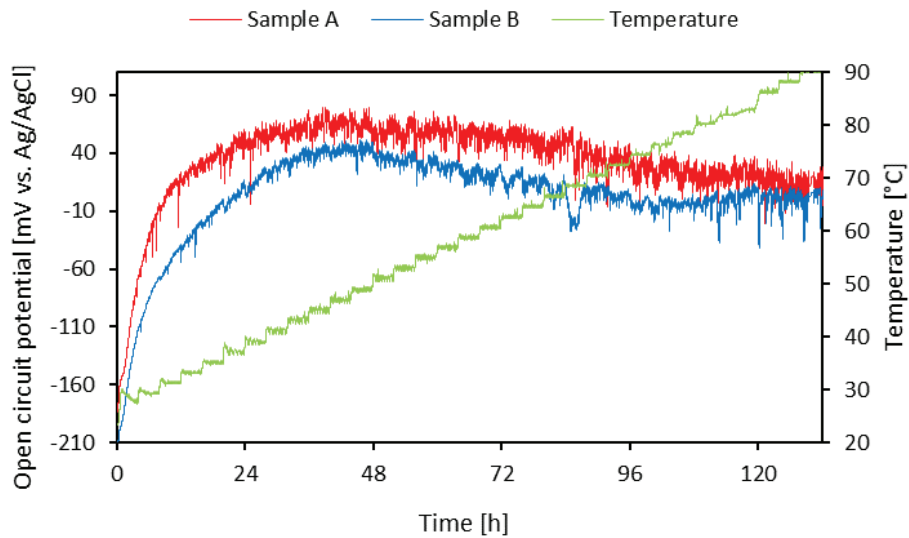

Figure 4.6: Open circuit potential development as a function of time and temperature for the TIG-welded, not pickled, coated samples exposed at OCP.

The corrosion damage underneath the coating of these samples can be seen in Figure 4.7 which shows orange corrosion products along the edge of where the paint used to be on the weld on both samples. Another sign of corrosion attacks underneath the coating are the bright areas, like the area within the dashed line in Figure 4.7a, which are present in both samples.
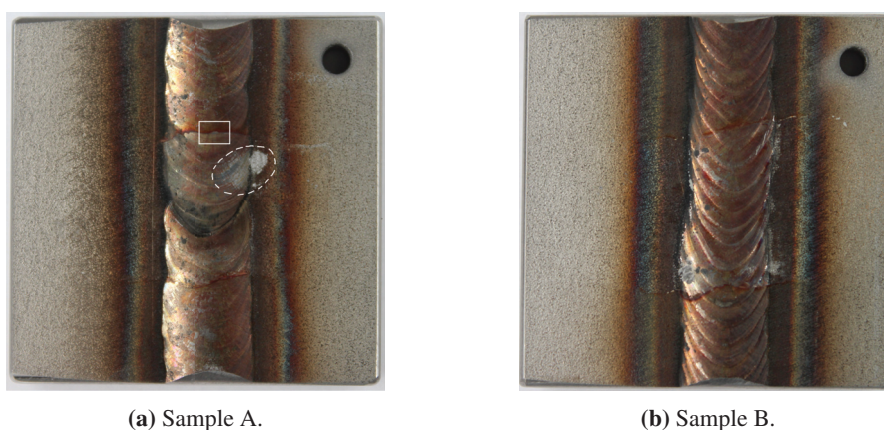
(a) Sample A.

(b) Sample B.

Figure 4.7: Corrosion attacks on the TIG-welded, not pickled, coated samples exposed at OCP.

One of these samples, the TIG-welded, not pickled, coated, Sample A, was further examined under the IFM as illustrated in Figure 4.8. The figure shows the area within the white rectangle in Figure 4.7a. This area contains a small bright spot and the orange corrosion products located at the edge of where the coating used to be. Figure 4.8

shows that this attack, like the other ones on these samples, is shallow.
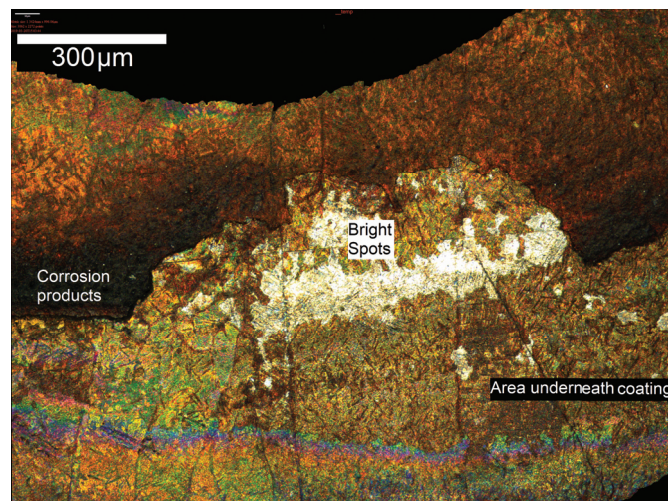
Figure 4.8: Corrosion damage along the coating edge of the TIG-welded, not pickled, coated, Sample A which was exposed at OCP.

As for the TIG-welded, pickled, coated samples exposed at OCP, these did not seem to corrode during the test, presented in Figure 4.9, which reached a temperature of 88 °C. This was evidenced by the lack of corrosion products on the surface of the samples during the test which was later confirmed with the microscope. There was also a lack of a drop in potential to a value below 0 mV vs. Ag/AgCl, which is expected from a corroding sample. In addition, it is possible to appreciate higher OCP values throughout the test than those seen with the TIG-welded, not pickled, coated samples under the same conditions. There seem to be, however, a few drops in potential in both samples. These did not originate from corrosion initiation but from other reasons. The cause of the drop in potential close to 48 hours is unknown but could be due to the data logger cabling. The drop and then sudden increase at 118 hours is due to the electrolyte evaporating to the point were one of the corners of Sample B was slightly outside of the electrolyte, and subsequent refilling of the electrolyte. At 118 hours the samples were also momentarily disconnected and connected back to the data logger. The electrolyte also evaporated significantly by the end of this test. The significant evaporation effect comes from having changed the cell to a smaller one as well as using shorter Pt wires.
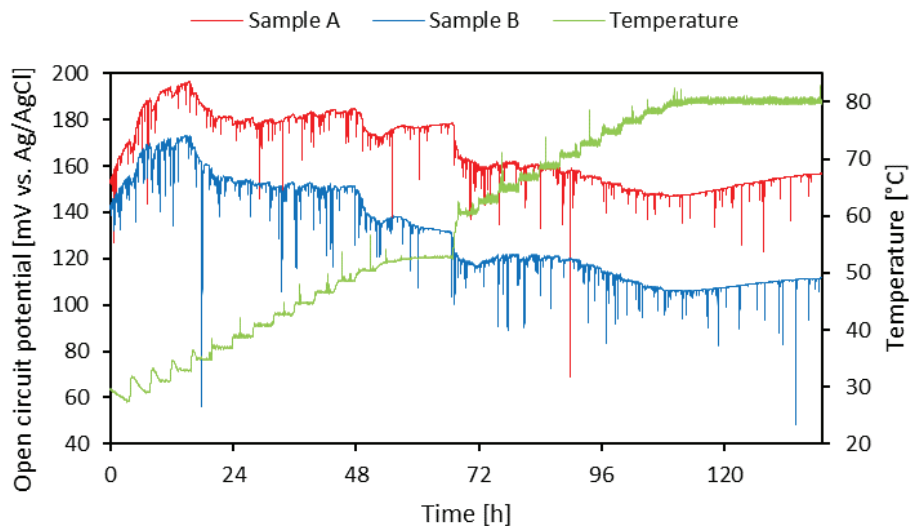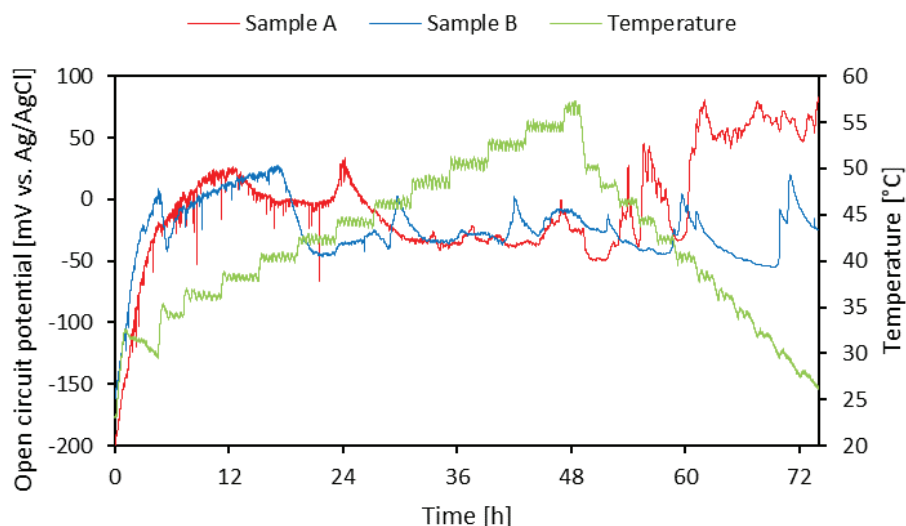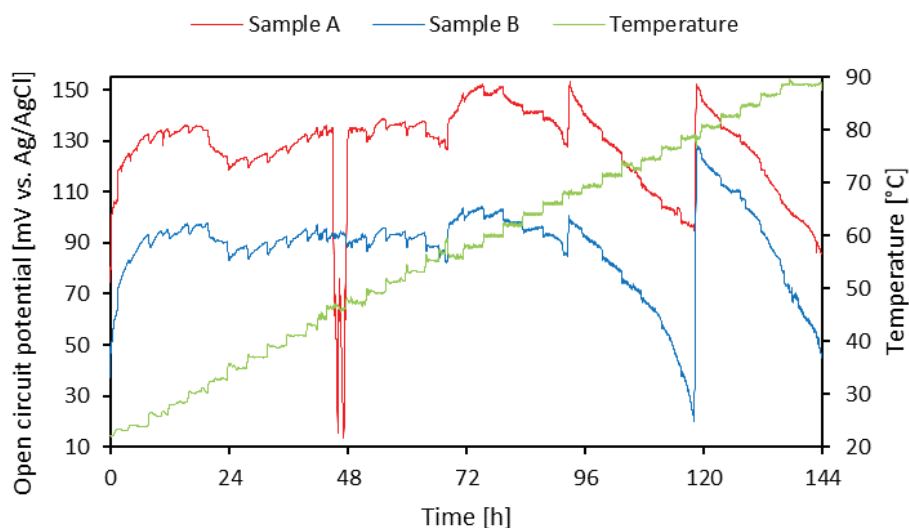

Figure 4.9: Open circuit potential development as a function of time and temperature for the TIG-welded, pickled, coated samples exposed at OCP.

Figure 4.10 shows the OCP development for the laser-welded, not pickled, coated samples exposed at OCP. The temperature regulator failed to make the electrolyte stay at room temperature at the start of the test and, instead, the temperature increased to 30 °C. After almost 3 hours at this temperature, the OCP of Sample B dropped while the OCP of Sample A remained high. Corrosion products were not seen on Sample B until after the potential drop when the temperature was 38 °C. Since the potential had already dropped significantly during the previous temperature step, T_{crit} was determined to be 36 °C. The potential drop for Sample A happened at 53 °C, however, the potential drop took place right after a fault with the temperature regulator, which lead to the temperature increasing dramatically °C. It can also be seen in Figure 4.10 that neither one of the samples repassivated.
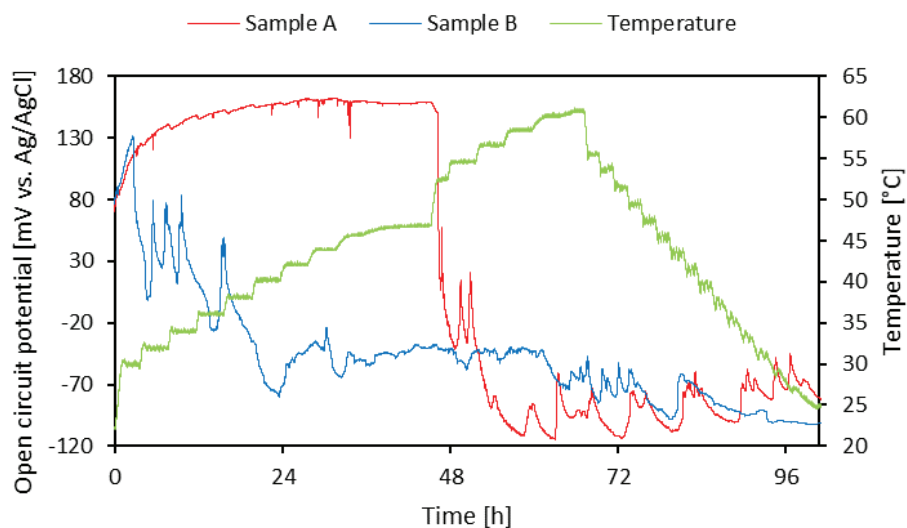
Figure 4.10: Open circuit potential development as a function of time and temperature for the laser-welded, not pickled, coated samples exposed at OCP.

The corrosion attacks on both of these laser-welded, not pickled, coated samples are shown in Figure 4.11. Both attacks initiated on the welded area underneath where the coating edge used to be.
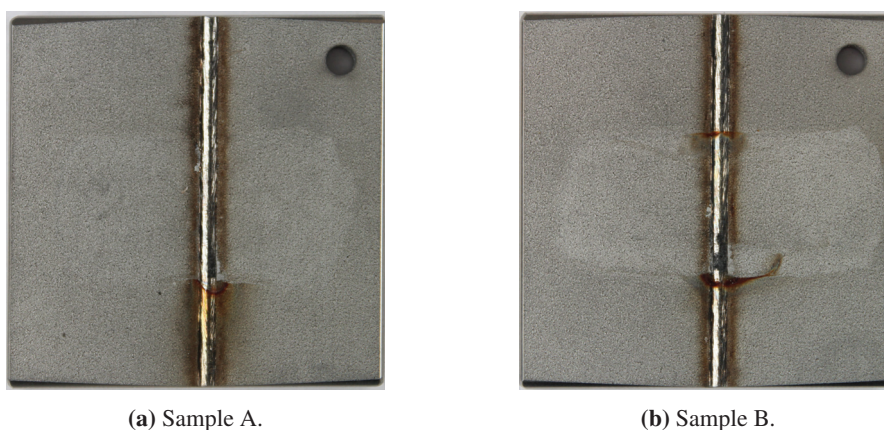
(a) Sample A.

(b) Sample B.

Figure 4.11: Corrosion attacks on the laser-welded, not pickled, coated samples exposed at OCP.

Samples polarized to +400 mV vs. Ag/AgCl

All graphs showing the critical corrosion temperature tests of samples polarized to +400 mV vs. Ag/AgCl include dashed lines at 10 and 100 $\mu A\,cm^{-2}$ marking the criteria defined in Section 4.1.2 for repassivation and initiation respectively.

Both TIG-welded, not pickled, not coated samples polarized to +400 mV vs. Ag/AgCl initiated at 53 °C and repassivated at 23 °C as shown in Figure 4.12.

Figure 4.12: Anodic current density as a function of time and temperature for the TIG-welded, not pickled, not coated samples polarized to +400 mV vs. Ag/AgCl.

Figure 4.13 shows the corrosion attacks on the TIG-welded, not pickled, not coated samples polarized to +400 mV vs. Ag/AgCl. All of the attacks initiated on the weld. At first sight, the pits present on the samples were almost unnoticeable until the affected areas were pressed with a sharp plastic tool. The thin metal surface on top of the pit then collapsed, revealing the large pits seen in Figure 4.13. This showed how most pits had a small entrance but propagated to a relatively large degree into the weld. In Figure 4.13a the largest pits in Sample A were numbered and are further referred to as Pit 1, Pit 2, etc.

(a) Sample A.

(b) Sample B.

Figure 4.13: Corrosion attacks on the TIG-welded, not pickled, not coated samples polarized to +400 mV vs. Ag/AgCl.

The largest pits in Sample A were examined further in the IFM. Figure 4.14 shows Pit 1, Figure 4.15 shows Pit 2 and 3, and Figure 4.16 shows Pit 4 and 5. Pit 1 had a depth of 1.34 mm, Pit 2 was 1.18 mm deep, Pit 3 was 1.24 mm deep deep, Pit 4 was 0.78 mm deep, and Pit 5 was 1.53 mm deep.

(a) IFM image showing corrosion attack.

(b) IFM image showing the differences in depth of the corrosion attack.

Figure 4.14: Corrosion attack in the form of pitting on the TIG-welded, not pickled, not coated Sample A (Pit 1) which was polarized to +400 mV vs. Ag/AgCl, imaged by IFM.

(a) IFM image showing corrosion attack.

(b) IFM image showing the differences in depth of the corrosion attack.

Figure 4.15: Corrosion attack in the form of pitting on the TIG-welded, not pickled, not coated Sample A (Pit 2 and 3) which was polarized to +400 mV vs. Ag/AgCl, imaged by IFM.

(a) IFM image showing corrosion attack.

(b) IFM image showing the differences in depth of the corrosion attack.

Figure 4.16: Corrosion attack in the form of pitting on the TIG-welded, not pickled, not coated Sample A (Pit 4 and 5) which was polarized to +400 mV vs. Ag/AgCl, imaged by IFM, showing the deepest pit on the sample.

Only one sample was tested in the TIG-welded, pickled, not coated condition. Figure 4.17 shows this sample initiated at 72 °C and repassivated at 24 °C.

Figure 4.17: Anodic current density as a function of time and temperature for the TIG-welded, pickled, not coated sample polarized to +400 mV vs. Ag/AgCl.

Figure 4.21 shows the corrosion attacks on the TIG-welded, pickled, not coated sample polarized to +400 mV vs. Ag/AgCl. Similarly to its not-pickled counterparts, the size of the pits could not be appreciated until the surface of the material was pressed with a sharp plastic tool.
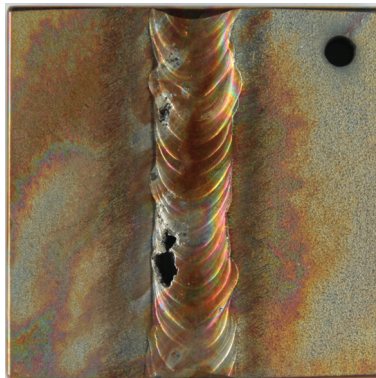
Figure 4.18: Corrosion attacks on the TIG-welded, pickled, not coated sample polarized to +400 mV vs. Ag/AgCl.

The largest pit in the sample was imaged in the IFM as shown in Figure 4.19. The pit reached a depth of 2.12 mm.
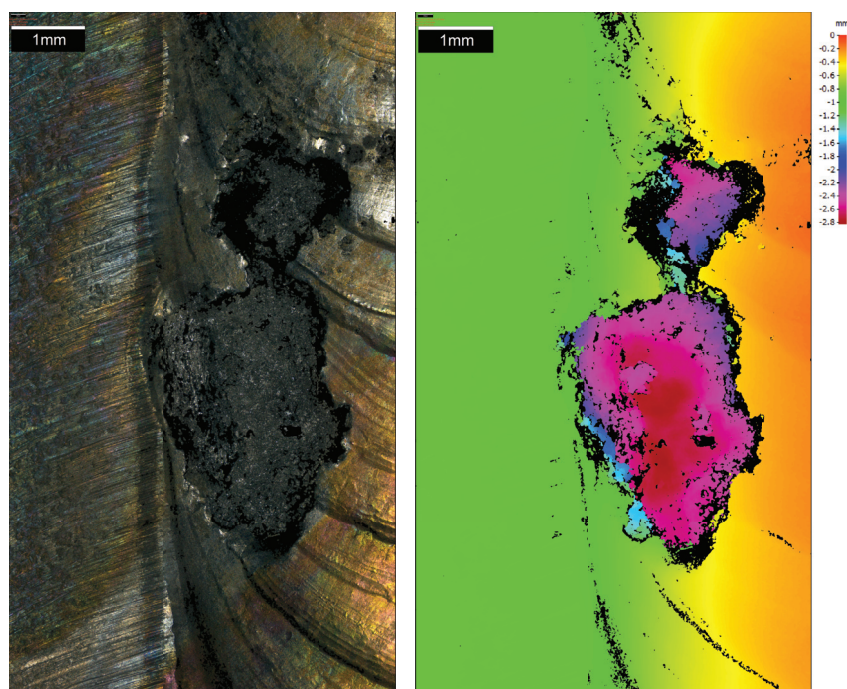
(a) IFM image showing corrosion attack.

(b) IFM image showing the differences in depth of the corrosion attack.

Figure 4.19: Corrosion attack in the form of pitting on the TIG-welded, pickled, not coated sample which was polarized to +400 mV vs. Ag/AgCl, imaged by IFM.

As for the laser-welded, not pickled, not coated samples polarized to +400 mV vs. Ag/AgCl, Sample A initiated when the temperature reached 46 °C and Sample B initiated at 48 °C. In terms of repassivation, only Sample B managed to repassivate at 25 °C while Sample A continued to corrode. These results are shown in Figure 4.20.
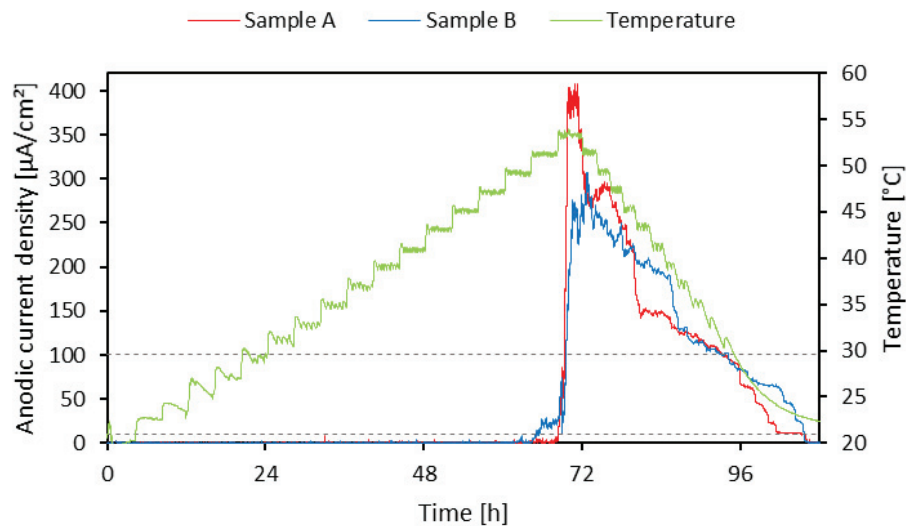

Figure 4.20: Anodic current density as a function of time and temperature for the laser-welded, not pickled, not coated samples polarized to +400 mV vs. Ag/AgCl.

The corrosion attacks on both laser-welded, not pickled, not coated samples are shown in Figure 4.21. As it can be seen in this figure, the corrosion damage is extensive and it initiated in the welded area exclusively. In Sample A, the depth of the damage reached 1.69 mm, whereas in Sample B the damage reached a depth of 2.57 mm.
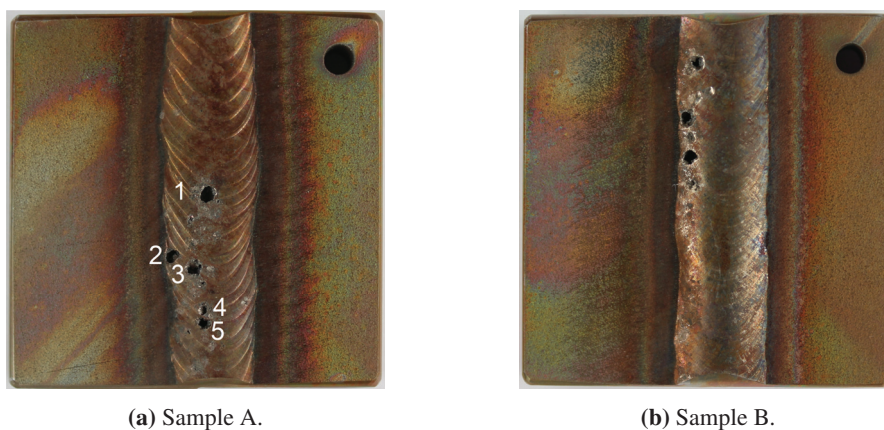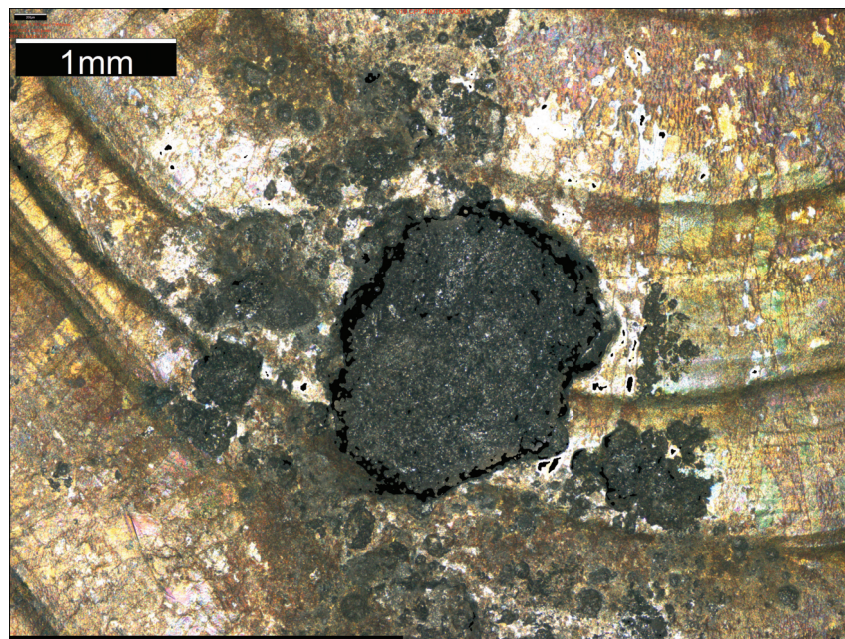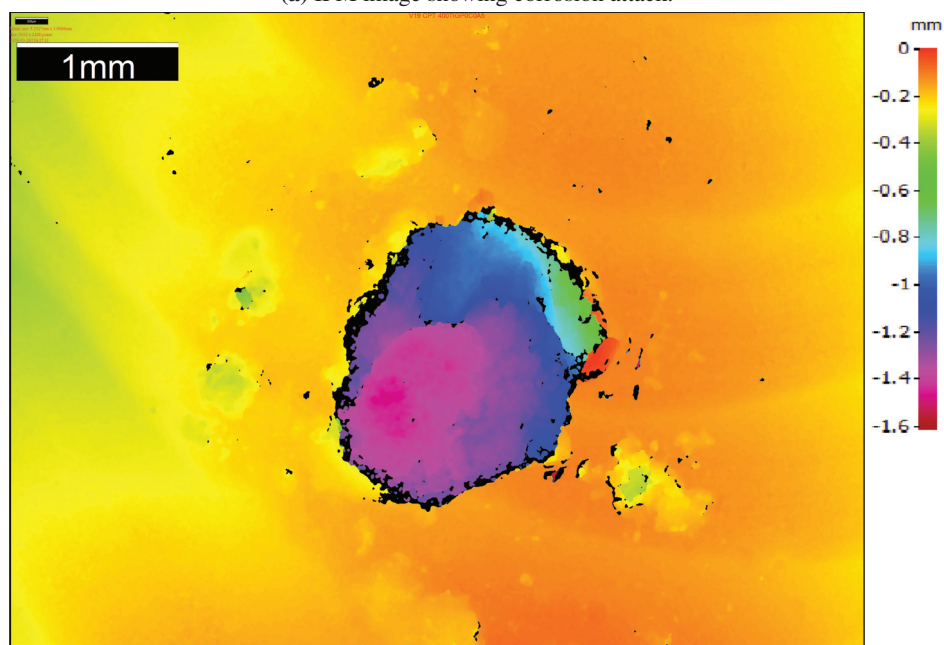

(a) Sample A.

(b) Sample B.

Figure 4.21: Corrosion attacks on the laser-welded, not pickled, not coated samples polarized to +400 mV vs. Ag/AgCl.

In the case of the coated samples, Figure 4.22 shows the TIG-welded, not pickled, coated Sample A initiated at 47 °C and repassivated at 23, while Sample B's anodic current density exceeded 100 $\mu A\,cm^{-2}$ only for approximately 6 minutes at 50 °C before going down. The anodic current density of Sample B exceeded 100 $\mu A\,cm^{-2}$ again at 53 °C where it experienced a sharp increase, and, later on, repassivated at 22 °C.
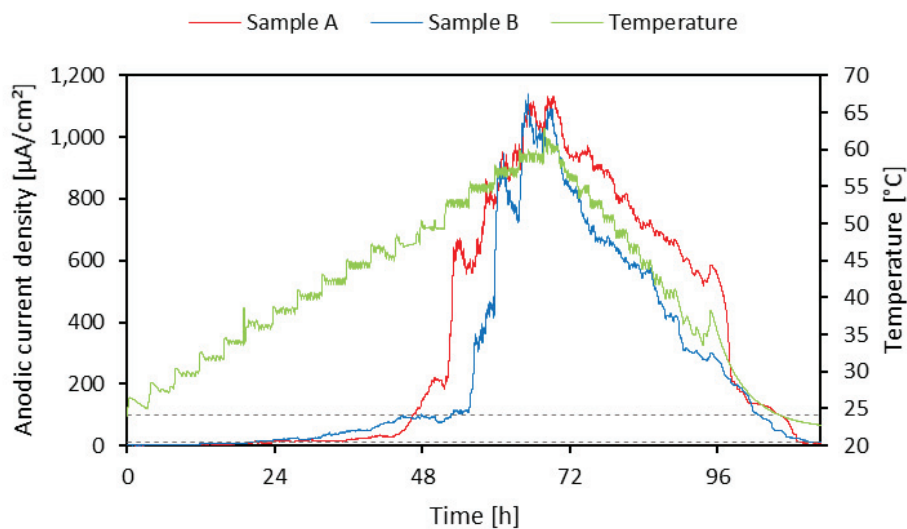
Figure 4.22: Anodic current density as a function of time and temperature for the TIG-welded, not pickled, coated samples polarized to +400 mV vs. Ag/AgCl.

The corrosion attacks on both samples are shown in Figure 4.23. On both samples, the greatest mass loss took place underneath the coating edge on top of the weld. Sample A not only experienced crevice corrosion underneath the coating but also pitting corrosion on the weld.

(a) Sample A.

(b) Sample B.

Figure 4.23: Corrosion attacks on the TIG-welded, not pickled, coated samples polarized to +400 mV vs. Ag/AgCl.

Examining the surface of the samples, the maximum depth of each corrosion attack at the crevice was 0.41 mm for Sample A and 0.25 for Sample B. Sample A was examined with the IFM as shown in Figure 4.24.

(a) IFM image showing corrosion attack.
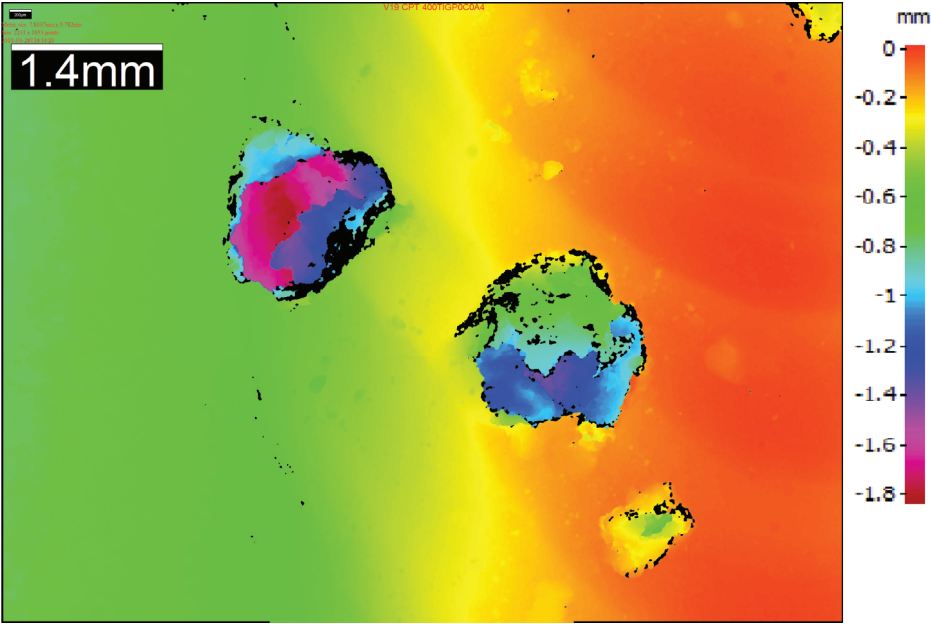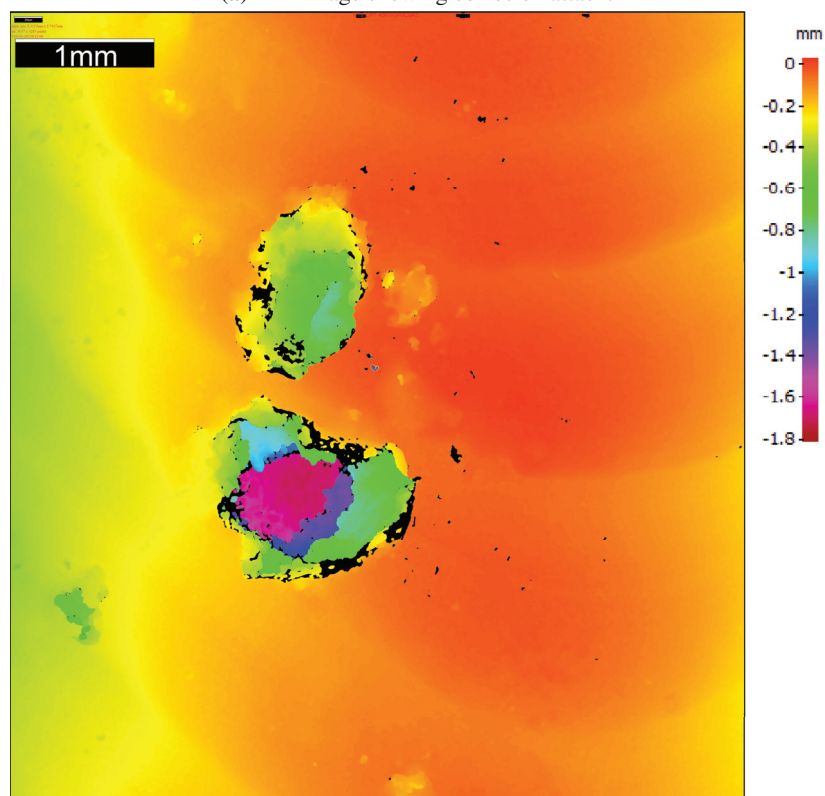

(b) IFM image showing the differences in depth of the corrosion attack.
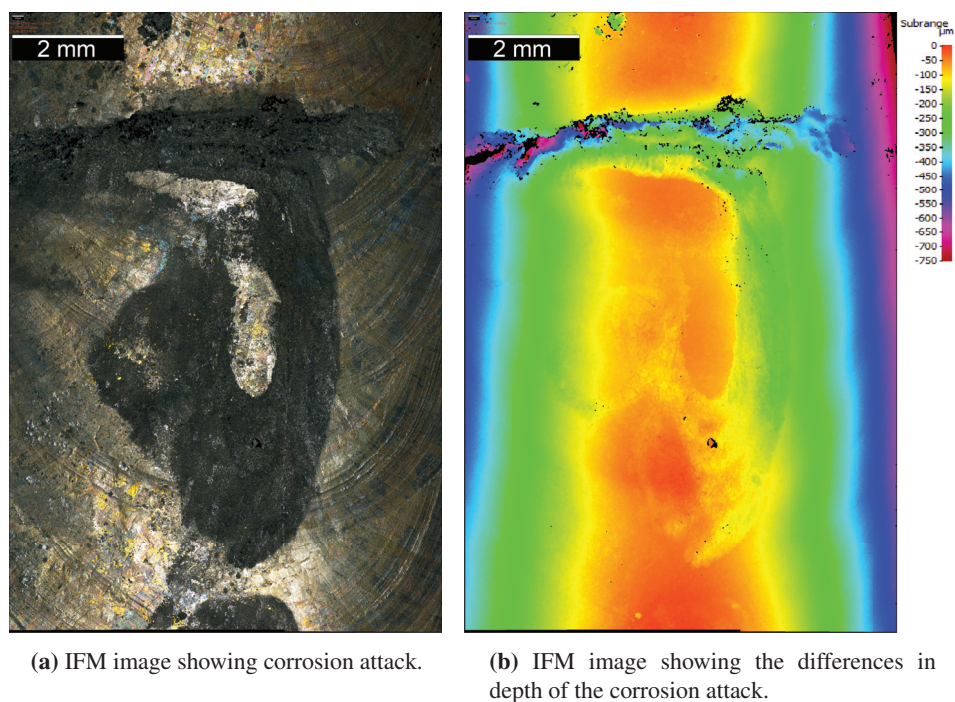
Figure 4.24: Crevice corrosion attack on the TIG-welded, not pickled, coated Sample A which was polarized to +400 mV vs. Ag/AgCl, imaged by IFM.

Sample A was cut perpendicularly to the weld and along the crevice for the SEM/EDS analysis. This unveiled the fact that the crevice had propagated further into the material than what was originally seen by examining the surface of the corroded sample. The cross-section cut, pictured in Figure 4.25, revealed that the crevice damage was as deep as approximately 2.5 mm.

Figure 4.25: Cross-section of crevice corrosion attack on the TIG-welded, not pickled, coated Sample A which was polarized to +400 mV vs. Ag/AgCl, imaged by IFM.

The TIG-welded, pickled, coated samples initiated at 44 °C and 51 °C respectively for Sample A and Sample B, as shown in Figure 4.26. Even though Sample A experienced a large drop in anodic current density, it still did not manage to repassivate as the anodic current density was never stable below 10 $\mu A\,cm^{-2}$. Sample B, on the other hand, repassivated at 30 °C.
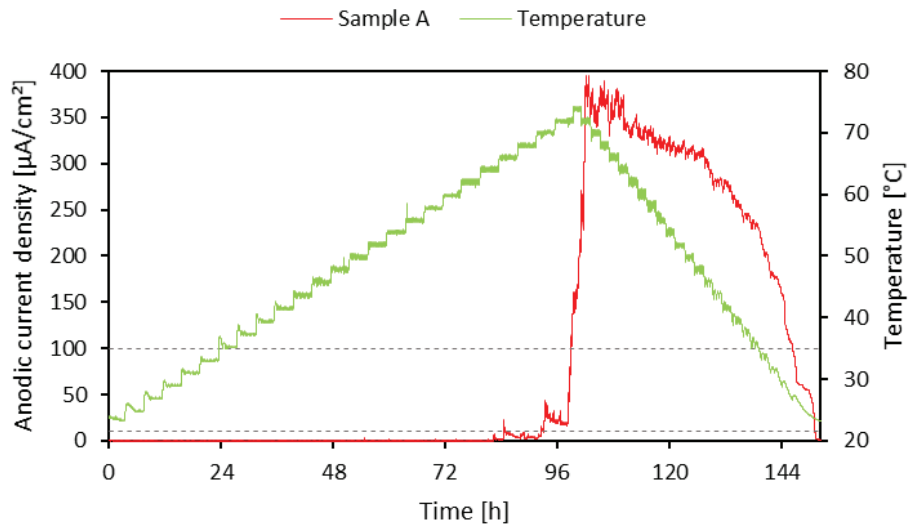

Figure 4.26: Anodic current density as a function of time and temperature for the TIG-welded, pickled, coated samples polarized to +400 mV vs. Ag/AgCl.

Figure 4.27a shows that Sample A experienced extensive crevice corrosion damage underneath the coating on top of the weld cap, as well as some damage on the HAZ and base material underneath the coating. Similar damage can be seen in Figure 4.27b where the crevice corrosion damage occurred on both coating edges on top of the weld cap, as well as in the HAZ and base material although to a lesser extent.
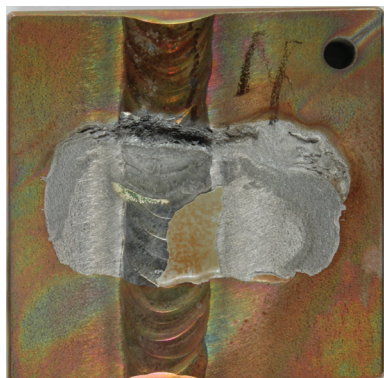
(a) Sample A.

(b) Sample B.

Figure 4.27: Corrosion attacks on the TIG-welded, pickled, coated samples polarized to +400 mV vs. Ag/AgCl.

It is worth noting that the corrosion attack on Sample A initiated at the scratch near the top right corner of the coating seen in Figure 4.27a. This area was examined under the IFM as shown in Figure 4.28.
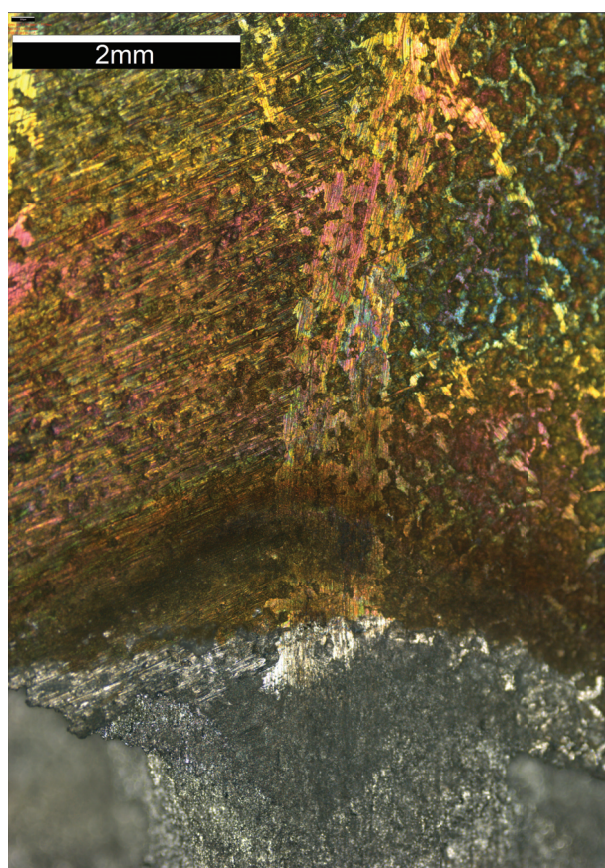
Figure 4.28: Scratch where corrosion initiated on the TIG-welded, pickled, coated Sample A which was polarized to +400 mV vs. Ag/AgCl, imaged by IFM.

The crevice corrosion damage on the weld in Sample A reached a depth of 1.70 mm. The crevice corrosion damage on top of the weld of this sample was inspected further in the IFM as shown in Figure 4.29.

(a) IFM image showing corrosion attack.

(b) IFM image showing the differences in depth of the corrosion attack.
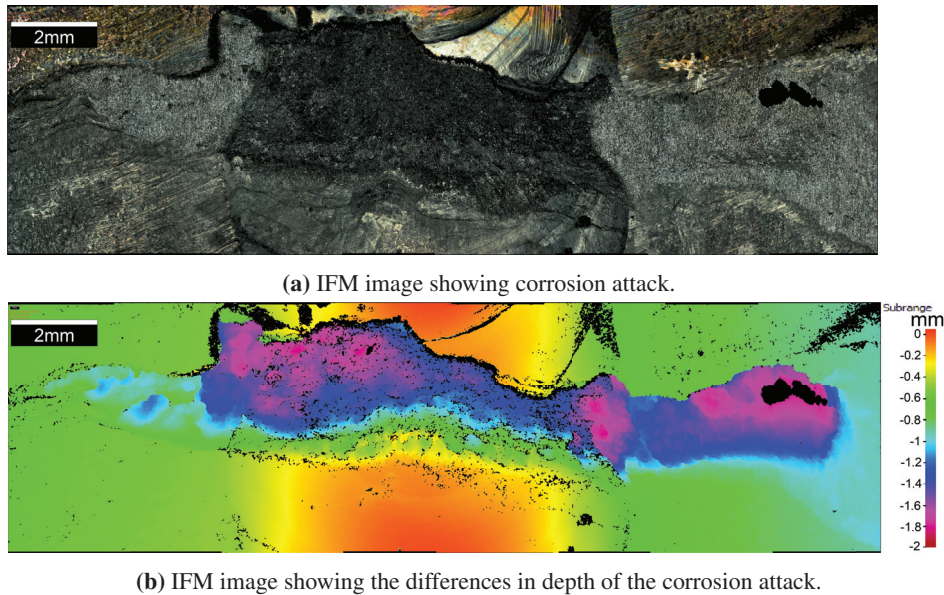
Figure 4.29: Crevice corrosion attack on the TIG-welded, pickled, coated Sample A which was polarized to +400 mV vs. Ag/AgCl, imaged by IFM.

The temperatures of initiation for the laser-welded, not pickled, coated samples are 41 °C and 45 °C, for Sample A and Sample B respectively. As shown in Figure 4.30, neither of these samples repassivated as the temperature decreased to 24 °C.
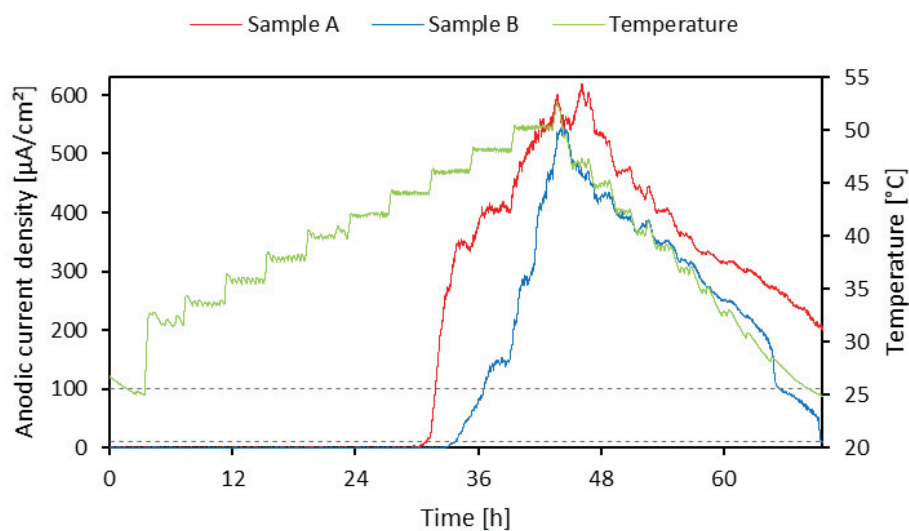

Figure 4.30: Anodic current density as a function of time and temperature for the laser-welded, not pickled, coated samples polarized to +400 mV vs. Ag/AgCl.

The damage in both samples initiated at the weld area where the damage is also more acute as seen in Figure 4.31. It can also be seen that the area that was underneath the coating on the base material was also affected.

(a) Sample A.　　　　　　　　　　　　　**(b)** Sample B.
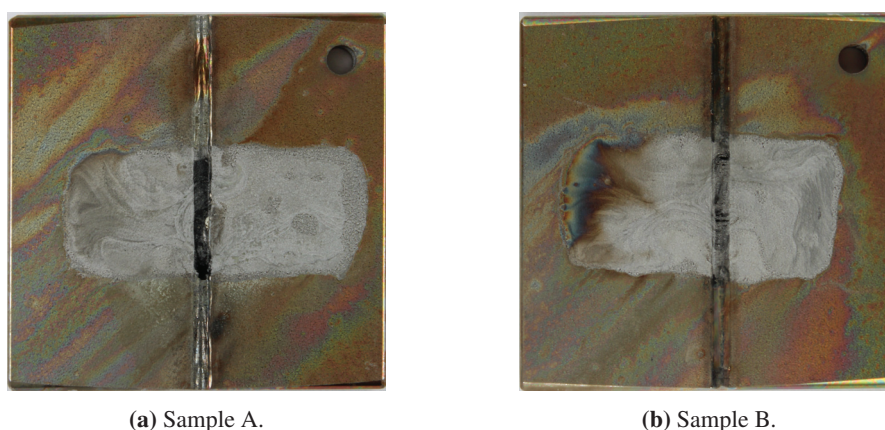
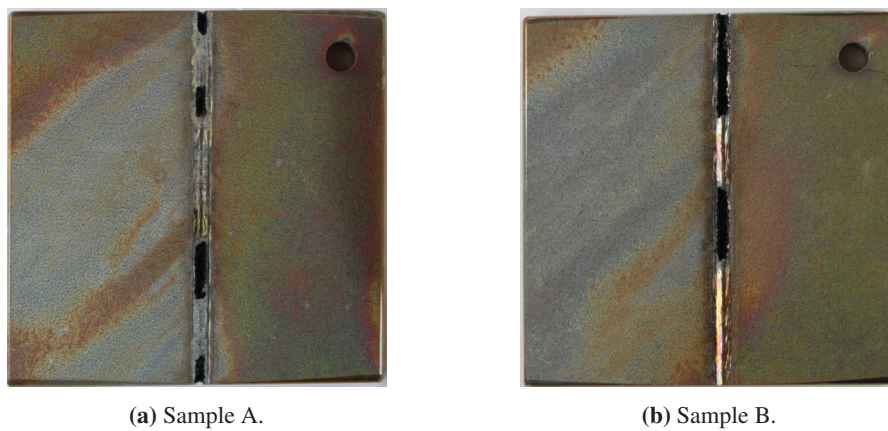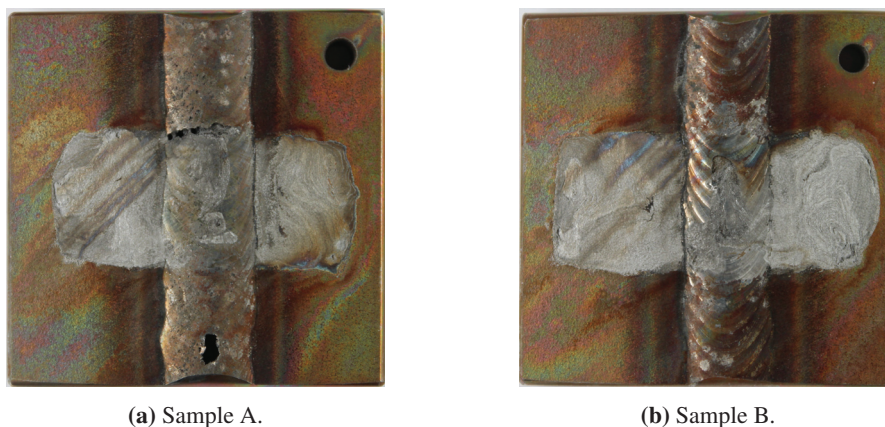**Figure 4.31:** Corrosion attacks on the laser-welded, not pickled, coated samples polarized to +400 mV vs. Ag/AgCl.

As for the samples that were polarized cathodically to -1100 mV vs. Ag/AgCl for a week, the cathodic current density was plotted as a function of time for the duration of the polarization, as shown in Figure 4.32
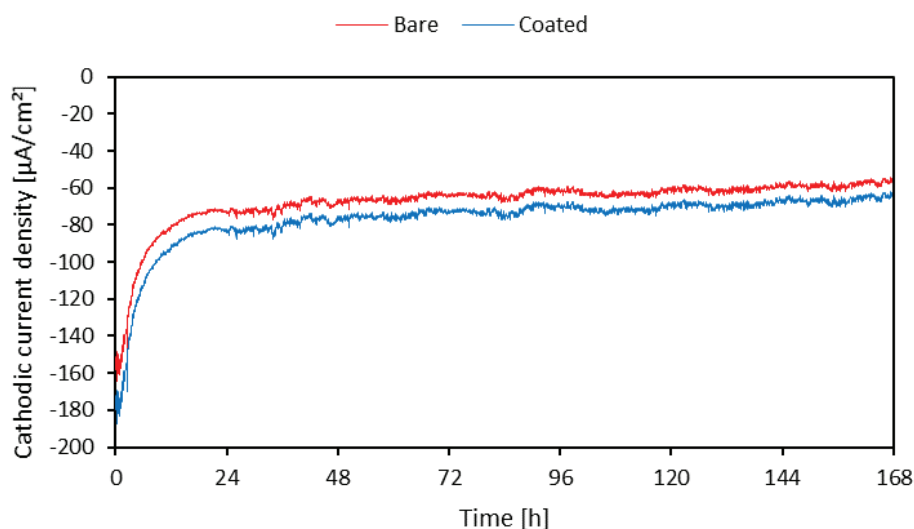
Figure 4.32: Cathodic current density as a function of time, expressed in hours, for the TIG-welded, pickled, bare and coated samples polarized to -1100 mV vs. Ag/AgCl for a week before critical corrosion testing.

The pH of the electrolyte used in the cathodic polarization was measured after the 1-week polarization. The pH measurement revealed that the pH of the electrolyte had decreased, for unknown reasons, as it was measured to be 3.95 whereas the pH of untested natural seawater was measured to be 7.93. The samples, however, managed to develop calcareous deposits, meaning the pH increased locally at the surface of the samples. In terms of the polarization itself, a lower pH of the electrolyte leads to a higher reversible potential of the hydrogen evolution reaction, which then leads to a higher hydrogen charging current density. This aspect is not quite problematic since the effect of CP in general is the priority of the investigation and not the specific value of the current.

After one week of cathodic polarization, followed by an hour immersed at OCP, the TIG-welded, pickled, bare and coated samples were polarized anodically to +400 mV vs. Ag/AgCl . Both samples corroded at 24 °C and did not repassivate as shown in Figure 4.33. Unfortunately, the temperature increased after three hours instead of the planned four hours.

After one hour of anodic polarization (+400 mV vs. Ag/AgCl) both samples already showed signs of initiation of corrosion in the form of brown corrosion products on the HAZ and weld area. It can be seen in Figure 4.30 that
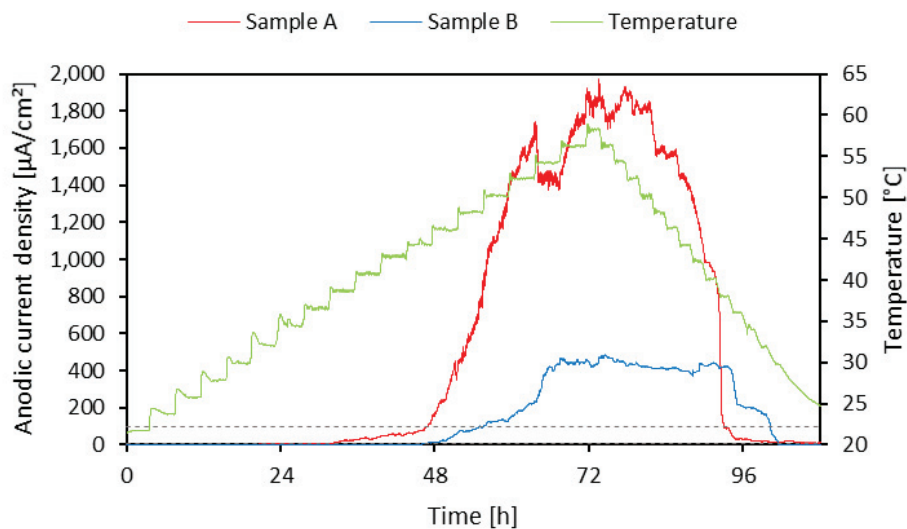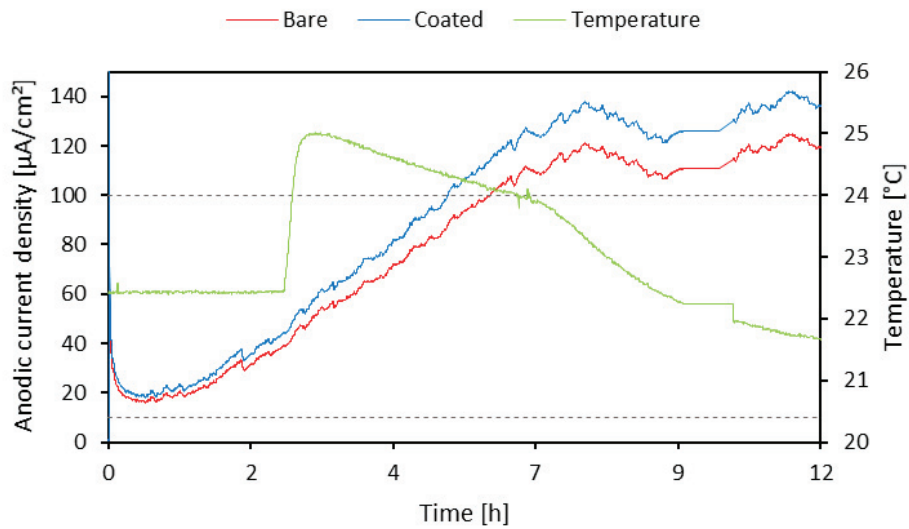
Figure 4.33: Anodic current density as a function of time and temperature for the TIG-welded, pickled, bare and coated samples while being polarized to +400 mV vs. Ag/AgCl after one week of cathodic polarization.

the anodic current density of the samples never reached zero, including the beginning of the anodic polarization where the sample had just been exposed at OCP for an hour. In addition, after one week of cathodic polarization, all samples had developed a fair amount of calcareous deposits throughout the sample surfaces. The corrosion damage on the samples can be observed in Figure 4.34 and some of the calcareous deposits are pointed out in Figure 4.34c.

(a) Front side of bare sample.

(b) Front side of coated sample.
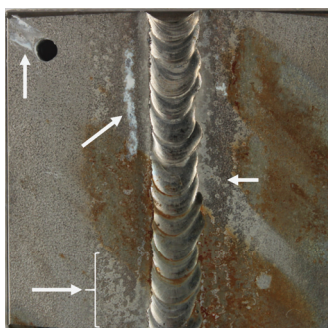
(c) Back side of bare sample.

(d) Back side of coated sample.

Figure 4.34: Corrosion attacks and calcareous deposits on the TIG-welded, pickled, bare and coated samples polarized to +400 mV vs. Ag/AgCl after one week of cathodic polarization.

For both materials, the corrosion attacks on the HAZ are superficial, whereas some of the damage in the weld area was more severe. In the case of the bare sample, when pressing the surface with a sharp plastic tool, one of the affected areas, pictured in Figure 4.35, collapsed, indicating pitting. The surface of the occluded pits could not be removed so the actual depth of the pits could not be determined.
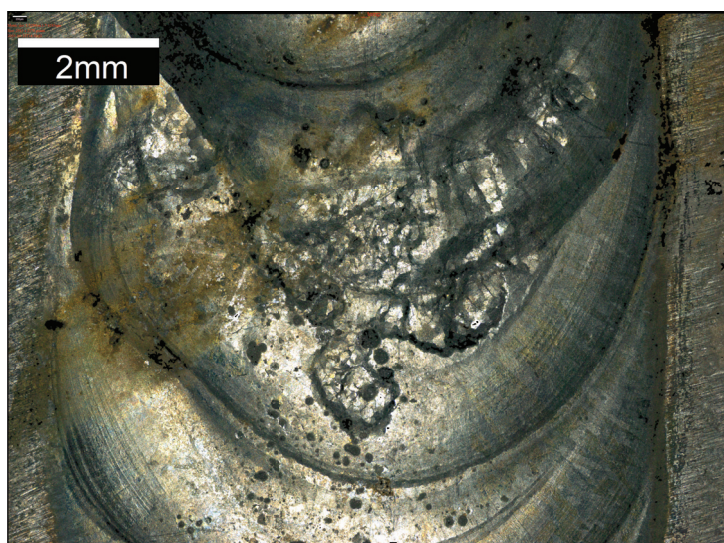
Figure 4.35: Corrosion attack in the form of pitting on the TIG-welded, pickled, not coated sample which was polarized to +400 mV vs. Ag/AgCl after one week of cathodic polarization, imaged by IFM.

It can be seen in Figure 4.34b that the coated sample has two major corrosion attacks, one of them outside the coating at the top of the weld area and another which is adjacent to the coating but that propagated outside of the coating. The corrosion attack adjacent to the coating was then analyzed in the IFM, as shown in Figure 4.36, where it was determined that this corrosion damage reached a depth of 0.19 mm.
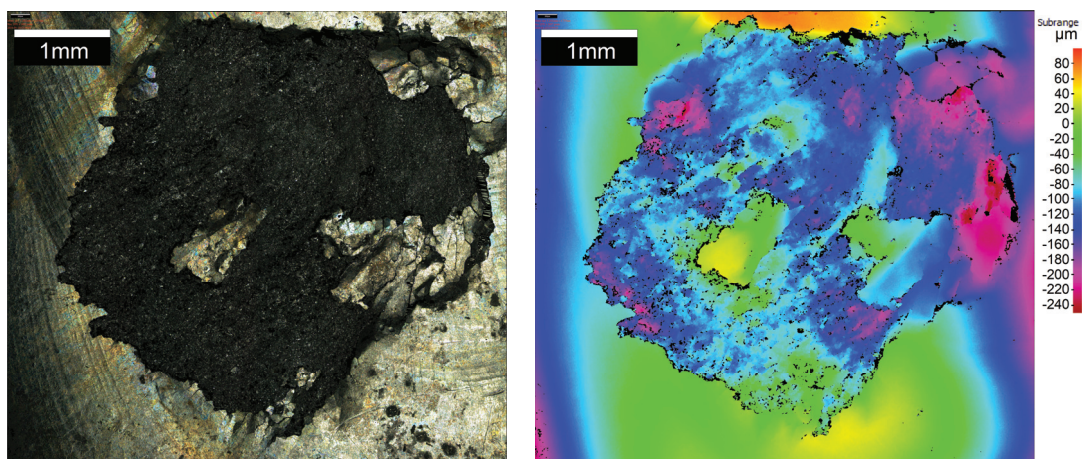
(a) IFM image showing corrosion attack.

(b) IFM image showing the differences in depth of the corrosion attack.

Figure 4.36: Corrosion attack adjacent to the coating on the TIG-welded, pickled, coated sample which was polarized to +400 mV vs. Ag/AgCl after one week of cathodic polarization, imaged by IFM.

The base material (not pre-cathodically polarized) polarized to +400 mV vs. Ag/AgCl, on the other hand, did not initiate corrosion for the entirety of the test which ran until 89 °C, as seen in Figure 4.37.
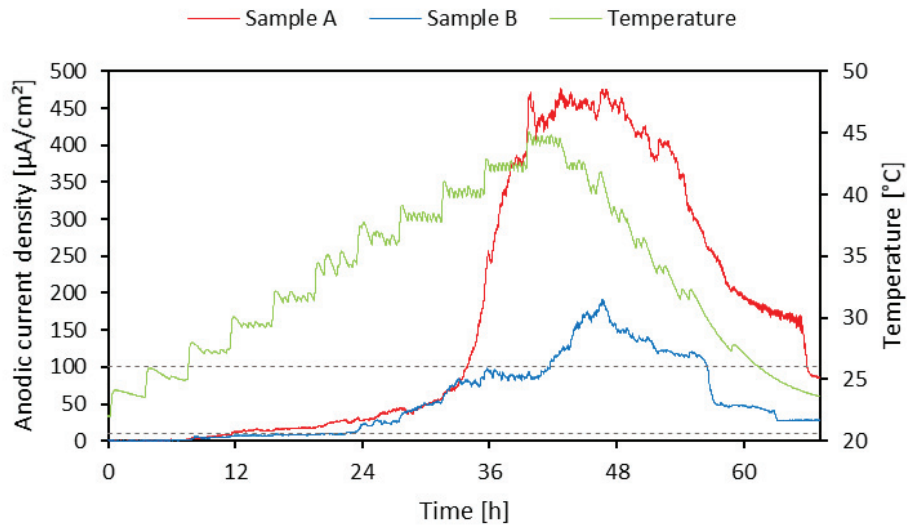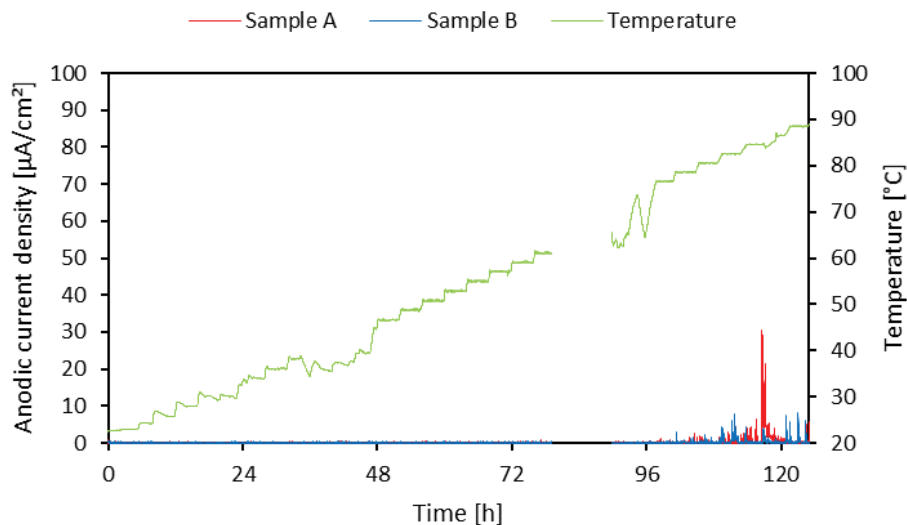

Figure 4.37: Anodic current density as a function of time and temperature for the base material, not pickled pickled, samples polarized to +400 mV vs. Ag/AgCl.

At temperatures above 80 °C, the anodic current density of the samples increased from zero and briefly reached a maximum of 30.56 $\mu A\,cm^{-2}$ for Sample A, and 8.13 $\mu A\,cm^{-2}$ for Sample B. This caused some superficial corrosion attacks, considered to be metastable pitting, seen in Figure 4.38.
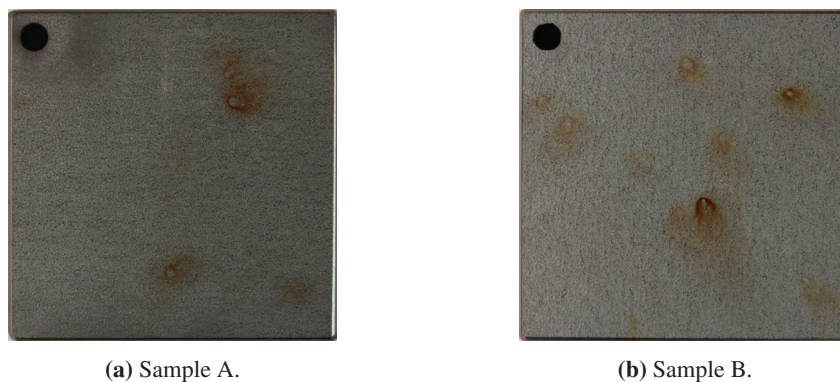
(a) Sample A.

(b) Sample B.

Figure 4.38: Superficial corrosion attacks on the base material polarized to +400 mV vs. Ag/AgCl.

4.2.2 Long-term exposure

The OCP development as a function of time and temperature of the samples exposed at OCP in the long-term test are illustrated in Figure 4.39. The data logging began as the electrolyte was at room temperature (during day -1) and ended after 60 days at 40 °C. No data could be logged from day 44 to day 48. The TIG-welded, not pickled, coated sample exposed at OCP began to show signs of corrosion in the form of brown rust around the coating on the weld before the temperature was increased to 40 °C. On the other hand, both the TIG-welded, pickled, coated sample and the laser-welded, not pickled, coated sample did not show any signs of corrosion during the test.
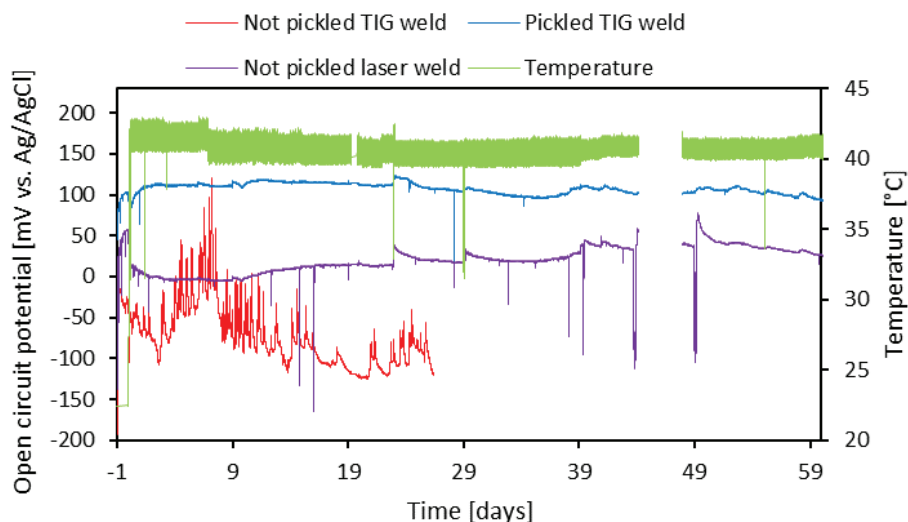
Figure 4.39: Open circuit potential development as a function of time and temperature, expressed in days and degrees Celsius respectively, for all the coated samples exposed at OCP during the long-term exposure test.

The anodic current density as a function of time and temperature of the samples polarized to +400 mV vs. Ag/AgCl in the long-term test is illustrated in Figure 4.40. Both the TIG-welded, not pickled, coated sample and the laser-welded, not pickled, coated sample had visible corrosion products around the coating on the weld before the temperature was increased to 40 °C. The TIG-welded, not pickled, coated sample did not reach 100 µA cm^{-2} in anodic current density, but was still removed lest it pollute the water any further with corrosion products. The TIG-welded pickled, coated sample, however, did not show any signs of corrosion until day 16 and reached 100 µA cm^{-2} after day 19.
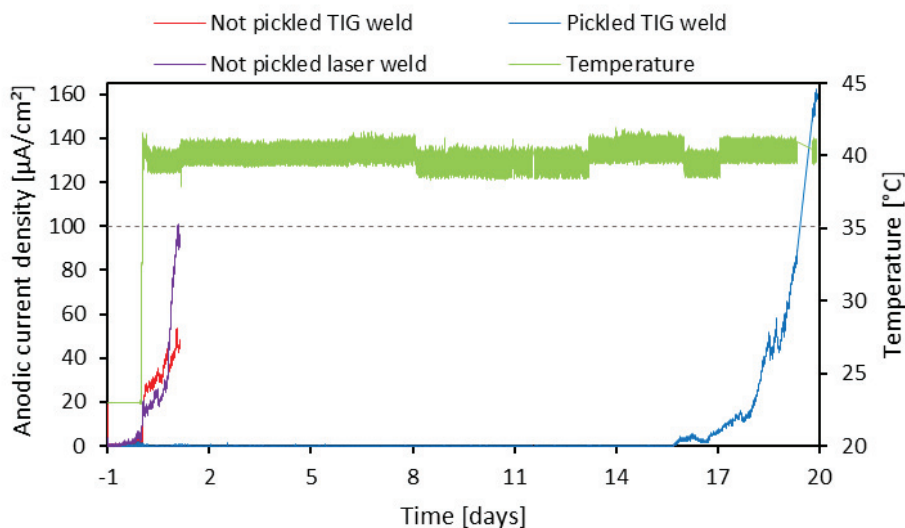
Figure 4.40: Anodic current density as a function of time and temperature for all the coated samples polarized to +400 mV vs. Ag/AgCl during the long-term exposure test.

4.2.3 Surface characterization

SEM/EDS

Three different tested samples were inspected with the SEM, the TIG-welded, not pickled, coated Sample A exposed at OCP, the TIG-welded, not pickled, not coated Sample A polarized to +400 mV vs. Ag/AgCl and the TIG-welded, not pickled, coated Sample A polarized to +400 mV vs. Ag/AgCl. In addition, EDS analysis was also performed in some of the areas imaged by the SEM.

Figure 4.41 shows the corroded area where the coating edge used to be. The area underneath the coating and adjacent to the corrosion damage at the edge of the coating was imaged in more detail in Figure 4.42.
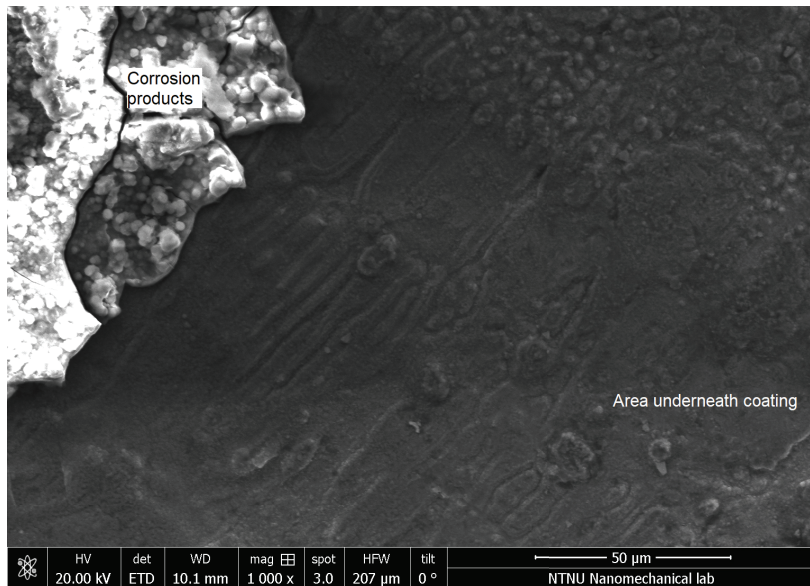
Figure 4.41: SEM image of the TIG-welded, not pickled, coated Sample A exposed at OCP showing the area where the coating edge used to be next to the corrosion products at 1000X magnification.
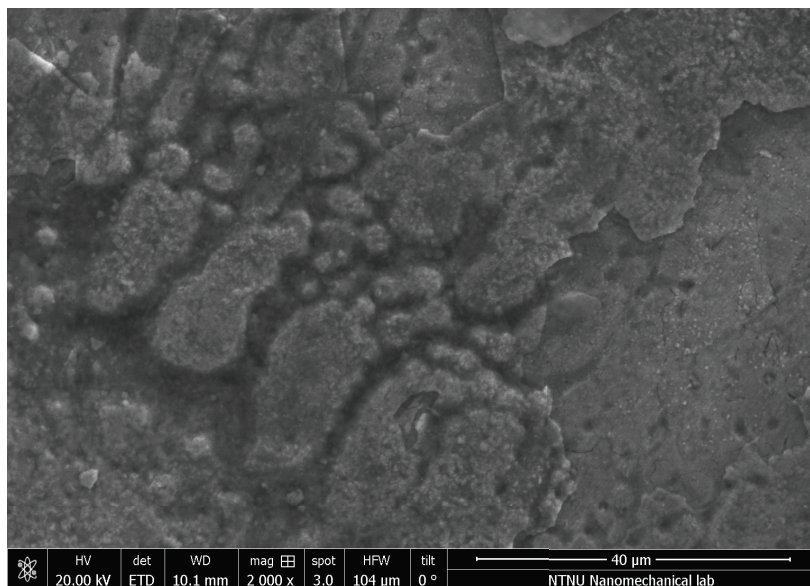
Figure 4.42: SEM image of the TIG-welded, not pickled, coated Sample A exposed at OCP showing the area underneath the coating close to the coating edge at 2000X magnification.

A section showing the corrosion damage along the coating edge of the TIG-welded, not pickled, coated Sample A exposed at OCP was examined by SEM/EDS, as indicated in Figure 4.43.
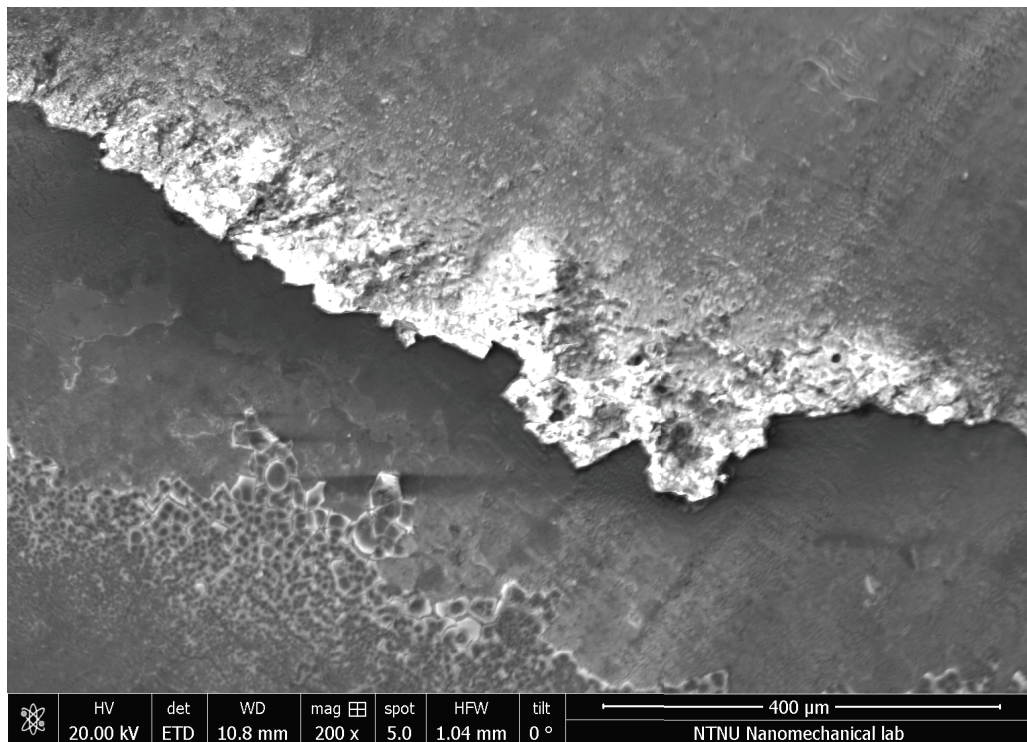
(a) SEM image displaying area analyzed.
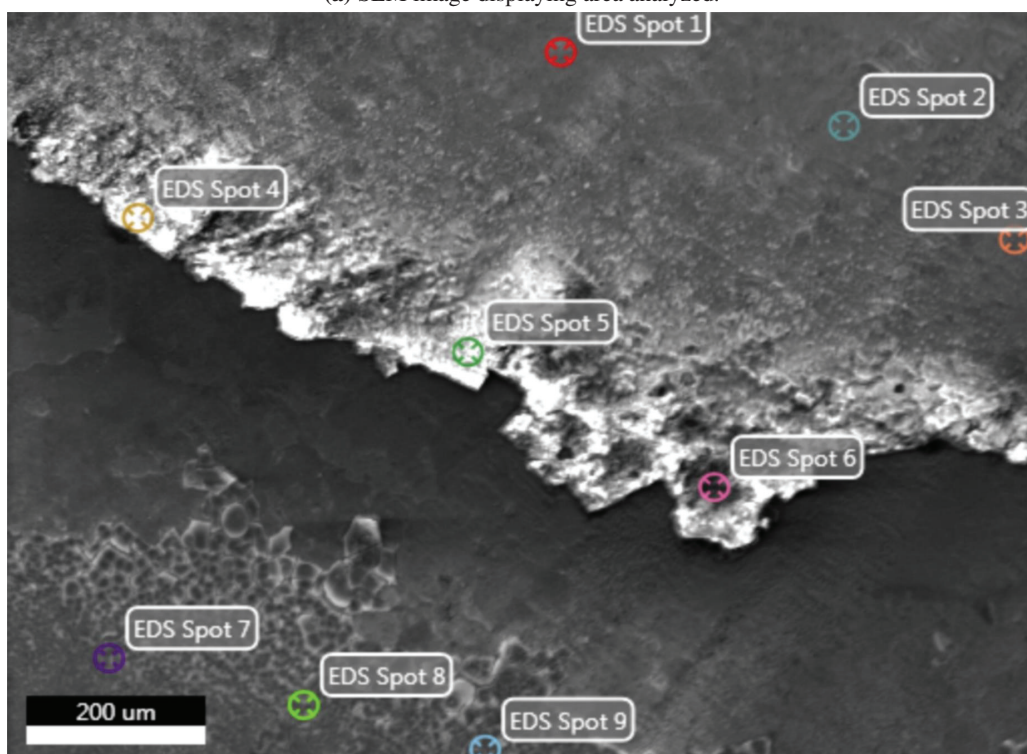
(b) EDS image displaying spots selected for analysis.

Figure 4.43: Corrosion damage along the coating edge of the TIG-welded, not pickled, coated Sample A exposed at OCP analyzed by SEM/EDS.

Spot 1-3, seen in Figure 4.43, correspond to the material outside of the coating, while Spot 4-6 correspond to the corrosion products adjacent to the coating edge, and Spot 7-9 correspond to the area underneath the coating. Table 4.5 shows that the highest PRE_N* attained were in the area underneath the coating while the generally lowest PRE_N* were found outside the crevice. The highest amounts of O are found outside of where the coating was.

Table 4.5: Composition of each element, expressed as weight percentage, found through EDS analysis for each spot in the area shown in Figure 4.43b, together with the calculated PRE_N* for the TIG-welded, not pickled, coated Sample A exposed at OCP.

| Spot number | Composition [wt%] | | | | | | | | | PRE_N* |
	C	O	Mg	Si	Mo	Cr	Mn	Fe	Ni	
1	8.64	24.80	-	0.33	0.98	16.91	-	45.80	2.53	20.14
2	4.17	22.60	-	0.30	1.31	18.18	1.96	48.27	3.21	22.50
3	9.14	26.12	0.97	0.52	1.17	15.96	1.08	42.96	2.08	19.82
4	7.13	33.24	-	0.17	2.61	17.19	-	39.67	-	25.80
5	7.56	31.66	-	0.12	1.71	11.39	-	47.56	-	17.03
6	5.63	26.15	-	0.18	3.29	20.72	-	44.03	-	31.58
7	3.06	19.10	-	0.28	3.94	28.27	-	41.79	3.56	41.27
8	10.48	22.51	-	0.38	3.49	24.43	1.16	34.70	2.85	35.95
9	7.16	24.53	-	0.41	4.49	24.18	-	36.73	2.49	39.00

Figure 4.44, 4.45 and 4.46 show the inside of Pit 1, 2 and 3 respectively, of the TIG-welded, not pickled, not coated Sample A which was polarized to +400 mV vs. Ag/AgCl.

| HV | det | WD | mag ⊞ | spot | HFW | tilt | 50 μm |
| 20.00 kV | ETD | 11.4 mm | 1 500 x | 3.0 | 138 μm | 0 ° | NTNU Nanomechanical lab |
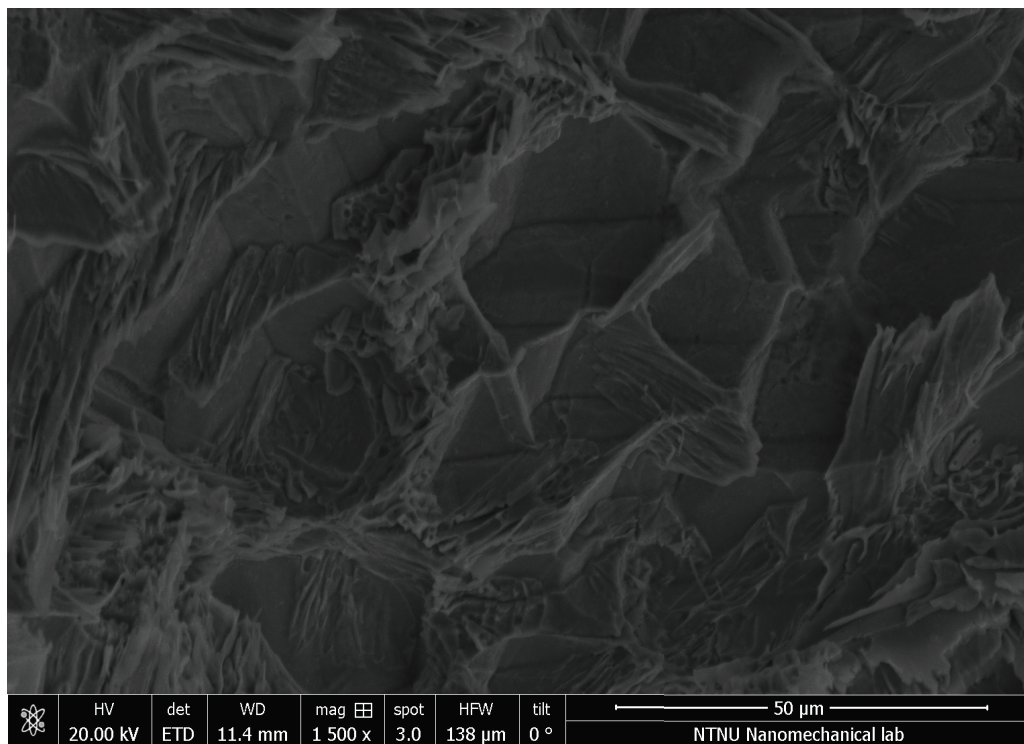
Figure 4.44: SEM image of the inside of Pit 1 of the TIG-welded, not pickled, not coated Sample A which was polarized to +400 mV vs. Ag/AgCl..
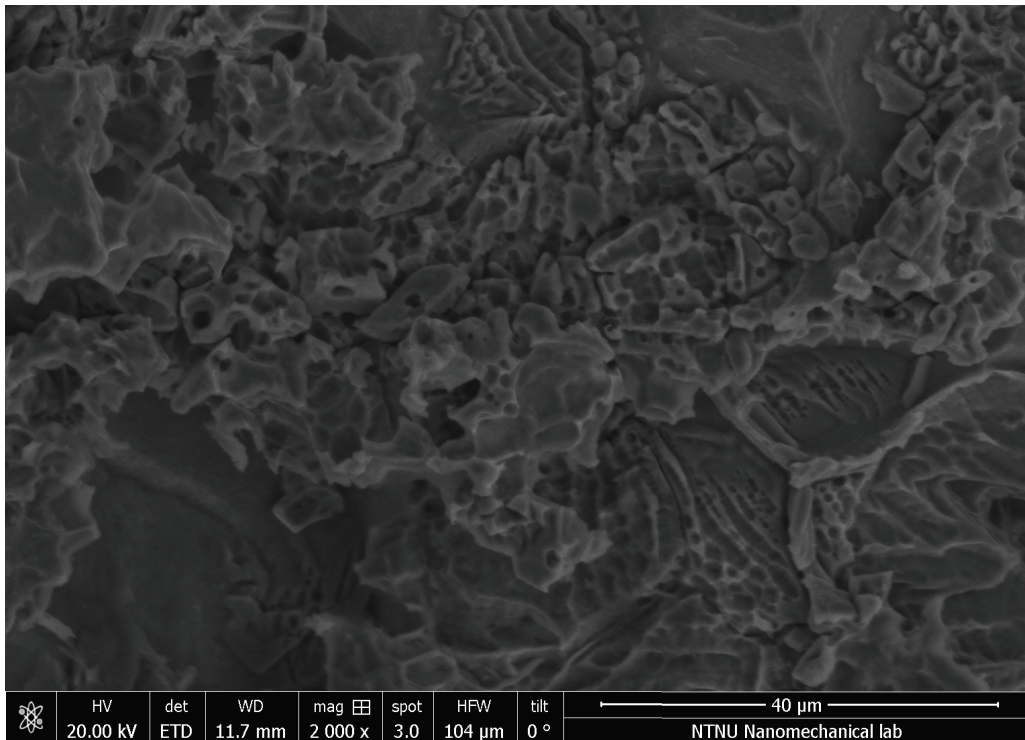
Figure 4.45: SEM image of the inside of Pit 2 of the TIG-welded, not pickled, not coated Sample A which was polarized to +400 mV vs. Ag/AgCl.
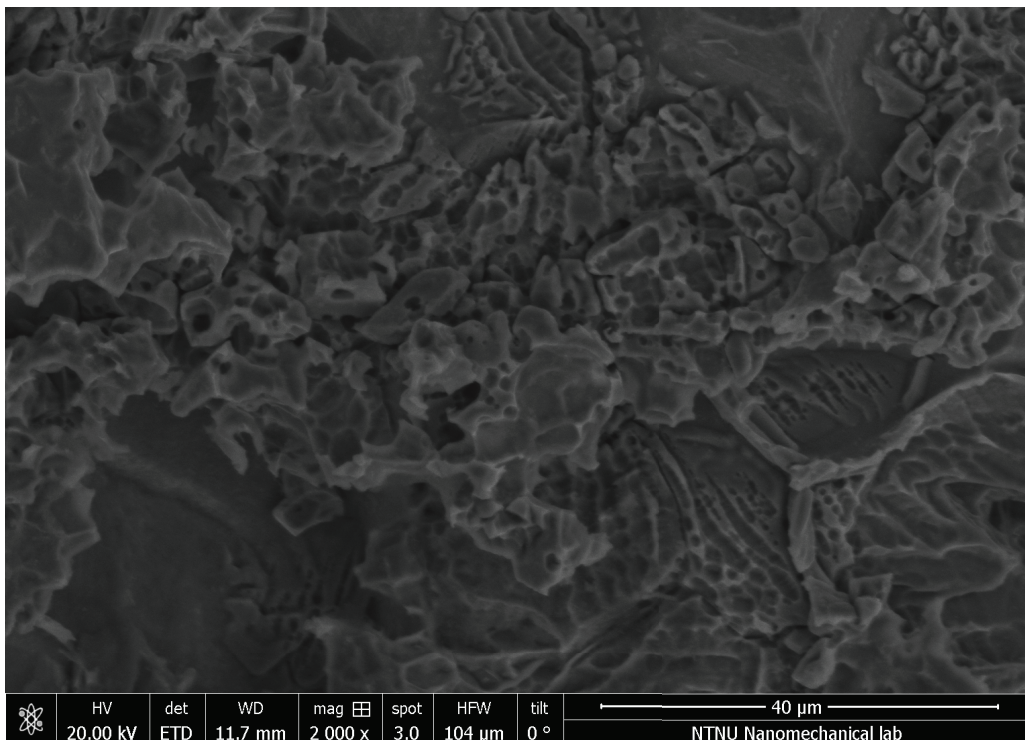
Figure 4.46: SEM image of the inside of Pit 3 of the TIG-welded, not pickled, not coated Sample A which was polarized to +400 mV vs. Ag/AgCl.

Pit 1 was analyzed in the SEM/EDS as seen in Figure 4.47.
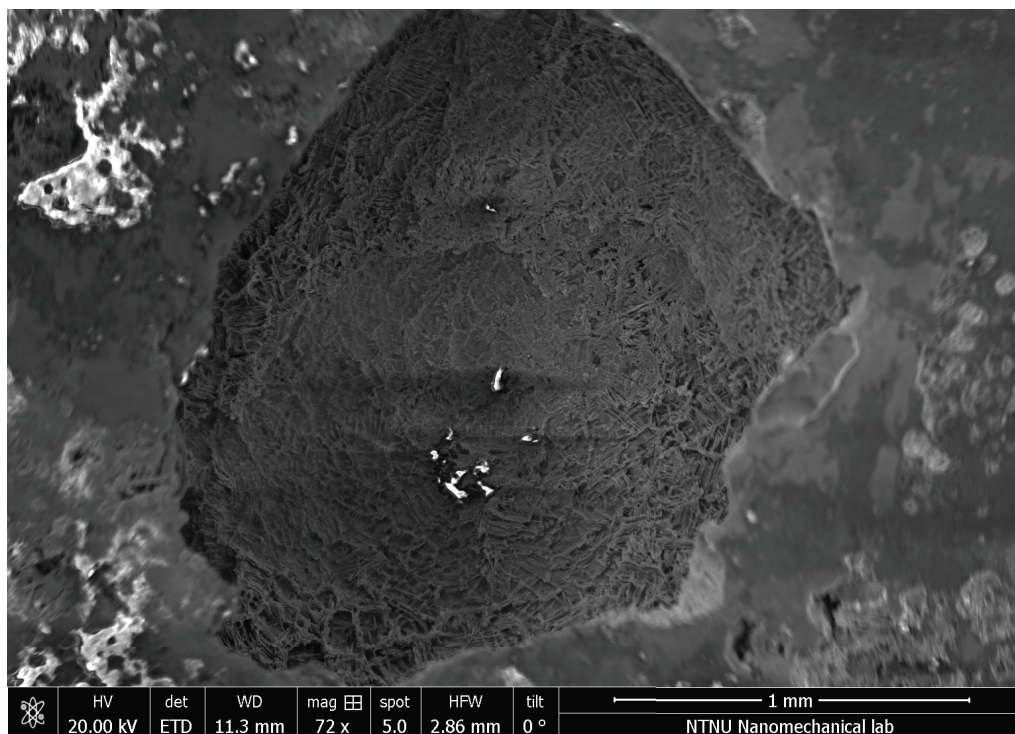
(a) SEM image displaying area analyzed.
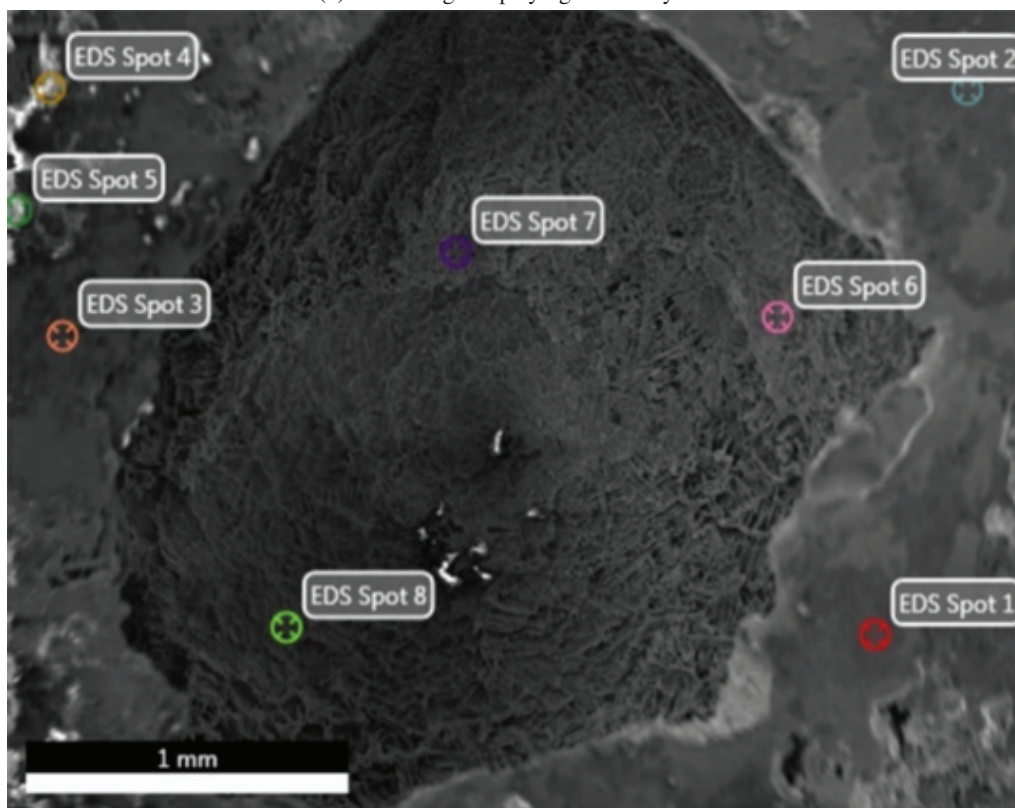
(b) EDS image displaying spots selected for analysis.

Figure 4.47: Pit 1 of the TIG-welded, not pickled, not coated Sample A polarized to +400 mV vs. Ag/AgCl analyzed by SEM/EDS.

Spot 1-3, seen in Figure 4.47, correspond to points outside of the pit, while Spot 4 and 5 correspond to white (non-conductive) bits, and Spot 6-8 correspond to the area inside Pit 1. Table 4.6 shows Spot 4 and 5 have high amounts of Na and Mg so these spots will not be discuss further as they most likely are spots of accumulated salts. This table also shows that the inside of the pit (Spot 6-8) have the highest PRE_N^* while the lowest PRE_N^* were found outside of the pit. The highest amounts of O are found outside of the pit.

Table 4.6: Composition of each element, expressed as weight percentage, found through EDS analysis for each spot in the area shown in Figure 4.47b, together with the calculated PRE_N^* for Pit 1 of the TIG-welded, not pickled, not coated Sample A polarized to +400 mV vs. Ag/AgCl.

Spot number	Composition [wt%]														PRE_N^*
	C	O	Na	Mg	Al	Br	Si	Mo	Cl	Ca	Cr	Mn	Fe	Ni	
1	7.31	16.38	-	1.01	-	-	0.43	3.80	-	0.43	23.89	-	41.67	5.07	36.43
2	5.63	14.96	2.79	-	-	-	0.23	2.61	2.49	-	23.72	-	42.19	5.36	32.33
3	15.54	10.60	-	1.18	-	-	0.50	2.59	-	1.01	23.79	1.70	38.82	4.27	32.34
4	12.82	10.48	24.68	0.69	-	1.71	0.19	7.98	33.58	6.24	0.87	-	0.77	-	27.20
5	11.08	19.28	19.46	1.19	13.79	-	0.71	8.30	16.49	8.36	1.34	-	-	-	28.73
6	15.47	9.49	-	-	-	-	1.65	3.35	-	-	27.81	-	38.91	3.32	38.87
7	14.25	9.61	-	-	-	-	1.29	3.03	-	-	30.02	-	39.15	2.64	40.02
8	5.74	3.08	-	-	-	-	0.95	2.79	-	-	32.13	-	51.41	3.91	41.34

Pit 2 was also analyzed through SEM/EDS to compare it to Pit 1. The SEM/EDS analysis was carried out as shown in Figure 4.48. Spot 1-6 in Figure 4.48 correspond to points outside of the pit, while Spot 7-14 correspond to points in the mouth of the pit, and Spot 15-20 correspond to the area inside Pit 2. Table 4.7 shows that Spot 6 has an unusually large amount of Mo as well as a diverse amount of, most likely, salts present. In addition, similar to the case of Pit 1, the highest PRE_N^* attained correspond to the areas inside the pit and the pit mouth (Spot 7-20).

Table 4.7: Composition of each element, expressed as weight percentage, found through EDS analysis for each spot in the area shown in Figure 4.48b, together with the calculated PRE_N^* for Pit 2 of the TIG-welded, not pickled, not coated Sample A polarized to +400 mV vs. Ag/AgCl.

Spot number	Composition [wt%]													PRE_N^*
	C	O	Na	Mg	Si	Mo	Cl	K	Ca	Cr	Mn	Fe	Ni	
1	6.75	8.46	-	0.46	0.47	2.83	-	-	-	24.33	-	50.04	6.66	33.67
2	4.41	7.34	-	-	0.32	2.49	-	-	-	25.47	-	52.64	7.33	33.69
3	6.21	12.73	-	0.46	0.30	3.18	-	-	-	24.67	-	46.60	5.85	35.16
4	12.55	12.15	1.82	1.68	0.89	3.54	-	-	-	24.41	3.05	36.63	3.27	36.09
5	3.51	10.55	-	1.68	0.77	4.09	-	-	-	26.92	3.48	44.63	4.38	40.42
6	14.80	19.54	2.83	1.94	1.33	10.22	1.55	0.42	0.57	24.33	3.75	17.67	1.06	58.06
7	9.14	10.07	-	-	1.72	3.69	-	-	-	31.84	-	40.84	2.70	44.02
8	13.56	11.67	-	-	1.32	2.92	-	-	-	30.10	-	36.44	3.99	39.74
9	8.51	8.62	3.95	1.41	0.90	3.01	-	-	-	27.83	-	41.92	3.85	37.76
10	3.20	10.14	-	1.17	0.51	4.51	-	-	-	28.79	-	47.21	4.46	43.67
11	6.08	3.80	2.50	-	0.37	3.21	-	-	0.36	25.54	-	52.33	5.81	36.13
12	18.00	14.71	-	-	0.59	1.50	-	-	-	35.43	-	26.76	3.01	40.38
13	9.82	9.94	7.15	2.14	0.59	3.53	2.57	-	-	19.24	-	40.60	4.41	30.89
14	1.57	-	4.96	-	0.38	2.92	1.70	-	-	29.36	-	54.41	4.70	39.00
15	11.35	11.10	6.17	-	1.03	2.73	-	-	-	30.96	-	34.52	2.13	39.97
16	17.92	30.25	-	-	0.24	2.47	-	-	-	23.09	-	24.59	1.45	31.24
17	13.12	16.20	-	-	0.66	3.47	-	-	-	30.09	-	33.81	2.65	41.54
18	15.48	19.98	-	-	0.11	0.85	-	-	-	30.38	-	32.79	0.41	33.19
19	18.30	-	-	-	2.35	2.51	-	-	-	35.05	-	38.38	3.42	43.33
20	7.07	-	6.16	-	1.64	1.90	-	-	-	37.47	-	42.57	3.20	43.74
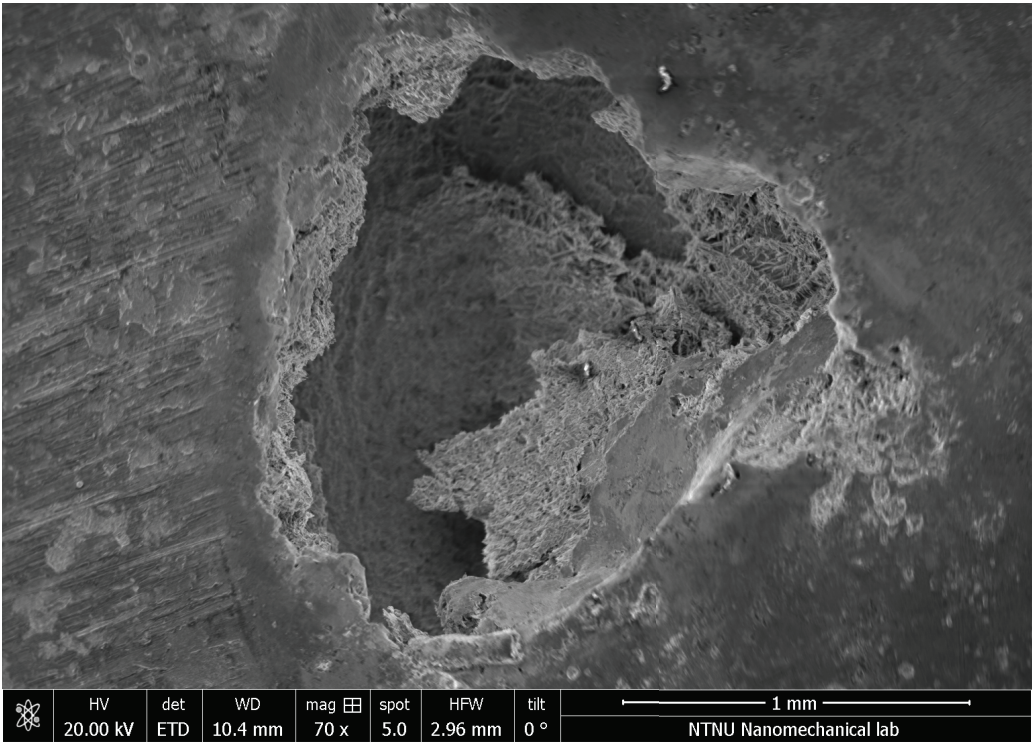
(a) SEM image displaying area analyzed.
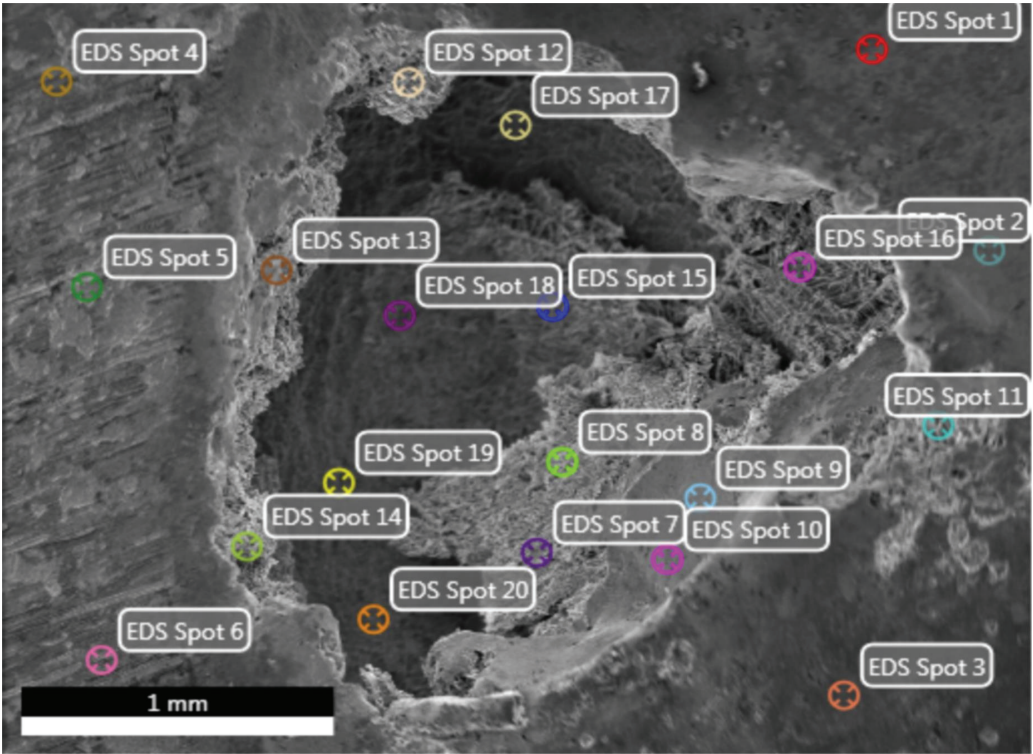
(b) EDS image displaying spots selected for analysis.

Figure 4.48: Pit 2 of the TIG-welded, not pickled, not coated Sample A polarized to +400 mV vs. Ag/AgCl analyzed by SEM/EDS.

The TIG-welded, not pickled, not coated Sample A was cut through Pit 1 perpendicularly to the weld to examine its cross-section with SEM/EDS as indicated in Figure 4.49.
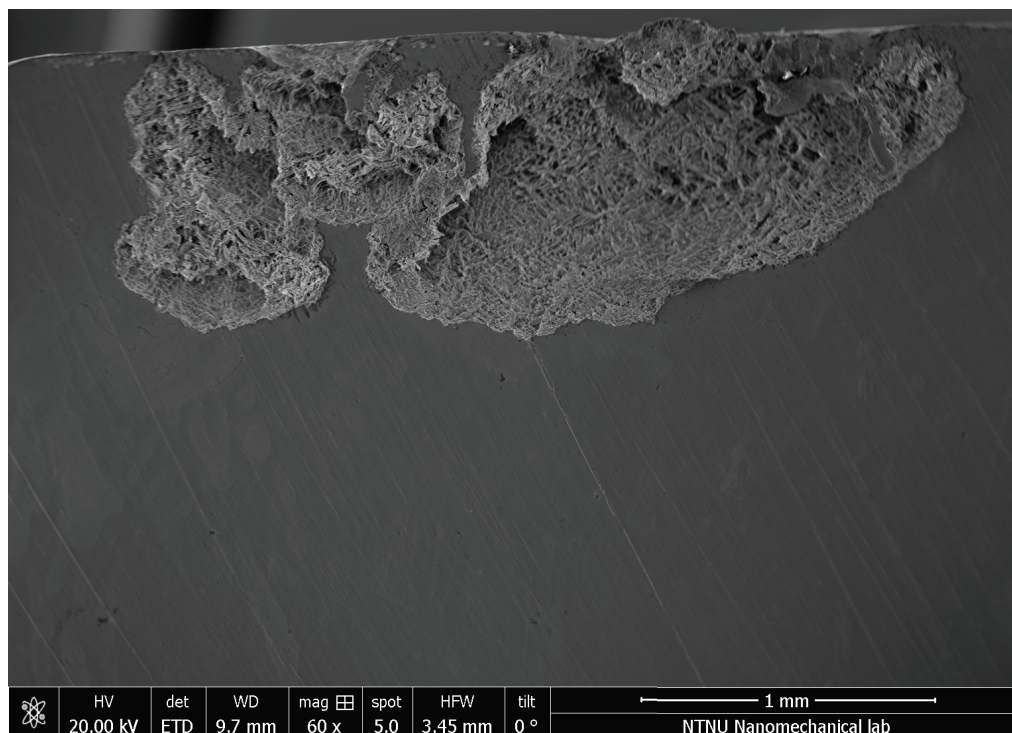
(a) SEM image displaying area analyzed.
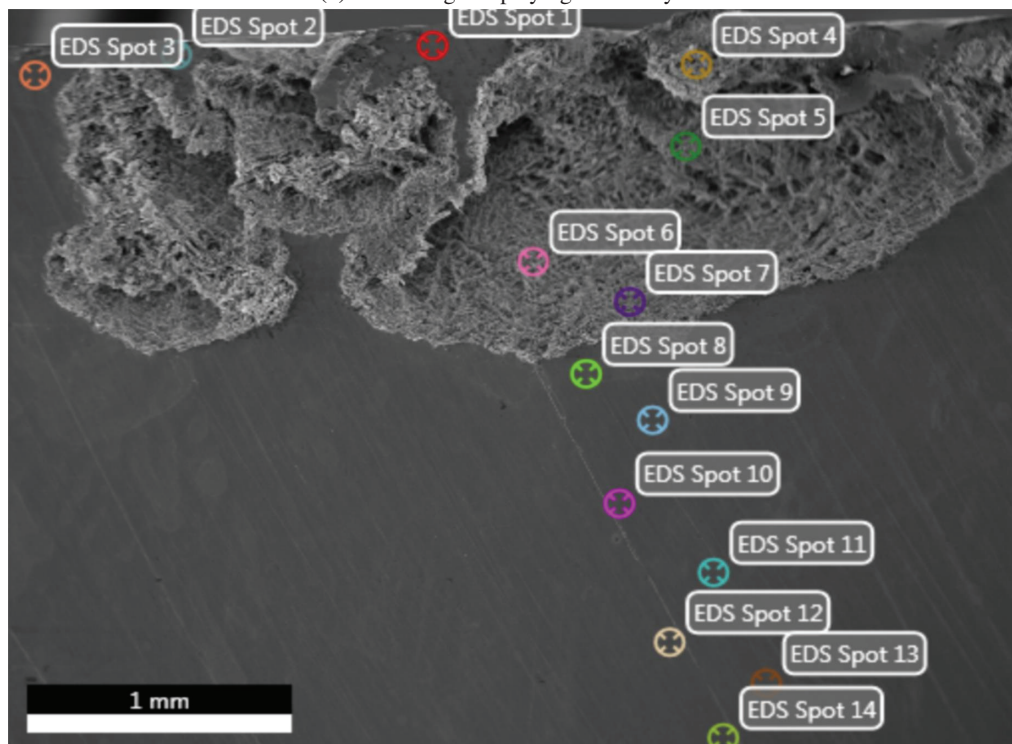
(b) EDS image displaying spots selected for analysis.

Figure 4.49: Cross-section of Pit 1 of the TIG-welded, not pickled, not coated Sample A polarized to +400 mV vs. Ag/AgCl analyzed by SEM/EDS.

Spot 1-3 in Figure 4.49 correspond to areas that are seemingly unaffected but that are close to the surface and the pit, Spot 4-7 are inside the pit, and Spot 8-14 are part of the unaffected material below the pit. The highest PRE_N* are found inside the pit while the PRE_N* of the other spots are relatively close. Fe and Ni are found in lower amounts inside the pit.

Table 4.8: Composition of each element, expressed as weight percentage, found through EDS analysis for each spot in the area shown in Figure 4.49b, together with the calculated PRE_N* for the cross-section of Pit 1 of the TIG-welded, not pickled, not coated Sample A polarized to +400 mV vs. Ag/AgCl.

Spot number	Composition [wt%]									PRE_N*
	C	O	Br	Si	Mo	Cr	Mn	Fe	Ni	
1	2.35	1.11	-	0.42	2.95	26.13	0.68	58.69	7.68	35.87
2	2.57	1.31	-	0.43	3.01	26.17	0.84	58.32	7.34	36.10
3	2.31	1.11	-	0.44	2.98	26.00	0.85	58.87	7.44	35.83
4	3.97	2.02	0.95	0.49	3.41	28.89	1.32	54.47	4.48	40.14
5	3.39	2.61	0.41	0.36	3.21	27.61	1.00	55.83	5.58	38.20
6	4.41	2.15	0.68	0.45	2.23	28.65	1.89	54.24	5.30	36.01
7	4.89	2.18	-	0.84	3.94	27.35	0.77	54.45	5.57	40.35
8	1.58	0.88	-	0.33	2.61	25.95	1.10	59.39	8.15	34.56
9	1.48	1.10	-	0.32	2.89	26.80	0.86	59.08	7.48	36.34
10	1.51	0.99	-	0.36	3.01	26.44	0.88	59.57	7.24	36.37
11	2.76	1.10	-	0.48	3.16	26.27	0.97	57.66	7.60	36.70
12	1.70	0.99	-	0.42	2.88	26.53	1.01	59.05	7.42	36.03
13	1.79	0.98	-	0.47	3.20	26.65	0.99	58.40	7.52	37.21
14	1.67	1.01	-	0.34	2.89	26.40	0.91	59.15	7.63	35.94

The pit outside of the coating of the TIG-welded, not pickled, coated Sample A was also imaged by the SEM, seen in Figure 4.50, as well as the corroded area underneath the coating, seen in Figure 4.51, to assess the nature of the attacks.
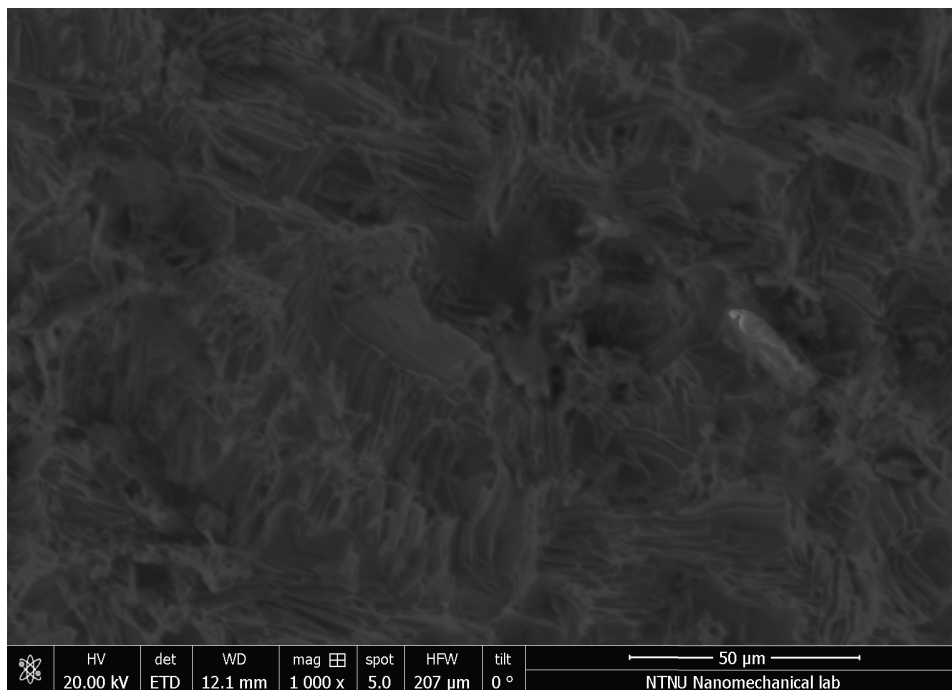
Figure 4.50: SEM image of the inside of the pit outside of the coating of the TIG-welded, not pickled, coated Sample A.
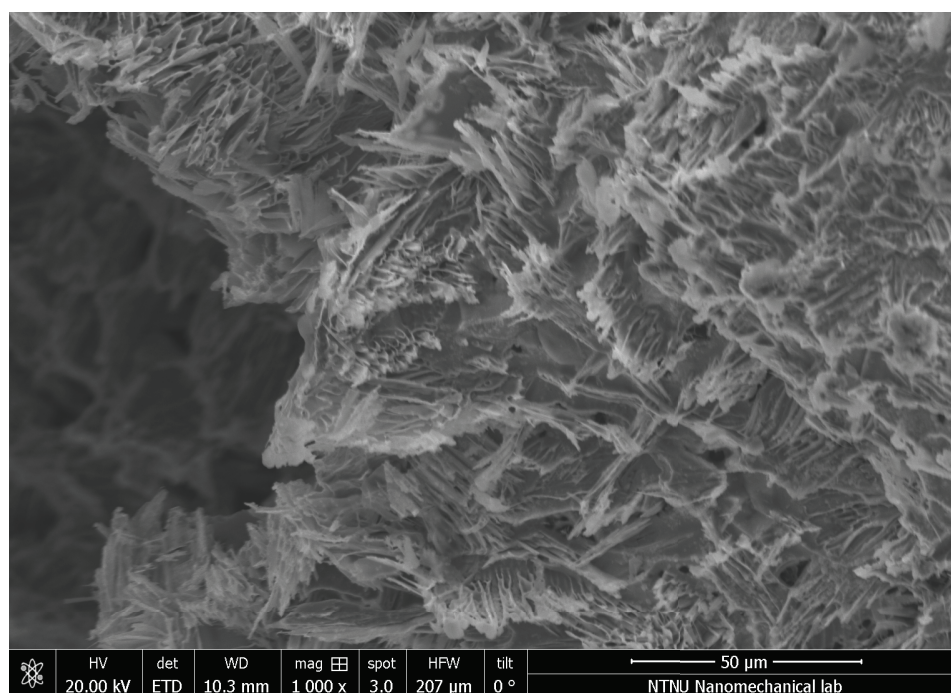
Figure 4.51: SEM image of the corroded area underneath of the coating of the TIG-welded, not pickled, coated Sample A TIG-welded, not pickled, not coated Sample A which was polarized to +400 mV vs. Ag/AgCl.

The pit outside of the coating of this sample was examined with SEM/EDS as shown in Figure 4.52. Spot 1-8 are located outside of the pit, while Spot 9-12 are located at the mouth of the pit, and Spot 13-15 are inside the pit. Table 4.9 shows that, unlike the other pits examined so far, the lowest PRE_N* are found inside the pit while the highest PRE_N* are outside, except for Spot 9 and 11 which have high PRE_N*. Nonetheless, the spots inside of the pit have larger amounts of Na and Mg.

Table 4.9: Composition of each element, expressed as weight percentage, found through EDS analysis for each spot in the area shown in Figure 4.52b, together with the calculated PRE_N* for the pit outside of the coating of the TIG-welded, not pickled, coated Sample A polarized to +400 mV vs. Ag/AgCl.

| Spot number | Composition [wt%] | | | | | | | | | | | | | | PRE_N* |
	C	O	Na	Mg	Br	Si	Mo	Cl	K	Ca	Cr	Mn	Fe	Ni	
1	-	-	-	-	-	0.42	3.30	-	-	-	24.97	-	62.92	8.39	35.86
2	2.57	17.10	-	0.71	0.58	0.17	3.27	0.72	-	-	24.69	-	46.14	4.04	35.48
3	1.66	1.57	-	-	-	0.10	2.61	-	-	-	24.27	1.02	60.04	8.74	32.88
4	2.81	11.84	1.75	1.21	-	0.46	4.39	1.36	-	-	24.18	1.38	45.13	5.48	38.67
5	4.79	8.88	2.67	2.31	-	0.82	5.01	1.87	-	0.27	22.47	-	45.64	5.28	39.00
6	1.76	1.58	1.28	0.36	-	0.41	2.61	-	-	-	23.28	-	60.87	7.84	31.89
7	2.20	1.40	-	0.38	-	0.40	3.07	-	-	-	23.57	-	60.42	8.57	33.70
8	3.52	9.80	2.39	1.12	0.53	1.48	3.11	1.02	-	-	24.70	1.19	44.96	6.17	34.96
9	4.33	2.33	3.95	0.78	-	1.02	0.53	-	-	-	42.13	7.54	37.38	-	43.88
10	7.06	17.24	12.51	1.81	0.87	6.76	3.16	6.62	-	-	15.13	-	26.87	1.97	25.56
11	6.78	8.81	12.36	1.09	0.55	4.40	2.13	-	-	-	33.52	-	28.56	1.80	40.55
12	10.20	9.08	10.02	1.41	0.72	4.40	3.58	5.18	0.14	-	18.38	-	34.29	2.61	30.19
13	9.90	13.28	16.16	2.03	-	6.87	2.91	-	-	-	19.59	-	26.19	3.07	29.19
14	6.48	12.10	13.88	0.98	-	6.73	2.13	-	-	-	26.47	-	29.96	1.28	33.50
15	13.23	13.98	14.44	2.25	-	5.20	2.06	-	-	-	21.95	-	24.98	1.91	28.75
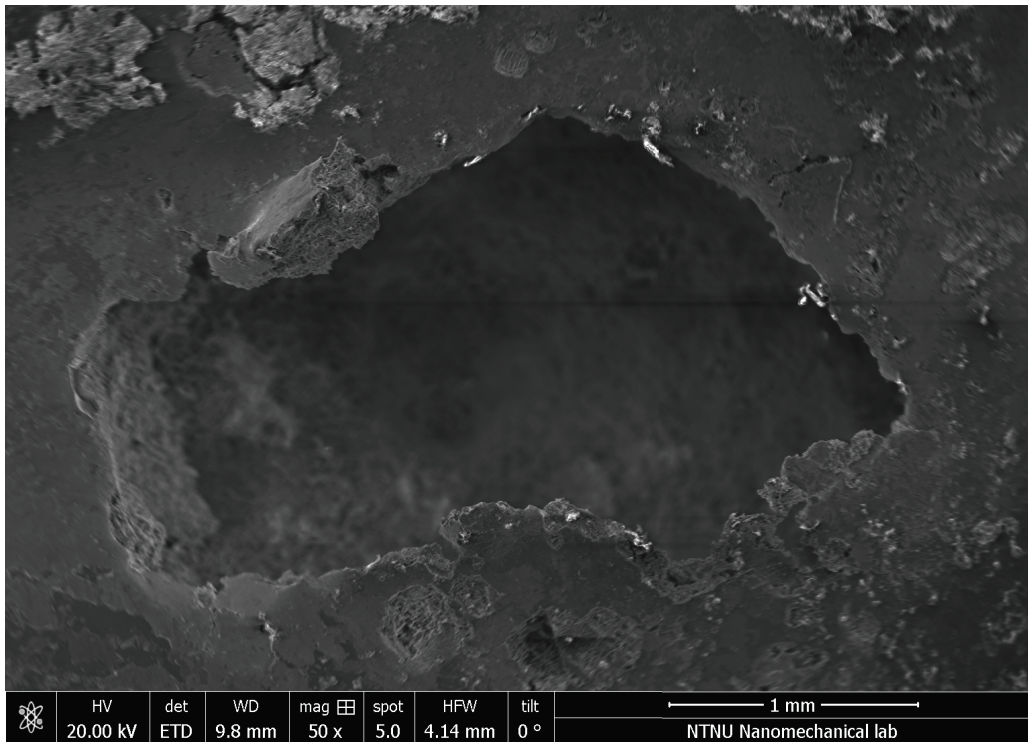
(a) SEM image displaying area analyzed.
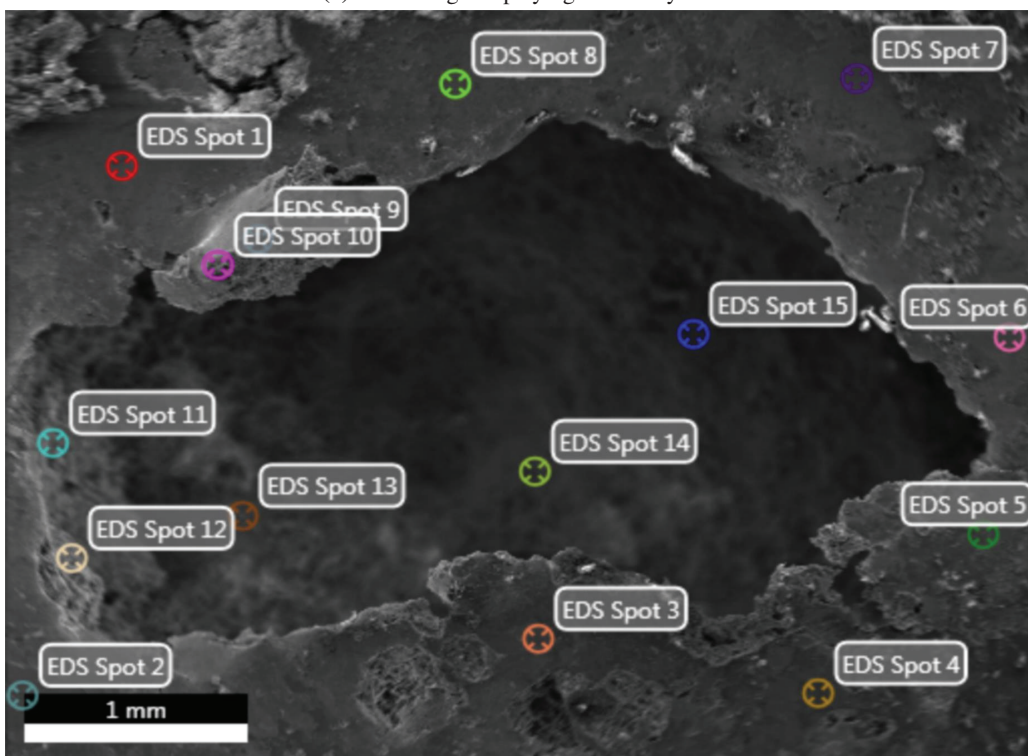
(b) EDS image displaying spots selected for analysis.

Figure 4.52: Pit outside of the coating of the TIG-welded, not pickled, coated Sample A polarized to +400 mV vs. Ag/AgCl analyzed by SEM/EDS.

The area underneath the coating was also analyzed through SEM/EDS as indicated in Figure 4.53.
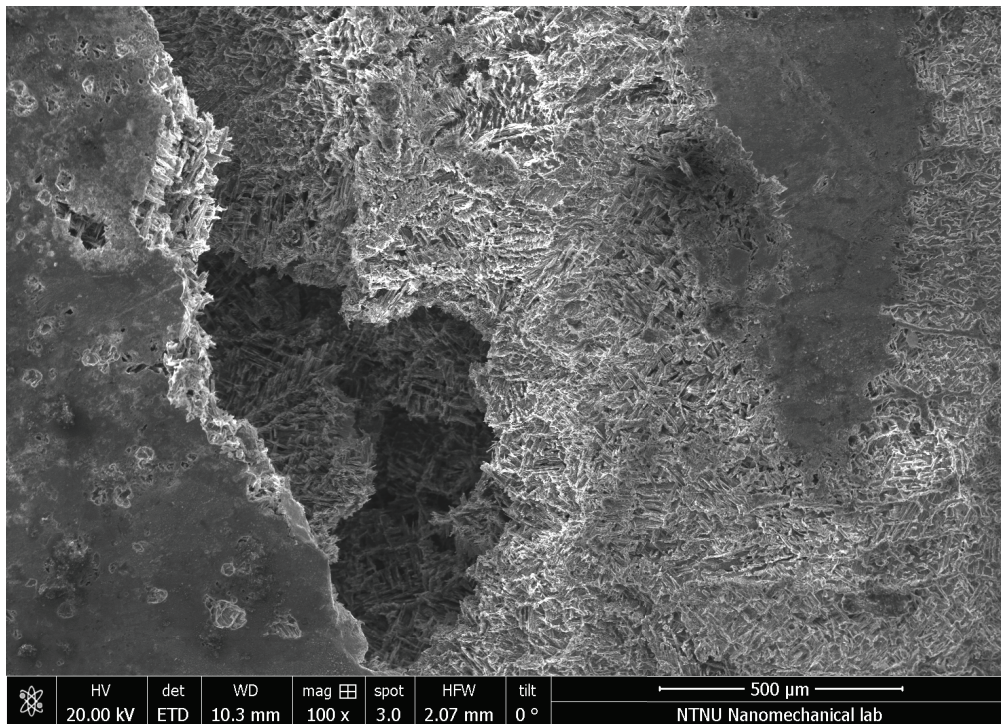
(a) SEM image displaying area analyzed.
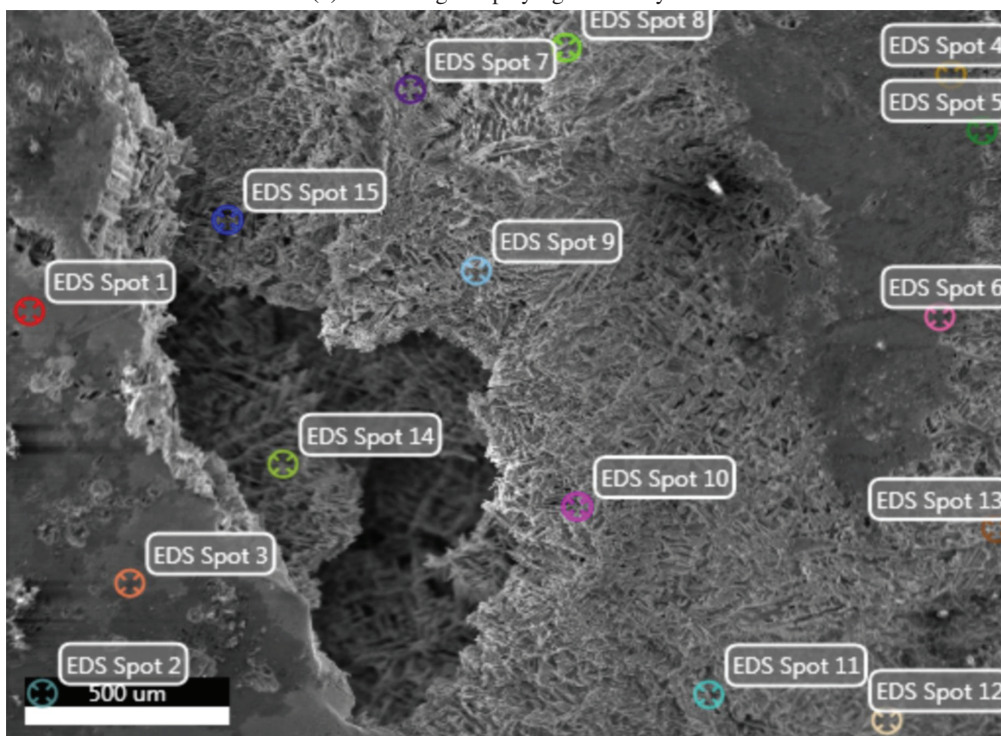
(b) EDS image displaying spots selected for analysis.

Figure 4.53: Crevice corrosion damage underneath the coating of the TIG-welded, not pickled, coated Sample A polarized to +400 mV vs. Ag/AgCl analyzed by SEM/EDS.

Spot 1-3 in Figure 4.53 are outside of the coated area, Spot 4-6 are in a seemingly intact area underneath the coating on the weld, Spot 7-13 are on the corroded area on the weld, and Spot 14 and 15 are on the deepest corroded area on the weld and closer to the coating edge. The PRE_N* is highest in Spot 14 and 15, and generally high in the corroded areas compared to the other areas. Additionally, the amount of O is the highest outside of the crevice.

Table 4.10: Composition of each element, expressed as weight percentage, found through EDS analysis for each spot in the area shown in Figure 4.53b, together with the calculated PRE_N* for the crevice corrosion damage underneath the coating of the TIG-welded, not pickled, coated Sample A polarized to +400 mV vs. Ag/AgCl.

Spot number	Composition [wt%]														PRE_N*
	C	O	Na	Mg	Br	Si	Mo	Cl	K	Ca	Cr	Mn	Fe	Ni	
1	2.43	1.56	-	-	-	0.47	3.20	-	-	-	24.32	-	59.71	8.31	34.88
2	4.99	10.61	1.46	0.91	3.27	0.38	2.37	-	-	-	25.35	-	45.16	5.51	33.17
3	5.03	11.56	-	1.03	2.23	0.31	2.20	-	-	-	24.12	1.16	47.22	5.12	31.38
4	1.53	2.33	3.16	1.33	-	0.46	2.69	2.12	-	0.18	21.83	-	55.75	8.60	30.71
5	2.04	3.90	6.81	6.70	-	0.51	2.76	8.74	0.28	0.49	17.52	-	43.80	6.45	26.63
6	3.12	3.81	-	1.05	-	0.55	4.88	-	-	1.51	21.92	-	55.07	8.10	38.02
7	4.67	2.74	3.39	-	-	0.83	4.43	1.04	-	-	27.58	-	51.36	3.96	42.20
8	1.01	1.64	9.00	0.40	-	0.03	1.92	2.67	-	0.12	25.61	1.28	50.94	5.38	31.95
9	0.59	0.52	3.16	-	-	-	0.89	1.58	-	-	36.83	5.57	47.55	3.30	39.77
10	4.82	5.03	14.45	1.32	-	1.12	2.87	5.26	-	-	24.86	-	35.03	5.25	34.33
11	1.96	2.04	8.69	0.54	-	0.18	0.86	3.48	-	-	39.07	-	40.10	3.08	41.91
12	1.07	3.22	9.31	1.20	-	1.45	3.29	3.95	-	0.84	21.95	1.46	46.67	5.58	32.81
13	1.32	1.50	6.46	0.85	-	0.20	-	4.25	-	0.94	25.07	2.15	50.13	5.99	25.07
14	1.95	2.57	5.65	-	-	0.65	1.15	2.09	-	-	45.48	-	37.35	3.11	49.28
15	1.99	3.28	5.96	-	-	0.95	1.19	1.95	-	-	41.85	-	40.22	2.62	45.78

As previously mentioned, TIG-welded, not pickled, coated Sample A which was polarized to +400 mV vs. Ag/AgCl was cut perpendicularly to the weld and along the crevice, and examined by SEM/EDS as shown in Figure 4.54. Spot 1-8 are located inside the crevice corrosion damage, with Spot 7 and 8 being at the deepest point away from the weld surface, and Spots 9-16 are part of the unaffected material below the pit. The highest PRE_N* were found at the bottom of the crevice (Spot 7 and 8), followed by the PRE_N* values of the material under the crevice, which are generally higher than those in the crevice (Spot 1-6).

Table 4.11: Composition of each element, expressed as weight percentage, found through EDS analysis for each spot in the area shown in Figure 4.54b, together with the calculated PRE_N* for the cross-section of the crevice corrosion damage underneath the coating of the TIG-welded, not pickled, coated Sample A polarized to +400 mV vs. Ag/AgCl.

| Spot number	Composition [wt%]													PRE_N*
	C	O	Na	Mg	Br	Si	Mo	Cl	Ca	Cr	Mn	Fe	Ni	
1	4.19	10.07	1.81	1.12	2.16	0.55	2.79	-	0.28	24.19	0.60	46.46	5.79	33.40
2	2.09	0.90	-	-	-	0.43	2.99	-	-	26.24	0.86	59.01	7.47	36.11
3	3.76	1.41	-	-	-	0.44	3.15	-	-	24.65	0.55	57.68	8.36	35.05
4	2.64	1.89	1.55	-	-	0.33	2.04	-	-	26.95	1.57	55.87	7.17	33.68
5	5.92	1.45	1.35	-	-	0.14	1.61	-	-	27.64	1.96	53.91	6.03	32.95
6	4.81	2.14	1.79	-	2.53	0.27	1.11	1.41	-	30.87	2.58	49.37	3.12	34.53
7	3.95	2.31	-	-	0.90	0.80	3.95	-	-	26.75	0.56	54.61	6.17	39.79
8	2.61	1.59	-	-	-	0.26	2.58	-	-	28.64	1.44	56.81	6.08	37.15
9	1.67	0.99	-	-	-	0.30	2.75	-	-	26.42	1.08	58.94	7.84	35.50
10	1.85	0.96	-	-	-	0.43	3.02	-	-	26.19	1.13	58.15	8.27	36.16
11	2.56	1.11	-	-	-	0.39	2.81	-	-	25.89	1.25	58.42	7.59	35.16
12	1.67	0.97	-	-	-	0.44	2.89	-	-	26.20	0.93	59.12	7.78	35.74
13	1.65	0.98	-	-	-	0.40	2.85	-	-	26.30	1.12	59.41	7.28	35.71
14	1.94	0.98	-	-	-	0.41	2.89	-	-	26.24	0.97	59.30	7.27	35.78
15	1.75	1.01	-	-	-	0.37	2.80	-	-	26.40	1.03	59.70	6.94	35.64
16	6.20	1.19	-	-	-	0.37	2.83	-	-	25.33	0.58	56.72	6.77	34.67
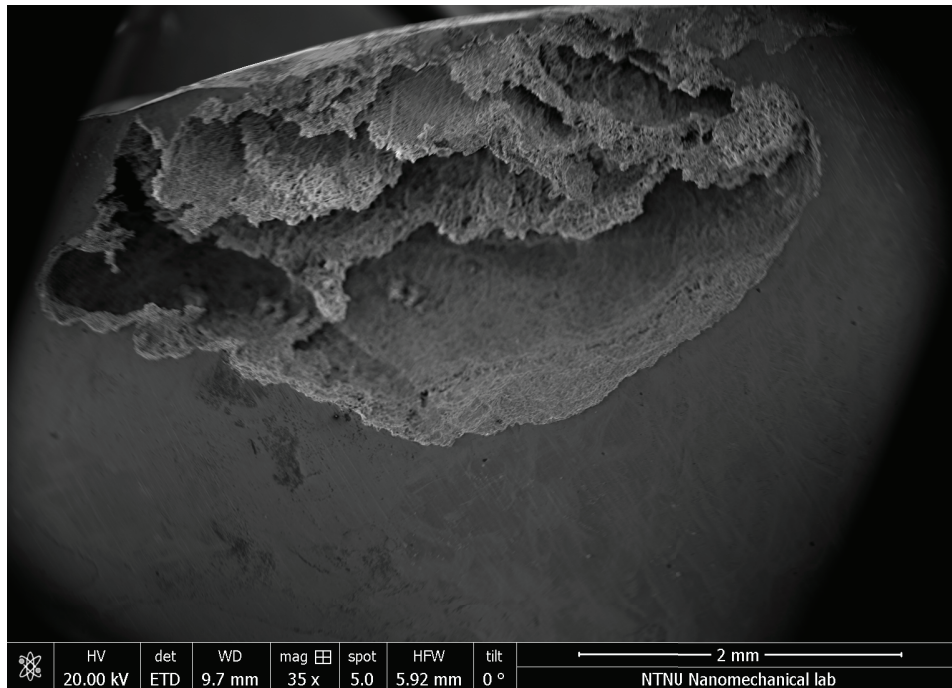
(a) SEM image displaying area analyzed.
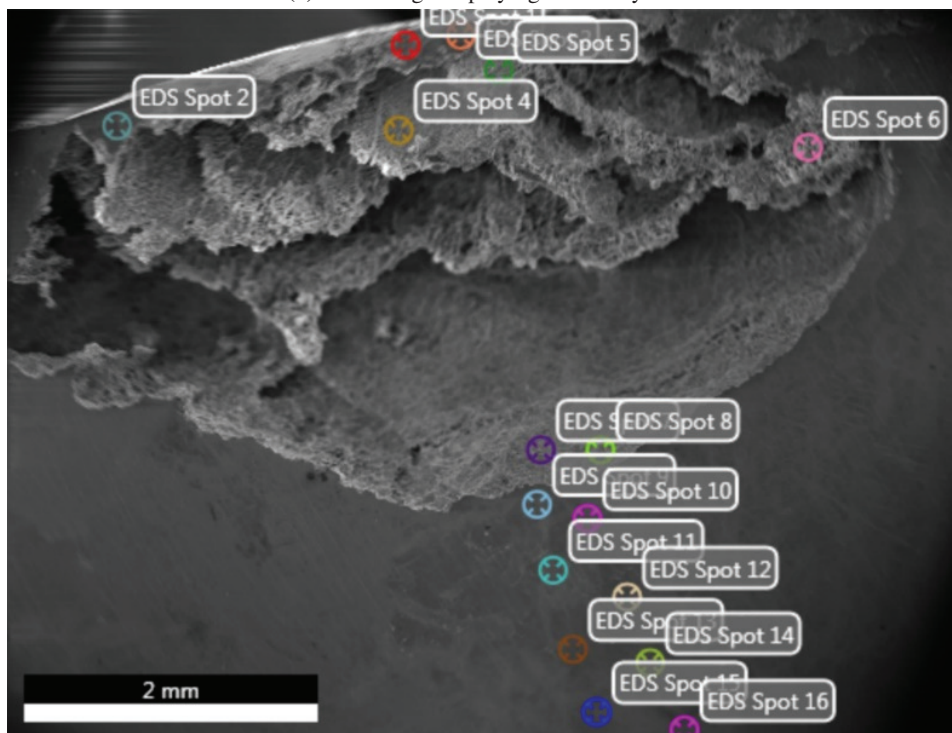
(b) EDS image displaying spots selected for analysis.

Figure 4.54: Cross-section of the crevice corrosion damage underneath the coating of the TIG-welded, not pickled, coated Sample A polarized to +400 mV vs. Ag/AgCl analyzed by SEM/EDS.

BSE

The BSE analysis of the untested TIG-welded pickled sample cross-section showed that intermetallic phases such as σ or χ were not present in any of the areas of the sample. Figure 4.55 shows that the only phases detected are austenite and ferrite. Figure 4.55c shows the interface between the HAZ (left) and the weld (right) at a lower magnification. Figure 4.55d and 4.55e were taken in areas at the edge of the etched area where the etching was the most efficient. The latter images are presented in order to show the microstructure of the weld and base material.
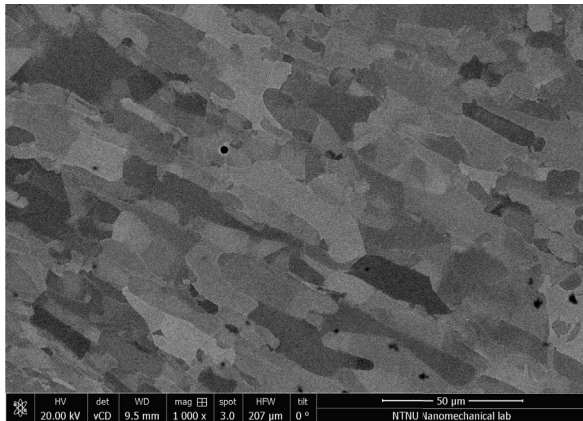
(a) HAZ.
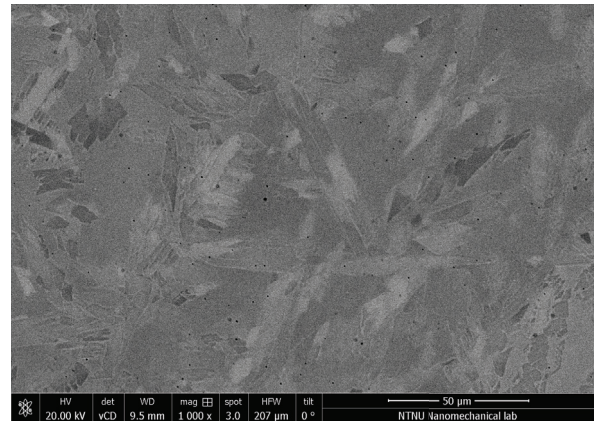
(b) Weld.
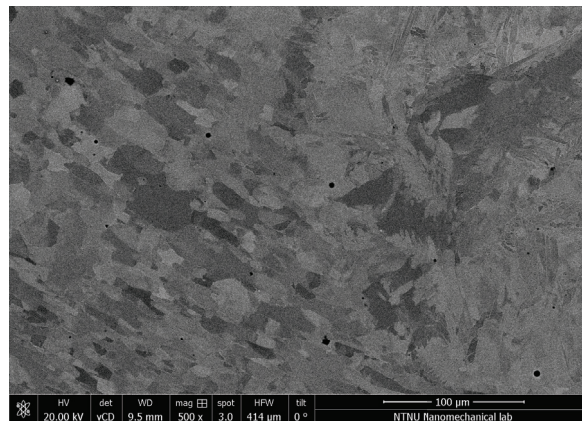
(c) HAZ-weld interface.
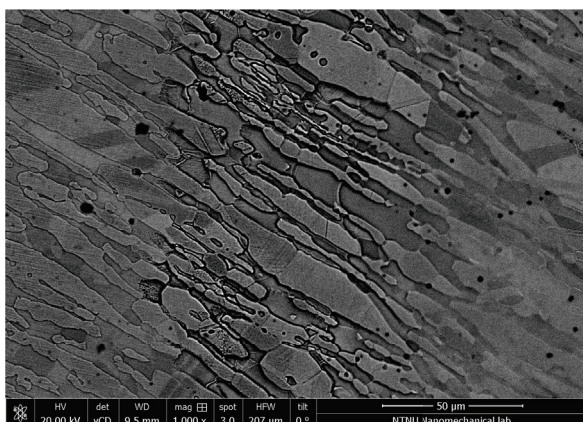
(d) Base.
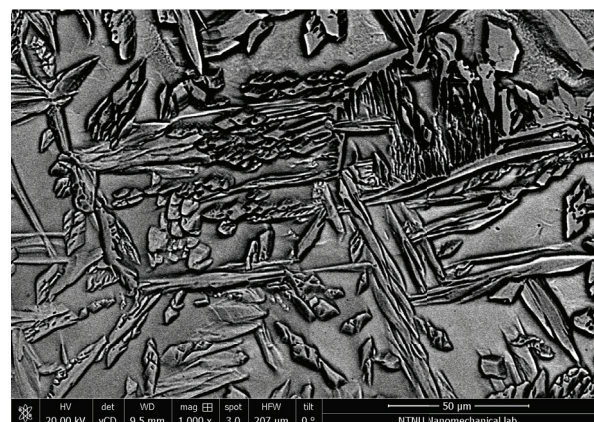
(e) Weld.

Figure 4.55: BSE imaging of phases present in the cross-section of a TIG-welded pickled sample.

EBSD

All phase and grain size diagrams obtained by EBDS are displayed in Figure 4.56. Figure 4.56a shows a content of 59.8 % austenite and 40.2 % ferrite the base material. The elongation of the grains in one direction due to rolling is quite noticeable in this image as well. In the HAZ, shown in Figure 4.56b, the proportion of austenite grains is less than in the base, as the austenite content is 50.3 % and ferrite 49.7 %. The grains, however, still show an elongated morphology similar to that in the base material. In the weld, shown in Figure 4.56c, the austenite content is 55.3 % and ferrite is 44.6 %. In this area, the austenite grains vary significantly in size and shape among each other, reassembling the microstructure of a cast material.

Figure 4.56d-4.56i show the grain size distribution in the different areas of the sample. The base material has the lowest maximum grain size, followed by the HAZ, which is then followed by the weld which has the highest maximum grain size.

(a) Phase map of base material.

(b) Phase map of HAZ.

(c) Phase map of weld.

(d) Austenite grain size distribution map in base material.

(e) Austenite grain size distribution map in HAZ.

(f) Austenite grain size distribution map in weld.

(g) Ferrite grain size distribution map in base material.

(h) Ferrite grain size distribution map in HAZ.

(i) Ferrite grain size distribution map in weld.
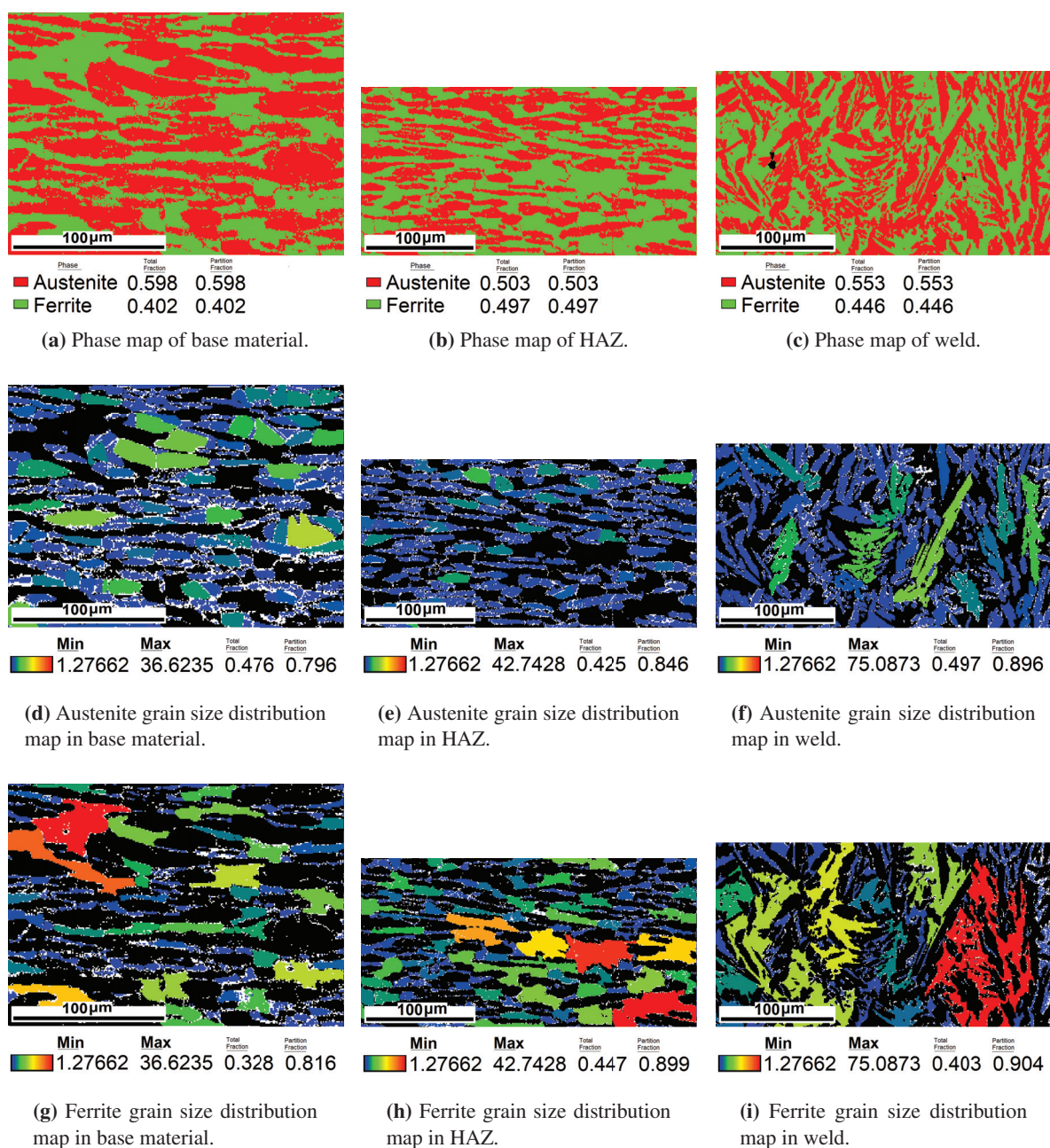
Figure 4.56: Phase and grain size maps for the different phases in the cross-section of a TIG-welded pickled sample at 200X magnification analyzed by EBSD.

XPS

Figure 4.57 compares the relative atomic percentages of Cr and its oxides and hydroxide at the surface (found when the sputtering time is approximately zero) of the three different regions, viz., the base material, HAZ and weld metal. This figure illustrates how the amount of Cr is generally higher in the pickled material than in the not pickled one, as well as higher at the weld than in the other two regions. Cr_2O_3 is found in larger proportions in the not pickled areas, with the base material having the largest amount of Cr_2O_3 than the other regions. It can also be seen that the proportions of $Cr(OH)_3$ are fairly close among the pickled areas, with the weld having slightly higher amounts than both of the other regions; however, in the not pickled samples, the variation is bigger with the weld having the highest amount of $Cr(OH)_3$ and the base material having the lowest. As for CrO_3, the HAZ of both the pickled and the not pickled samples have higher amounts than the other regions. Generally, $Cr(OH)_3$ and Cr_2O_3 are found more predominantly at the surface of all samples than Cr and CrO_3.
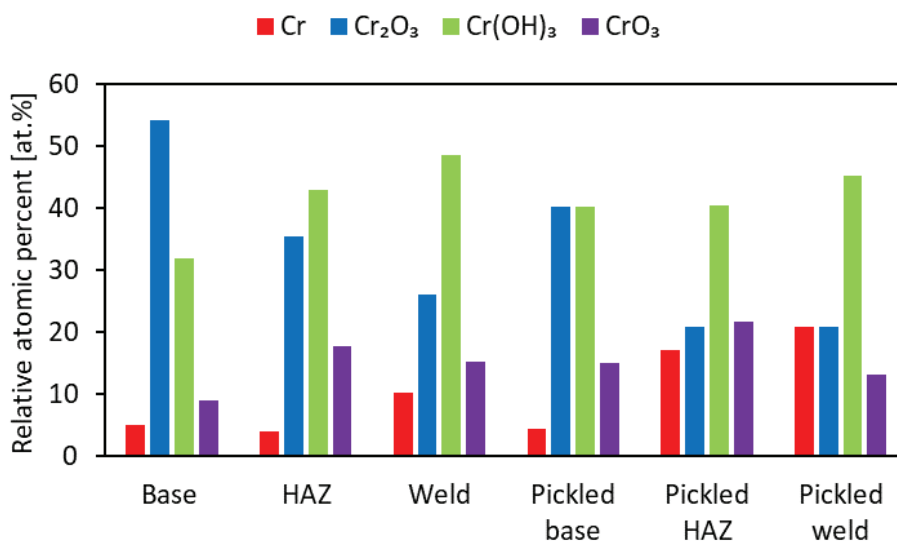
Figure 4.57: Amount of Cr and its oxides and hydroxide, expressed as the relative atomic percent, found at the base material, HAZ and weld of TIG-welded pickled and not pickled sample surfaces.

Figure 4.58 shows the relative atomic percents of the different Cr and its oxides and hydroxide present in the surfaces of the different regions of the pickled and not pickled samples as a function of sputterring time. As sputtering time increases, the proportions of Cr and its oxides and hydroxide in the base material of the not pickled sample become similar to those of the pickled base, HAZ and weld, with Cr being more prevalent. The reference sputtering rate for the results shown in Figure 4.58 and 4.60 is approximately $0.003\ \mathrm{nm\,s^{-1}}$ with respect to a Ta/Ta_2O_5, given by Zavieh and Espallargas [95] from a similar investigation where the same equipment was used. Figure 4.58b indicates, that, contrary to the base material, Cr_2O_3 and $Cr(OH)_3$ are present in the not pickled HAZ in bigger proportions than Cr as sputtering time increases. In the not pickled weld, Cr_2O_3 is present in larger amounts followed relatively close by $Cr(OH)_3$, which is followed by Cr and later CrO_3.

(a) Base material.

(b) HAZ.

(c) Weld.

(d) Pickled base material.

(e) Pickled HAZ.
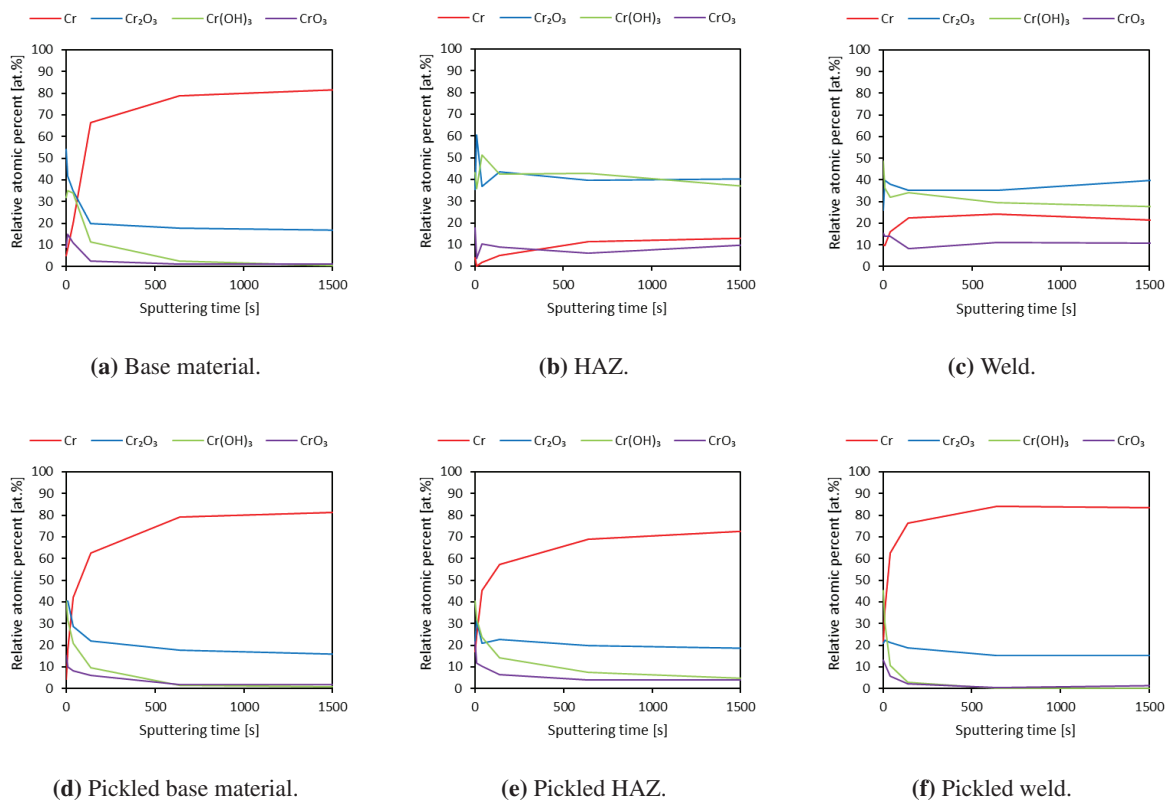
(f) Pickled weld.

Figure 4.58: Relative atomic percent as a function of sputtering time, expressed in seconds, of the different Cr and its oxides and hydroxide found in the base material, HAZ and weld of TIG-welded pickled and not pickled samples when sputtering the sample surfaces.

The Fe/Cr ratio at the surface of each sample (found when the sputtering time is approximately zero) is presented in Figure 4.59. It is evident from the chart that the ratio is significantly higher in the not pickled samples compared to the pickled samples. In addition, the ratio is higher at the weld and lowest at the base material for both the pickled and not pickled conditions.
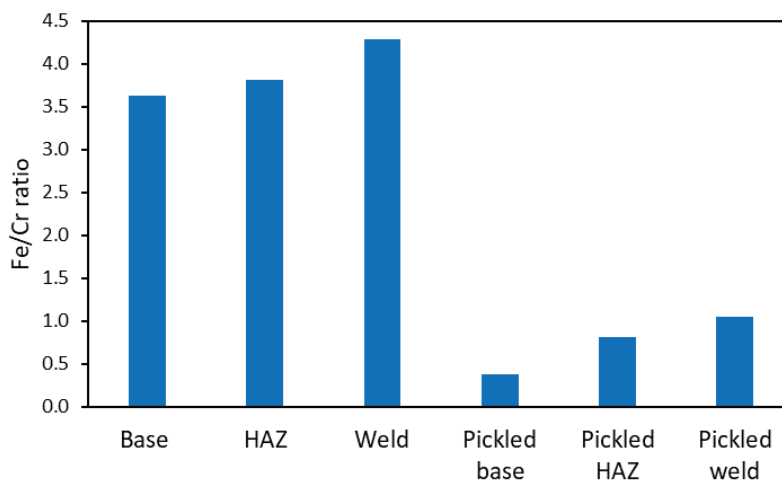
Figure 4.59: Fe/Cr ratio at the surface of the base material, HAZ and weld of TIG-welded pickled and not pickled samples.

Figure 4.60 presents the relative atomic percent of each element in each of the areas of the sample surfaces as a function of sputtering time. This data is also presented comparing the amounts of each element alone for each sample area in Appendix D.

(a) Base material. **(b)** HAZ. **(c)** Weld.
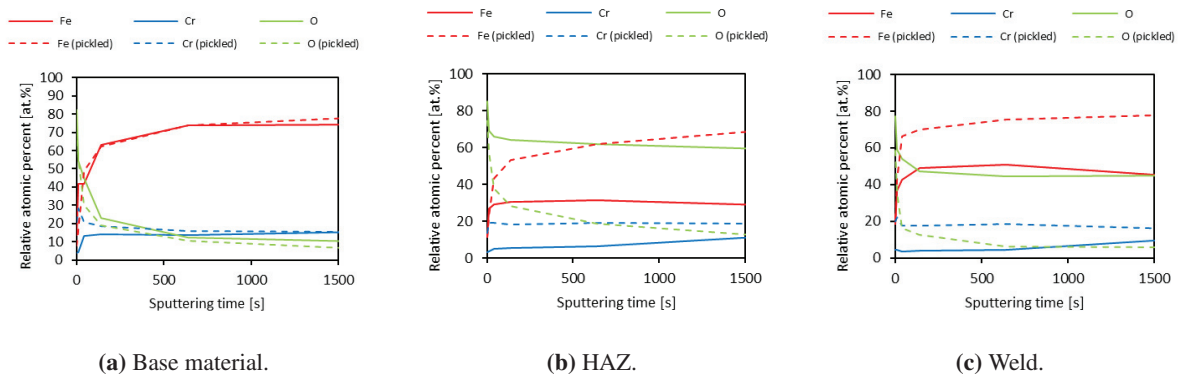
Figure 4.60: Relative atomic percent as a function of sputtering time, expressed in seconds, of Fe, Cr and O found in the base material, HAZ and weld of TIG-welded pickled and not pickled samples during depth profiling.

Hardness across the weld

Figure 4.61 shows the hardness of the material across a cross-section of the weld. The measurement points 8-15 correspond to the fusion zone and where the material is the hardest according to the test performed. These results will not be discussed in the following section.
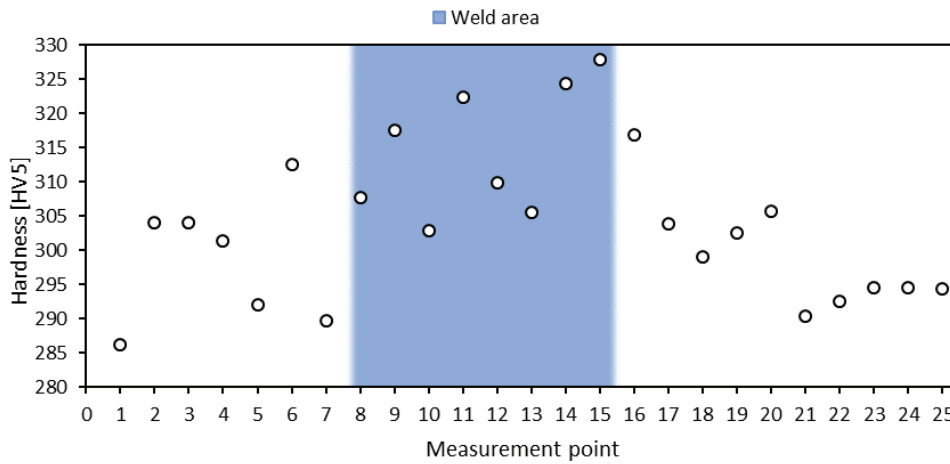
Figure 4.61: Vicker's hardness number, HV5, across a cross-section of the weld of a SDSS sample.

4.3 Discussion

Critical corrosion temperature

Two different welding procedures were included in the test program; i) laser welding without filler metal, and ii) TIG welding with filler metal. The laser welding was performed by a company that normally does not supply services to the oil and gas industry, but is instead more focused on the agriculture industry. In this industry austenitic stainless steel grades like AISI 304 and AISI 316 are the workhorses, while SDSS is seldom used. Because of this, the company has limited experiences with welding SDSS. The quality of the laser weld documents a lack of experiences; poor weld seam with local micro-crevices due to lack of burn through. Figure 4.1f shows an example of the weld seam. As a result of this, the laser weld is not representative of a qualified weld on SDSS. This is also the reason why the laser welds were not characterized and will not be discussed in further detail.

For the TIG welding procedure, pickling the TIG weld showed a significant improvement in T_{crit} except for when the samples were both polarized and coated where pickling did not produce a significant effect. The results indicate the positive effect of pickling does not outweigh the combined detrimental effect of polarization to +400 mV vs. Ag/AgCl and the introduction of crevices by a coating.For the TIG welding procedure, pickling the TIG weld showed a significant improvement in T_{crit} except for when the samples were both polarized and coated where pickling did not produce a significant effect. The results indicate the positive effect of pickling does not outweigh

Of all the samples exposed at OCP, only the not pickled, coated TIG-welded samples and the not pickled, coated laser-welded samples initiated corrosion. At +400 mV vs. Ag/AgCl, however, all welded samples initiated corrosion. None of the samples exposed at OCP reached an OCP value higher than +200 mV vs. Ag/AgCl, due to the absence of biofilm, which should, in theory, make them less susceptible to localized corrosion attacks than the samples that were polarized to +400 mV vs. Ag/AgCl. Nevertheless, the T_{crit} of the TIG-welded, not pickled, coated samples exposed at OCP is lower than their polarized counterparts. This was also the case for one of the laser-welded coated samples exposed at OCP which initiated at 36 °C compared to its polarized counterparts which initiated at 41 and 45 °C. This is most likely related to the differences in how T_{crit} were determined, i.e. potential drop for the OCP samples and increase in anodic current density to 100 µA cm^{-2} for polarized samples. The TIG-welded, pickled, coated samples, however, did show a significant decrease in T_{crit} of at most 44 °C in the polarized condition compared to the OCP condition.

The differences between bare and coated samples are very significant when it comes to the samples exposed at OCP. The difference in T_{crit} between bare and coated samples are, at least 44 °C and at most 48 °C for the TIG-welded, not pickled samples exposed at OCP, and 28 and 40 °C, respectively, for the laser-welded samples exposed at OCP (using the maximum temperatures achieved as references for both). On the other hand, the differences between coated and bare polarized samples, were at least 3 °C and at most 6 °C for the TIG-welded, not pickled samples, and 3 and 7 °C for the laser-welded samples. The polarized TIG-welded pickled samples, had a difference of at least 21 and at most 28 °C, between bare and coated samples; this difference is quite large indicating the pickled weld quality was largely affected by the introduction of crevices. Nevertheless, this decrease in T_{crit} is still smaller than the aforementioned change due to polarization seen in the TIG-welded, pickled condition, which was of 44 °C, implying biofilm is a bigger threat to the pickled welded material than a crevice formed by a poor coating such as the one used.

The effect of welding on T_{crit} can be appreciated comparing the T_{crit} of the TIG-welded, pickled, not coated polarized sample with the polarized base material samples. The difference in T_{crit} is at least 17 °C, not considering the fact that the base material samples started to show signs of corrosion products above 80 °C. Considering the not pickled TIG weld and the laser weld, the difference becomes much larger. Moreover, compared to the base material in 3.5 % NaCl solution investigated during the previous semester [7], the TIG-welded, not pickled, coated samples exposed at OCP did just as well as one of the artificial crevice specimens exposed at OCP. However, the coated base material samples exposed at OCP and polarized to +300 mV vs. Ag/AgCl, had higher critical temperatures than any of the coated welds in the present work. The coated base material exposed at OCP investigated previously did not corrode during the test that reached 61 °C, and the coated base material polarized to +300 mV vs. Ag/AgCl initiated at 65 and 77 °C vs. Ag/AgCl. While this comparison gives an idea of how welding decreases the T_{crit} of the the base material, accurate parallels are complicated to draw since the electrolytes used are different and the artificial crevice assembly used offers a different, and mostly narrower, crevice geometry than a coating.

Polarizing the pickled TIG-welded samples cathodically, for a week, at a potential of -1100 mV vs. Ag/AgCl was the factor that decreased the T_{crit} the most. Compared to the other samples polarized to +400 mV vs. Ag/AgCl, the difference in T_{crit} is 48 °C compared to the TIG-welded, pickled, not coated sample, and at most 27 °C compared to the TIG-welded, pickled, coated sample. The pre-cathodically polarized samples never reached a zero current density and were already showing signs of corrosion as the electrolyte was still at room temperature. The acuteness of the effect of cathodic polarization is also mirrored in the fact that corrosion attacks started in the HAZ as well as the weld metal, which did not happen to any of the other samples. The severity of the situation is also augmented considering these samples were pickled, which is the best welding quality investigated. Furthermore, there was no significant difference between the temperature and time of initiation between the coated and the bare sample, indicating pitting and crevice corrosion were just as likely to initiate in this temperature range. On the other hand, the supposed crevice corrosion damage, pictured in Figure 4.34b and 4.36, seems to have propagated away from the crevice contrary to all of the other crevice attacks; this might indicate the attack started as a pit that propagated towards the coating rather than being a crevice corrosion attack.

According to the results from the previous work mentioned in Section 3 [80], SS32750 [not welded] samples with artificial crevices and polarized to +600 mV vs. Ag/AgCl reached a T_{crit} of 41 and 46 °C, after being charged for a week at -0.1 mA cm^{-2} before being immersed in 3.5 % NaCl solution and increasing the temperature of the electrolyte. It was reported that this result amounted to a decrease in T_{crit} of approximately 22 °C when compared to the uncharged condition. For welded samples polarized to +600 mV vs. Ag/AgCl with an artificial crevice, hydrogen charging with a current density of -0.1 mA cm^{-2} for only 24 hours produced a decrease in T_{crit} equal to 12 °C. One aspect that could account for the more dramatic temperature change in the present work (27 and 48 °C) compared to the previous work (12 and 22 °C) could be the formation of uneven calcareous deposits on the samples in the present work which may have acted as crevices. It is worth noting the samples on the previous work were polarized to +600 mV vs. Ag/AgCl which should, in theory, make them more susceptible to localized corrosion. Moreover, the results from previous work on pre-cathodic polarization in natural seawater [89], also mentioned in Section 3, showed base material samples pre-cathodically polarized to -1100 mV vs. Ag/AgCl for 336 and 720 hours followed by critical corrosion temperature testing in natural seawater, while polarized anodically to +600 mV vs. Ag/AgCl, initiated corrosion at 25 °C which is similar to the samples in the present work. This indicates the effect of hydrogen adsorption due to cathodic polarization to -1100 mV vs. Ag/AgCl on T_{crit} is not sensitive to material quality (base or welded), polarization (+400 or +600 mV vs. Ag/AgCl), presence of crevices (bare, coated or with artificial crevices) and charging duration (168 vs. 336 and 720 hours).

In terms of repassivation, in the polarized condition, the TIG-welded samples, pickled and not pickled, performed better than the laser-welded samples. Except for the polarized TIG-welded pickled, coated, samples, there are no major differences in repassivation between the coated and not coated TIG-welded polarized samples. In the same way, the repassivation behavior of the TIG-welded not coated pickled and not pickled samples is very similar, which is explained by the fact pickling is purely a surface treatment and the crevice and pitting damages were mostly deep. As for the polarized TIG-welded pickled coated samples, although Sample A did not manage to repassivate like Sample B, it did show a significant decrease in anodic current density already as the temperature was decreased from 42 °C. Sample A's final anodic current density values (as shown in Figure 4.26) approached 10 µA cm^{-2}, therefore, its repassivation behavior is not significantly different from Sample B's. Nonetheless, the most important result from investigating repassivation is that, after initiation, a crevice or pitting corrosion attack may propagate at temperatures below 25 °C. It has been shown that propagation is able to take place in temperatures down to 15 °C in seawater environments for high-alloyed welded stainless steels [78]. Taking this into consideration, the 20 °C limit for SDSS in seawater stated by NORSOK M-001 and ISO 21457 seems more sensible for applications where one cannot guarantee a service temperature below 40 °C where weld material and crevices are present. However, the results from the base material suggest these standards should consider specifying limits according to material quality (base material, welded, etc.) given the significant differences in corrosion behavior, as Kivisäk implies [12] (see Section 3). Moreover, even if some samples did not manage to repassivate according to the limit used (10 µA cm^{-2}) during the test, the anodic current density was significantly reduced as the temperature was decreased in all cases except for the pre-cathodically polarized samples. Therefore, even if propagation is able to take place as the temperature is decreased, the corrosion rate may be negligible in some cases.

Although it was unfortunate that during testing of all polarized TIG-welded, coated samples, both pickled and not pickled, the temperature was not decreased until several hours after initiation, which meant the temperature kept increasing every 4 hours, these tests give an insight into the current density development beyond initiation and any influence in repassivation. Most notably are the pickled samples which presented two different behaviors; the

anodic current density of Sample B stayed below 485 µA cm^{-2} while Sample A was able to reach 1976 µA cm^{-2}. This not only highlights the randomness of the manifestation of the attacks but also how severe an attack can become.

While the IFM gave a satisfactory estimate of how deep the corrosion damage could be, it is possible the damages were more extensive that they appeared, such as it happened with the TIG-welded, not pickled coated samples. This may not have been the case for all attacks since the polarized TIG-welded not pickled, not coated sample was also cut for the SEM/EDS analysis and Pit 1 was the same depth as estimated by examining its surface with the IFM. Moreover, 36 hours and 10 minutes passed from initiation of this sample until repassivation so, if it is assumed the depth of Pit 5 is accurate, the corrosion rate of this pit was approximately 0.04 mm h^{-1} which is significant considering the temperature started to decrease not long after initiation and considering the anodic current density is not as high as it was for the coated samples.

All the attacks seem to have initiated in the weld metal, as brown rust was seen in these areas during initiation, indicating an increased susceptibility in this area. The exception to this were the samples that were previously polarized cathodically and the polarized TIG-welded, pickled, coated Sample A. The latter which initiated at a scratch on the surface of the material under the coating close to the HAZ. The scratch most likely aided corrosion initiation, causing the 7 °C difference with Sample B, and then the attack propagated into the weld (if it had not initiated already) while the scratched area most likely repassivated promptly. This indicates how, even if corrosion initiates elsewhere, the weld is the preferential corrosion site for the type of welded samples used.

The wire material used for the TIG-welding was S32760 whose welded condition, some research [81] points out, has a 5 °C lower critical temperature than welded S32750. However, given how the materials are so similar and preferential attacks on the weld were expected, the differences in SDSS grades are insignificant for this work.

While the temperature regulator caused some problems with the temperature increases, in most cases, such as during the testing of the laser-welded, not coated samples exposed at OCP, the cathodically polarized sample, and the base material; these problems are not significant to the results of the experiments. It is somewhat significant for the laser-welded, coated Sample A exposed at OCP as the temperature change was too abrupt right before initiation. Still, Sample B initiated much before so this glitch is negligible.

Many samples experienced an increase in anodic current density and showed signs of corrosion well before reaching 100 µA cm^{-2}. This limit is used as a reference dictated by the ASTM G150 standard, although if one were to take into account those small increases, like the ones seen in all polarized coated samples, the critical temperatures for these samples would be much lower. Furthermore, for the samples exposed at OCP, it was difficult to accurately determine what the actual T$_{crit}$ should be as some potentials decreased gradually over a span of many temperatures. In the case of the not pickled, coated, TIG-welded samples exposed at OCP, even though there was a gradual potential drop, brown rust was seen and the temperature kept increasing after corrosion initiation, the corrosion attacks were shallow. It is worth noting the OCP of both of the samples before corrosion initiation was low, around +25 mV vs. Ag/AgCl (see Figure 4.6), which probably was a factor in the low corrosion rate due to a smaller potential difference between the surface in the crevice and the outside sample surface.

The number of parallels for each condition also presents a setback in terms of accuracy and precision. Nevertheless, some scatter in the critical temperatures is expected, especially from the attacks involving crevice corrosion which is highly stochastic in nature.

Finally, one important drawback from critical temperature experiments is that starting the material off in the electrolyte at a low temperature, where localized corrosion does not initiate, and increasing the temperature in steps until initiation, actually gives the material the chance to improve its passive layer which results in higher critical temperatures [56]. This so-called mild start-up period is the reason why a long-term immersion test was carried out.

Long-term exposure

Increasing the temperature from room temperature to 40 °C mitigated the effects of a mild start-up. This is evidenced by the fact that all polarized coated samples initiated corrosion in this test at 40 °C, compared with the fact that the T$_{crit}$ obtained in the critical corrosion test with the same type of samples were higher and, for one of the pickled, coated TIG-welded samples polarized to +400 mV vs. Ag/AgCl, this temperature reached 51 °C. Still,

many coated samples, at OCP and polarized, in the critical temperature test did corrode at temperatures in the range of 40–45 °C so the effect of the mild start-up period was probably not seen to its full extent. Furthermore, prior to the temperature increase to 40 °C, the samples were immersed in natural seawater at OCP and room temperature for a day which also helps improve the passive layer and also counts as a mild start-up.

For the samples exposed at OCP, the TIG-welded, not pickled, coated sample was the only one to initiate corrosion during the test and, most notably, it initiated corrosion during the first day when the electrolyte was at room temperature. This further demonstrates the significant effect of pickling since the pickled sample did not initiate even after two months at 40 °C.

The polarized TIG-welded, pickled, coated sample initiated 16 days after the temperature change, suggesting a more resistant behavior in line with what is expected from a pickled sample. Nonetheless, all the samples corroded, indicating 40 °C is not a safe temperature for welded coated samples whose OCP is able to rise to +400 mV vs. Ag/AgCl in natural seawater. Another important aspect is the gradual increase in anodic current density of the polarized, not pickled, coated, TIG- and laser-welded samples at room temperature. Even though this increase was very low and absent in the pickled condition, it was enough to cause visible damage in the sample and to question whether or not the current would continue to increase at room temperature, considering the TIG-welded, not pickled coated sample at OCP also initiated at room temperature this might be a possibility.

No ennoblement due to biofilm was seen in any of the samples exposed at OCP which was expected (see Section 3) as most biofilms are not able to form in temperatures above 35 - 40 °C. Since all the polarized samples corroded at 40 °C, and two of these samples started to corrode already at approximately 23 °C, it would follow that it is a possibility that the critical temperature of the coated material is below 35 °C, where biofilm could form, ennobling the material and leading to localized corrosion attacks in the field. Nevertheless, without testing more parallels than one, especially for the pickled samples, all these inferences are not conclusive.

In the critical corrosion temperature test the potential of the samples (OCP or +400 mV vs. Ag/AgCl) had a significant effect. This was also the case for the long-term exposure test. The effect of the potential of the samples on T_{crit} emphasizes the argument mentioned in Section 3 that results from ASTM G48 tests, where the potential of the sample can reach +600 to +650 mV vs. SCE, should not be confused with fitness for purpose. This also makes the results from the samples polarized to +400 mV vs. Ag/AgCl the most relevant for application at Bjørnafjorden.

SEM/EDS

All SEM images indicate no heightened susceptibility in either ferrite or austenite as no selective attacks initiated in any of the samples examined.

In all pits investigated, the inside of the pit or crevice had the highest PRE_N* compared to other areas including the bulk material investigated in the cross-sectional images. The exception to this was the pit outside of the coating in the polarized, TIG-welded, not pickled, coated sample in which only two points at the mouth of the pit had a high PRE_N* while the inside of the pit, except for Spot 14, has low values. Even if the salts present in this pit were removed from the analysis, the pit would still have lower PRE_N* than the other pits. The abnormal amount of Si seen in this pit compared to all other sites investigated indicates the possibility the analysis of this pit is an outlier. Regarding the other pits and the crevice, the reason the insides of the pits/crevice have a higher PRE_N* than, for example, the bulk material, may be related to the fact that these samples repassivated during the test. In acidic media, passive films have shown to be enriched with Cr compared to the underlying material as a result of the dissolution of Fe [96]; additionally, in the presence of chlorides, Fe and Ni have been shown to dissolve preferentially from the passive film [22]. If the pit/crevice managed to maintain an acidic environment during repassivation, and since repassivation took place in the test electrolyte, the new passive layer of the material would have experienced the dissolution of Fe and Ni. This would then lead to higher relative amounts of Cr and Mo and, thus, higher PRE_N*.

BSE and EBSD

The lack of intermetallic phases precipitated indicates a good quality of the weld. Nevertheless, the possibility of Cr-nitride precipitation cannot be discarded as it is possible these were not detected due to their small size [31].

Moreover, there is a marked difference between the weld and base microstructures in line with the theory. The microstructure in the weld is clearly similar to that of cast material including intergranular austenite grains, as well as intragranular and Widmannstäten austenite.

The TIG-weld quality can be appreciated further in the phase balance presented in Figure 4.56a-4.56c where, even though the ferrite content increased in the HAZ and the weld, it is still close but below 50 %. Especially in the HAZ whose ferrite grains seemed to have coarsened slightly (see Figure 4.56h) compared to the base material. As mentioned in Chapter 2, the ferrite content should be below 65% to be able to maintain corrosion resistance and mechanical properties.

The critical temperatures found in the critical corrosion tests then correspond to those of a good weld produced by using an appropriate heat input and cooling rate; therefore, it is still possible to get even lower T_{crit} than those found earlier if the ferrite composition is more than 65 % and/or secondary phases precipitate.

XPS

Pertaining the occurrence of Cr at the surfaces of the material, $Cr(OH)_3$ and Cr_2O_3 were expected to be found predominantly at the surface of the material due to the nature of passive films [96]. Nevertheless, the differences in proportions of the different Cr species between the pickled and not pickled samples were unpredicted. According to the results obtained in this work, Cr_2O_3 is more predominant than $Cr(OH)_3$ at the surface of the not pickled base material, while for the pickled base material they are present in the same proportions. Additionally, the Cr_2O_3 content in the pickled HAZ and weld is lower than what is found at the not pickled HAZ and weld. Given how the corrosion properties of stainless steel rely mostly on Cr_2O_3, these results alone would point out a better corrosion resistance of the not pickled HAZ and weld over the same pickled areas incongruent with Chapter 2-3 and the previous results from this work. Further, CrO_3 is found in the pickled HAZ in slightly, higher proportions than Cr_2O_3; the passive film in this pickled area then can be regarded as more susceptible to attacks given the high solubility of CrO_3 in aqueous media [96]. Additionally, in Figure 4.58, the not pickled base material, and the pickled base material, HAZ and weld show an increase in Cr content with sputtering time making it the predominant species in these regions, whereas the not pickled HAZ shows $Cr(OH)_3$ and Cr_2O_3 remain the most predominant species with sputter time, and Cr_2O_3 remains more predominant for the not pickled weld. These results could be hinting at a better corrosion resistance of the not pickled HAZ and weld. Nonetheless, when factoring Fe into the equation, it can be seen in Figure 4.59 that the Fe/Cr ratio is, as expected, significantly higher for the not pickled material than for the pickled material and highest at the weld followed by the HAZ. Considering also how the Fe content is higher than the Cr content in all zones as shown in Figure 4.60, it then makes sense the weld and HAZ of the not pickled material are more susceptible to corrosion attacks. Furthermore, Cr_2O_3 being more predominant than $Cr(OH)_3$ at the surface of the not pickled base material, while for the pickled base material they are present in the same proportions, is not necessarily an indication of a smaller hydroxide concentration in the not pickled sample given how this analysis is not taking into account the Fe species which are expected to be predominant in the hydroxide layer of the not pickled sample but have dissolved and are absent in the pickled condition, thus improving its corrosion resistance.

Relevant results for Bjørnafjorden bridge

The temperature of the water in Bjørnafjorden has been measured by the NPRA 2 m below the surface since 2015 [97, 98]. The temperatures in this location were found to be below 20 °C. The measurements are planned to continue until 2020 but the results so far have been confirmed with modelled data provided by the Norwegian Institute of Marine Research (Havforskningsinstituttet).

According to the literature survey and the results from this project, the most relevant results for the Bjørnafjorden bridge correspond to those of the TIG-welded samples polarized to +400 mV vs. Ag/AgCl which simulate biofilm formation. The T_{crit} for these samples, not including those pre-cathodically polarized, are in the range 44–72 °C. However, the long-term exposure test showed that, if biofilm is still present at temperatures approaching 40 °C, corrosion can initiate. A momentary increase in temperature at Bjørnafjorden, e.g. due to heat from the sun, can cause corrosion to initiate and then corrosion can propagate even as the temperature is decreased. Moreover, since the tests could not be carried at temperatures below 22 to 25 °C, the lowest temperature limit for corrosion

propagation was not determined. Therefore, the possibility of corrosion propagation for SDSSs welds at the recorded normal temperatures at Bjørnafjorden, which are less than 20 °C, cannot be discarded.

It is also important, since the pontoons with be cathodically protected with anodes, that the CP is not stopped (e.g. all anodes consumed and/or no protection from the connected carbon steel) during use. The results from this thesis show that corrosion can initiate quickly after removing the CP at very low temperatures and continue to propagate at temperatures below 21 °C even if no crevices are present.

4.4 Conclusion

The critical corrosion temperature tests showed that TIG welding SDSS causes a decrease in T_{crit} of at least 17 °C compared to the base material while the long-term exposure tests showed that 40 °C is not a safe temperature for coated welded samples polarized to +400 mV vs. Ag/AgCl. For pickled TIG-welded samples, the potential of the sample (OCP or +400 mV vs. Ag/AgCl) had a bigger impact on T_{crit} than the presence of crevices. Moreover, while pickling was shown to have a significant positive effect on T_{crit}, its effects were not significant for samples that were both polarized and coated.

Although the effects of sample potential and presence of crevices are highly significant, these are not as impactful as the effects of pre-cathodic polarization. The pickled TIG-welded pre-cathodically polarized samples initiated at 24 °C and brown rust was already seen at room temperature. It is therefore pivotal that CP applied to the pontoons at Bjørnafjorden is not disconnected during service.

Some samples managed to repassivate at temperatures between 23–38 °C while others continued to corrode at temperatures below 23 °C. This means that, once initiated, corrosion can continue to propagate at Bjørnafjorden. Additionally, such low repassivation temperatures make the 20 °C temperature limit stated by NORSOK M-001 and ISO 21457 seem more sensible. Nevertheless, if the limits make a distinction between welded and base material, the limits for base material can be reconsidered. Moreover, the even if corrosion propagates at lower temperatures, the corrosion rate is still reduced significantly as temperature decreases.

The material characterization of the samples showed, among others, that no selective attacks took place on either austenite or ferrite, intermetallic phases such as σ or χ did not precipitate, and that the pickled condition had a good passive layer rich in Cr species compared to Fe species. This means the T_{crit} obtained correspond to those of a good TIG weld. Lower T_{crit} can be obtained if the welding parameters are chosen poorly.

Chapter 5

Further work

This thesis studied a limited number of parallel samples for each welded condition. More tests of the same nature, with more parallels, should be performed to draw more accurate conclusions about the localized corrosion behavior of welded SDSS in seawater. Furthermore, a different way to assess corrosion initiation of samples exposed at OCP should perhaps be used to produce more accurate results.

The long-term exposure tests showed that 40 °C is not a safe temperature for welded samples polarized to +400 mV vs. Ag/AgCl. The same test can be performed at 30 °C to determine if this is a safe working temperature for SDSS.

The repassivation behavior of welded SDSS was evaluated by decreasing the temperature at a faster rate than the one used to initiate corrosion of the samples. It is worth investigating the effect of decreasing the temperature by a few degrees to a fixed temperature after corrosion initiation to check if corrosion propagation can stop after several hours at the fixed temperature.

This master's thesis showed that the welding procedure and surface condition have a great impact on the T_{crit} of the sample. The welded parameters can be modified in order to either increase T_{crit}, by, for example, using a N-containing backing gas, or decrease T_{crit} by, for example, introducing intermetallic phases. It is therefore important for the NPRA to test the exact welding procedure to be used and the surface treatments that will be employed, in order to determine a more relevant T_{crit}.

For the Bjørnafjorden bridge specifically, a continuation of this work, focusing on simulating the splash zone instead of the purely immersed condition is also important. Due to periodical wet and dry cycles, the splash zone experiences, among others, the increase in concentration of chlorides due to evaporation. This condition, combined with the SDSS being heated by the sun, and the possible formation of crevices due to macrofouling, make the splash zone a critical component.

Bibliography

[1] The Norwegian Public Roads Administration, "Fjordkryssing - Bjørnafjorden." `https://www.vegvesen.no/Europaveg/e39stordos/fjordkryssing-bjornafjorden`. Accessed: 10.04.2019.

[2] F. Langfitt, "Norway Embarks On Its Most Ambitious Transport Project Yet." `https://www.npr.org/2019/01/08/682222168/norway-embarks-on-its-most-ambitious-transport-project-yet?t=1560718300758`, Jan. 2019. Accessed: 10.04.2019.

[3] The Norwegian Public Roads Administration, "Arbeidet med val av flytebru er i gang." `https://www.vegvesen.no/Europaveg/e39stordos/nyhetsarkiv/arbeidet-med-val-av-flytebru-er-i-gang`, 2018. Accessed: 10.04.2019.

[4] J. I. Skar and S. Olsen, "A Review of Materials Application Limits in NORSOK M-001 and ISO 21457," *CORROSION*, vol. 73, no. 6, pp. 655–665, 2017.

[5] NORSOK M-001, "Materials selection." Fifth ed., 2014.

[6] ISO 21457, "Petroleum, petrochemical and natural gas industries – Materials selection and corrosion control for oil and gas production systems." First ed., 2010.

[7] A. Rueda, "Corrosion properties of 25Cr super duplex stainless steel in the splash zone," Dec. 2018. Specialization project as part of the subject TMT4500 Materials Technology.

[8] J. Lai, C. H. Shek, and K. H. Lo, *Stainless Steels: An Introduction and Their Recent Developments*, ch. 5 - Duplex Stainless Steels, pp. 52–63. Dubai, United Arab Emirates: Bentham Science Publishers, first ed., 2012.

[9] J. R. Davis, *Stainless steels*, ch. Metallurgy and Properties of Wrought Stainless Steels, pp. 13–65. ASM specialty handbook, Materials Park, Ohio, USA: ASM International, 1994.

[10] J. Charles, *Duplex Stainless Steels '91*, vol. 1, ch. The duplex stainless steels: materials to meet your needs, pp. 3–48. Beaune, Bourgogne, France: Les éditions de physique, 1991.

[11] H. Bhadeshia and R. Honeycombe, *Steels: Microstructure and Properties*, ch. 12 - Stainless Steel, pp. 343–376. Butterworth Heinemann, fourth ed., 2017.

[12] U. Kivisäkk, *Marine corrosion of stainless steels (EFC 33): testing, selection, experience, protection, and monitoring*, ch. 12 - Duplex Stainless Steels in Sea Water - Instructions For Good Practice and Results From Exposure of Butt-Welded Tubes, pp. 130–144. Materials Science Series, London, UK: IOM Communications, 2001.

[13] A. J. Sedriks, *Corrosion of stainless steels*, ch. 2 - Composition, structure, and mechanical properties, pp. 13–78. Corrosion monograph series, New York, USA: Wiley, second ed., 1996.

[14] H. D. Solomon, "Age hardening in a duplex stainless steel," *Journal of Heat Treating*, vol. 3, no. 1, p. 4, 1983.

[15] J. R. Davis, *Stainless steels*, ch. Metallurgy and Properties of Wrought Stainless Steels, p. 32. ASM specialty handbook, Materials Park, Ohio, USA: ASM International, 1994.

[16] Sandvik, "SANDVIK SAF 2707 HD™ HYPER-DUPLEX STAINLESS STEEL." `https://www.materials.sandvik/en/products/tube-pipe-fittings-and-flanges/high-performance-materials/duplex-stainless-steel/sandvik-saf-2707-hd/`. Accesssed: 13.06.2019.

[17] J. R. Davis, *Stainless steels*, ch. General Introduction, p. 3. ASM specialty handbook, Materials Park, Ohio, USA: ASM International, 1994.

[18] C.-O. A. Olsson and D. Landolt, "Passive films on stainless steels - chemistry, structure and growth," *Electrochimica Acta*, vol. 48, pp. 1093–1104, 04 2003.

[19] A. J. Sedriks, *Corrosion of stainless steels*, ch. 3 - Electrochemistry, pp. 79–101. Corrosion monograph series, New York, USA: Wiley, second ed., 1996.

[20] D. Landolt, *Corrosion and surface chemistry of metals*, ch. 6 - Passivity of metals, pp. 227–274. Lausanne, Switzerland: EPFL Press, 2007.

[21] A. J. Sedriks, *Corrosion of stainless steels*, ch. 3 - Electrochemistry, p. 32. Corrosion monograph series, New York, USA: Wiley, second ed., 1996.

[22] A. Kocijan, Č. Donik, and M. Jenko, "The corrosion behaviour of duplex stainless steel in chloride solutions studied by XPS," *Materiali in Tehnologije*, vol. 43, pp. 195–199, 07 2009.

[23] C.-O. A. Olsson, S. Malmgren, M. Gorgoi, and K. Edström, "Quantifying the Metal Nickel Enrichment on Stainless Steel," *Electrochemical and Solid-State Letters*, vol. 14, pp. C1–C3, 11 2010.

[24] E. Gardin, S. Zanna, A. Seyeux, A. Allion-Maurer, and P. Marcus, "Comparative study of the surface oxide films on lean duplex and corresponding single phase stainless steels by XPS and ToF-SIMS," *Corrosion Science*, vol. 143, pp. 403–413, Oct. 2018.

[25] J. Charles, *Duplex Stainless Steels '91*, vol. 1, ch. Super duplex stainless steels: structure and properties, pp. 151–168. Beaune, Bourgogne, France: Les éditions de physique, 1991.

[26] J.-O. Nilsson, "Super duplex stainless steels," *Materials Science and Technology*, vol. 8, no. 8, pp. 685–700, 1992.

[27] J. Charles, *Duplex Stainless Steels '91*, vol. 1, ch. Super duplex stainless steels: structure and properties, p. 158. Beaune, Bourgogne, France: Les éditions de physique, 1991.

[28] B. Josefsson, J.-O. Nilsson, and A. Wilson, *Duplex Stainless Steels '91*, vol. 1, ch. Phase transformations in duplex steels and the relation between continuous cooling and isothermal heat treatment, pp. 67–78. Beaune, Bourgogne, France: Les éditions de physique, 1991.

[29] C. Torres, R. Johnsen, H. Østvold, M. Bernås, and M. Iannuzzi, "Effect of W on Phase Transformation Kinetics and Its Correlation with Localized Corrosion Resistance for UNS S39274," in *CORROSION 2019*, (Nashville, Tennessee, USA), NACE International, Mar. 2019. ID: NACE-2019-13233.

[30] C. Torres, R. Johnsen, H. Østvold, M. Bernås, and M. Iannuzzi, "Effect of W on Phase Transformation Kinetics and Its Correlation with Localized Corrosion Resistance for UNS S39274," in *CORROSION 2019*, (Nashville, Tennessee, USA), p. 7, NACE International, Mar. 2019. ID: NACE-2019-13233.

[31] N. Llorca-Isern, I. López-Jiménez, H. López-Luque, M. V. Biezma, and A. Roca, "Study of the Precipitation of Secondary Phases in Duplex and Superduplex Stainless Steel," in *THERMEC 2016*, vol. 879 of *Materials Science Forum*, pp. 2537–2542, Trans Tech Publications Ltd., 2 2017.

[32] J. R. Davis, *Stainless steels*, ch. Welding, pp. 240–401. ASM specialty handbook, Materials Park, Ohio, USA: ASM International, 1994.

[33] J. C. Lippold and D. J. Kotecki, *Welding Metallurgy and Weldability of Stainless Steels*, ch. 7 - Duplex stainless steels, pp. 230–263. New Jersey, USA: John Wiley & Sons, 2005.

[34] C. F. G. Baxter, A. W. Stevenson, and G. R. Warburton, "Welding of Zeron 100 Super Duplex Stainless Steel," in *The Third International Offshore and Polar Engineering Conference*, (Singapore), International Society of Offshore and Polar Engineers, June 1993. ID: ISOPE-I-93-376.

[35] R. W. Messler Jr, *Principles of Welding: processes, Physics, Chemistry, and Metallurgy*, ch. 2 - Classifying Welding Processes, p. 38. New York, USA: John Wiley & Sons, 1999.

[36] R. W. Messler Jr, *Principles of Welding: processes, Physics, Chemistry, and Metallurgy*, ch. 3 - Fussion Welding Processes, pp. 51–55. New York, USA: John Wiley & Sons, 1999.

[37] S. Katayama, *Handbook of Laser Welding Technologies*, ch. 1- Introduction: fundamentals of laser welding. No. 41 in Woodhead Publishing Series in Electronic and Optical Materials, Woodhead Publishing, 2013.

[38] M. Bolut, C. Y. Kong, J. Blackburn, K. A. Cashell, and P. R. Hobson, "Yb-fibre Laser Welding of 6 mm Duplex Stainless Steel 2205," *Physics Procedia*, vol. 83, pp. 417–425, Sept. 2016.

[39] M. Landowski, "Influence of Parameters of Laser Beam Welding on Structure of 2205 Duplex Stainless Steel," *Advances in Materials Science*, vol. 19, pp. 21–31, Mar. 2019.

[40] J. Zhou, *Handbook of Laser Welding Technologies*, ch. 5 - Developments in pulsed and continuous wave laser welding technologies, pp. 103–138. No. 41 in Woodhead Publishing Series in Electronic and Optical Materials, Woodhead Publishing, 2013.

[41] L. Quintino, R. M. Miranda, S. Williams, and C. J. Kong, "Gas shielding in fiber laser welding of high strength pipeline steel", Science and Technology of Welding and Joining," *Science and Technology of Welding & Joining*, vol. 16, no. 5, pp. 399–404, 2011.

[42] L. van Nassau, H. Meelker, and J. Hilkes, *Duplex Stainless Steels '91*, vol. 1, ch. Welding duplex and super-duplex stainless steel, pp. 303–323. Beaune, Bourgogne, France: Les éditions de physique, 1991.

[43] P. Combrade and J.-P. Audouard, *Duplex Stainless Steels '91*, vol. 1, ch. Duplex stainless steels and localized corrosion resistance, pp. 303–323. Beaune, Bourgogne, France: Les éditions de physique, 1991.

[44] J. R. Davis, *Stainless steels*, ch. Corrosion of Weldments, p. 2. ASM specialty handbook, Materials Park, Ohio, USA: ASM International, 1994.

[45] T. G. Gooch, *Duplex Stainless Steels '91*, vol. 1, ch. Corrosion resistance of welds in duplex stainless steels, pp. 325–346. Beaune, Bourgogne, France: Les éditions de physique, 1991.

[46] L. Odegard and S.-A. Fager, *Duplex Stainless Steels '91*, vol. 1, ch. The root side pitting resistance of stainless steel welds, pp. 451–460. Beaune, Bourgogne, France: Les éditions de physique, 1991.

[47] ASTM A380/A380M, "Standard Practice for Cleaning, Descaling, and Passivation of Stainless Steel Parts, Equipment, and Systems," 2017.

[48] J. R. Davis, *Stainless steels*, ch. Surface Engineering, pp. 421–436. ASM specialty handbook, Materials Park, Ohio, USA: ASM International, 1994.

[49] Z. Zhang, H. Zhang, J. Hu, X. Qi, Y. Bian, A. Shen, P. Xu, and Y. Zhao, "Microstructure evolution and mechanical properties of briefly heat-treated SAF 2507 super duplex stainless steel welds," *Construction and Building Materials*, vol. 168, pp. 338–345, Apr. 2018.

[50] A. J. Sedriks, *Corrosion of stainless steels*, ch. 4 - Pitting, pp. 102–175. Corrosion monograph series, New York, USA: Wiley, second ed., 1996.

[51] G. S. Frankel, *ASM Handbook, Volume 13A - Corrosion: Fundamentals, Testing, and Protection*, ch. Pitting corrosion, pp. 236–241. ASM International, 2003.

[52] H.-H. Strehblow, V. Maurice, and P. Marcus, *Corrosion Mechanisms in Theory and Practice (Corrosion Technology Book 26)*, ch. 7 - Mechanisms of Pitting Corrosion, pp. 349–393. Boca Raton, Florida, USA: CRC Press, 2011.

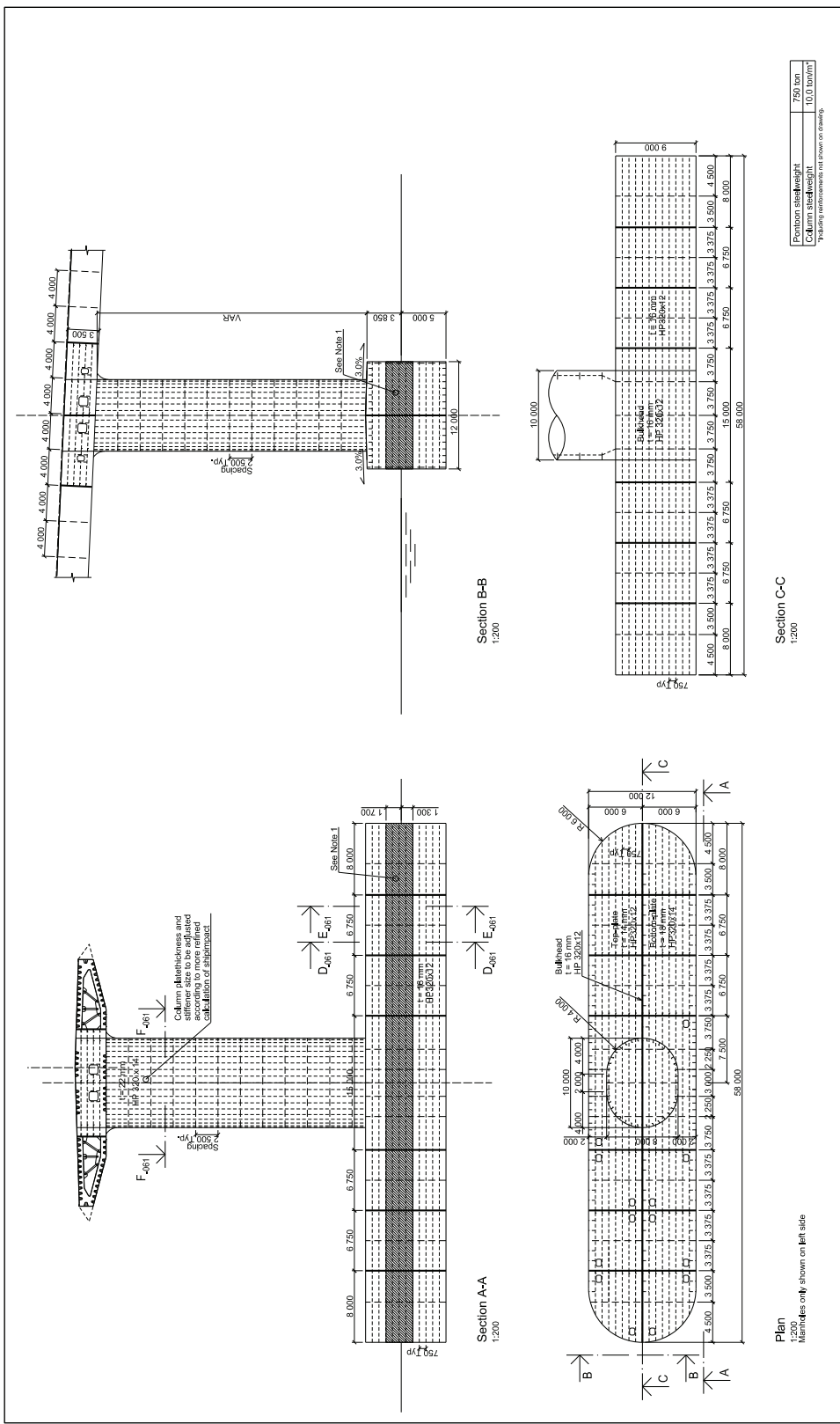[53] R. J. Brigham and E. W. Tozer, "Temperature as a Pitting Criterion," *CORROSION*, vol. 29, no. 1, pp. 33–36, 1973.

[54] J. O. Park, S. Matsch, and H. Böhni, "Effects of Temperature and Chloride Concentration on Pit Initiation and Early Pit Growth of Stainless Steel," *Journal of The Electrochemical Society*, vol. 149, no. 2, pp. B34–B39, 2002.

[55] B. Baroux, *Corrosion Mechanisms in Theory and Practice (Corrosion Technology Book 26)*, ch. 9 - Further Insights on the Pitting Corrosion of Stainless Steels, pp. 419–447. Boca Raton: CRC Press, 2011.

[56] B. Wallén, "Corrosion of duplex stainless steels in seawater," *Avesta Corrosion Management and Application Engineering*, 1998. Avesta Sheffield AB, Avesta, Sweden.

[57] P. Combrade, *Corrosion Mechanisms in Theory and Practice (Corrosion Technology Book 26)*, ch. 10 - Crevice Corrosion of Metallic Materials, pp. 449–498. Boca Raton, Florida, USA: CRC Press, 2011.

[58] A. J. Betts and L. H. Boulton, "Crevice corrosion: review of mechanisms, modelling, and mitigation," *British Corrosion Journal*, vol. 28, no. 4, pp. 279–296, 1993.

[59] J. W. Oldfield and W. H. Sutton, "Crevice Corrosion of Stainless Steels: I. A Mathematical Model," *British Corrosion Journal*, vol. 13, no. 1, pp. 13–22, 1978.

[60] S. Valen, P. O. Gartland, and U. Steinsmo, *Marine Corrosion of Stainless Steels (EFC 10): Chlorination and Microbial Effects*, ch. 10 - Effect of Temperature on Initiation, Repassivation and Propagation of Crevice Corrosion of High-Alloy Stainless Steels in Natural Seawater, pp. 114–127. Maney Publishing, 1993.

[61] A. P. Bond and H. J. Dundas, "Resistance of Stainless Steels to Crevice Corrosion in Seawater," *Materials Performance*, vol. 23, no. 7, pp. 39–43, 1984.

[62] J. S. Kim, P. J. Xiang, and K. Y. Kim, "Effect of Tungsten and Nickel Addition on the Repassivation Behavior of Stainless Steel," *CORROSION*, vol. 61, no. 2, pp. 174–183, 2005.

[63] J.-O. Nilsson, P. Kangas, A. Wilson, and T. Karlsson, "Mechanical properties, microstructural stability and kinetics of σ-phase formation in 29Cr-6Ni-2Mo-0.38N superduplex stainless steel," *Metallurgical and Materials Transactions A*, vol. 31, pp. 35–45, Apr. 2000.

[64] E. B. Haugan, M. Næss, C. T. Rodriguez, R. Johnsen, and M. Iannuzzi, "Effect of Tungsten on the Pitting and Crevice Corrosion Resistance of Type 25Cr Super Duplex Stainless Steels," *CORROSION*, vol. 73, pp. 53–67, 08 2016.

[65] A. J. Sedriks, *Corrosion of stainless steels*, ch. 5 - Crevice corrosion, pp. 176–230. Corrosion monograph series, New York, USA: Wiley, second ed., 1996.

[66] F. P. Ijsseling, *Marine Corrosion of Stainless Steels (EFC 10): Chlorination and Microbial Effects*, ch. 1 -Aspects of Marine Corrosion and Testing for Seawater Applications, pp. 1–20. Maney Publishing, 1993.

[67] M. A. O. Alum, "Localized Pitting Corrosion of Super Duplex Stainless Steel in a Sea Water Application: Practical Case of When Chlorination was Not to Blame," in *SPE Nigeria Annual International Conference and Exhibition*, (Lagos, Nigeria), Society of Petroleum Engineers, Aug. 2017. ID: SPE-189091-MS.

[68] J. Eidhagen and U. Kivisäkk, "Sandvik SAF 2507® in service for twenty years in seawater applications," *Stainless Steel World*, Dec. 2010.

[69] ASTM G48-11, "Standard Test Methods for Pitting and Crevice Corrosion Resistance of Stainless Steels and Related Alloys by Use of Ferric Chloride Solution," 2011.

[70] ASTM G150-13, "Standard Test Method for Electrochemical Critical Pitting Temperature Testing of Stainless Steels," 2013.

[71] T. Mathiesen, T. S. Nielsen, T. Haugen, B. Espelid, P. Hummelgaard, and K. Vilpponen, "Improved method for ASTM G48 corrosion testing of welds," techreport TR 548, Nordic Innovation Center, Oslo, Norway, Mar. 2004.

[72] M. Bernås, I. Westermann, R. Johnsen, C. Lauritsen, and M. Iannuzzi, "Effect of Microstructure on the Corrosion Resistance of Duplex Stainless Steels: Materials Performance Maps," in *CORROSION 2017*, (New Orleans, Louisiana, USA), NACE International, Mar. 2017. ID: NACE-2017-8923.

[73] R. M. Kain, *ASM Handbook, Volume 13A - Corrosion: Fundamentals, Testing, and Protection*, ch. Evaluating Crevice Corrosion, pp. 549–561. ASM International, 2003.

[74] R. Holthe, *Cathodic and anodic properties of stainless steel in seawater*. Dr.Ing. thesis, Trondheim, Norway: Universitetet i Trondheim, Norges Tekniske Høgskole, Institutt for materialer og bearbeiding, 1988.

[75] R. Johnsen and E. Bardal, "The effect of a microbiological slime layer on stainless steel in natural sea water," in *Corrosion 86*, (Hourston, Texas, USA), NACE, 1986. Paper no. 227.

[76] F. P. Ijsseling, *Survey of literature on crevice corrosion (1979-1998) (EFC30): mechanisms, test methods and results, practical experience, protective measures and monitoring*, ch. 4 -Mechanisms, Conditions, Applications and Experimental Results of Specific Alloy Types, pp. 71–96. IOM Communications, 2000.

[77] N. Larché and D. Thierry, "Potential ennoblement on stainless steel and implication on crevice corrosion in natural seawater," in *2nd Conference & Expo Genoa 2018*, (Genoa, Italy), French Corrosion Institute, NACE International, May 2018.

[78] F. P. Ijsseling, *Survey of literature on crevice corrosion (1979-1998) (EFC 30): mechanisms, test methods and results, practical experience, protective measures and monitoring*, ch. 4 - Mechanisms, Conditions, Applications and Experimental Results of Specific Alloy Types, p. 90. IOM Communications, 2000.

[79] R. Johnsen and H. Vingsand, "Corrosion Properties of UNS S32750, UNS N06022 and UNS N10276 in Seawater," in *CORROSION 2009*, (Atlanta, Georgia, USA), NACE International, Mar. 2009. ID: NACE-09195.

[80] H. H. Olavesen, "The Effect of Hydrogen on the Corrosion Resistance of Stainless Steel in Seawater," Master's thesis, NTNU, Trondheim, Norway, 2018.

[81] R. Johnsen, "Stainless steels in seawater systems," in *NITO Conf.*, (Amsterdam, The Netherlands), The Norwegian Society of Engineers, in cooperation with Nickel Development Institute, Feb. 1990.

[82] S.-A. Fager and L. Odegard, "Welding of the Super Duplex Stainless Steel Sandvik SAF2507™ (UNS S32750)," in *The Third International Offshore and Polar Engineering Conf.*, (Singapore), International Society of Offshore and Polar Engineers, June 1993. ID: ISOPE-I-93-377.

[83] M. De Marco and M. Palombo, "What's Wrong with ASTM G48 Qualification Test in Duplex SS welds?," in *CORROSION 2019*, (Nashville, Tennessee, USA), NACE International, Mar. 2019. ID: NACE-2019-13118.

[84] T. Rogne, J. M. Drugli, and S. Valen, "Testing of Stainless Steel Welds for Various Applications," *CORROSION*, vol. 48, no. 10, pp. 864–870, 1992.

[85] ASTM D-1141, "Standard Practice for the Preparation of Substitute Ocean Water," 2013.

[86] R. Johnsen, "Effect of insufficient backing gas on corrosion properties of 22Cr, 25Cr duplex stainless steel and Ti Gr. 2," techreport 90183100-01, Department of Mechanical and Industrial Engineering (MTP) at NTNU, Trondheim, Norway, June 2017. Restricted.

[87] R. Pettersson, M. Johansson, and E. M. Westin, "Corrosion Performance of Welds in Duplex, Superduplex and Lean Duplex Stainless Steels," *Rivista Italiana della Saldatura*, vol. 66, pp. 335–343, 01 2013.

[88] E. Westin and D. Serrander, "Experience In Welding Stainless Steels For Water Heater Applications," *Welding in the World*, vol. 56, pp. 14–28, 05 2013.

[89] R. Johnsen, H. Olavesen, A. H. Zavieh, and T. L. Erlien, "Effect of Cathodic Polarization on Localized Corrosion of 25Cr in Seawater," in *CORROSION 2019*, (Nashville, Tennessee, USA), NACE International, Mar. 2019. ID: NACE-2019-12870.

[90] O. Ø. Knudsen, "Felttest av superduplex stål med sveis," tech. rep., SINTEF, Nov. 2018.

[91] Metrode Products Ltd, "ZERON-100X-TIG." `http://www.metrode.com/en-gb/alloy-families/stainless-steels/duplex-and-superduplex-for-the-offshore-industry/product/zeron-100x-tig.html`. Accesssed: 01.05.2019.

[92] Outokumpu, "Forta SDX 2507." `http://steelfinder.outokumpu.com/GradeDataSheetv3PDF.aspx?OKGrade=2507&Category=Forta`. Accesssed: 01.05.2019.

[93] Jotun, "Jotamastic 87." `https://www.jotun.com/me/en/b2b/paintsandcoatings/products/Jotamastic-87.aspx`. Accesssed: 01.05.2019.

[94] Alicona, "InfiniteFocus." `https://www.alicona.com/products/infinitefocus/`. Accessed: 10.12.2018.

[95] A. H. Zavieh and N. Espallargas, "The role of surface chemistry and fatigue on tribocorrosion of austenitic stainless steel," *Tribology International*, vol. 103, pp. 368–378, 2016.

[96] D. Landolt, *Corrosion and surface chemistry of metals*, ch. 6 - Passivity of metals, pp. 243–246. Lausanne, Switzerland: EPFL Press, 2007.

[97] Øyvind Thiem (Statens vegvesen), "Målte sjøtettheter Bjørnafjorden," Oct. 2018. Technical report shared internally.

[98] The Norwegian Public Roads Administration, "Sammenligning mellom målte og modellerte sjøtemperaturer for Bjørnafjorden," Oct. 2018. Technical report shared internally.

Appendix

A   Pontoon design

Section B-B
1:200

Section A-A
1:200
Manholes only shown on left side

Section C-C
1:200

Plan
1:200
Manholes only shown on left side

4 000 4 000 4 000 4 000 4 000 4 000
3 500
VAR
5 000   3 850
12 000
3.0%
See Note 1
Spacing 2 500 Typ.
t = 16 mm
HP 326x32

58 000
4 500 3 500 3 375 3 375 3 750 3 750 3 750 3 750 3 375 3 375 3 375 3 500
15 000
10 000
750 Typ.
t = 16 mm
HP 326x32
Bulkhead
t = 16 mm
HP 380x12

9 000
8 000 3 500 3 375 3 375 6 750 6 750 6 750 4 500

1 700
1 300
8 000
6 750 6 750
See Note 1
t = 22 mm
HP 430x20

D₀61 E₀61
F₀61

Column plate thickness and stiffener size to be adjusted according to more refined calculation of shipimpact.

12 000
9 000 9 000
R 6 000
R 6 000
10 000
4 000 4 000
2 000 2 000
750 Typ.
Bulkhead
t = 16 mm
HP 320x12
Top plate
t = 14 mm
HP 320x12
Bottom plate
t = 16 mm
HP 320x14

Remarks:
Note 1: 25Cr SDSS
Super Duplex Stainless Steel with 25 % Cr.
Note 2: Two access manholes with access ladder to each compartment

Directions:
1. Structural design according to NPRA Handbook R762, N400 and Eurocode 3 (NS-EN-1993) or equivalent DNVGL standards.
2. Steel quality in plates: S420 MPa
3. Steel quality in stiffeners: S355 MPa
4. All measurements in mm.

References:
-

B   Material certificate for TIG-welded SDSS samples

CERTIFICATE - ZEUGNIS - CERTIFICAT
EN 10204-3.1
2453708-EN

Invoice No.	Page
Rechnung Nr.	Seite
N° de facture	Page
6610/1000568450	1/1

Business Unit / QCM	Date Datum Date	Load, Ladung, Charge No	Acknowledged ID, Bestätigung, Commande ID
Avesta Works / Johan Nordström	08-Aug-2017	SE/152639	6610/300430287

Your ref, Ihre Ref., Votre ref
test samples.

Buyer, Besteller, Acheteur
Outokumpu Nirosta GmbH
Oberschlesienstr. 16
DE 47807, Krefeld
GERMANY

Requirements, Anforderungen, Exigences
ASTM A 240M-16a
ASME BPVC SEC II PART A SA-240/SA-240M 2015
EN 10088-2:2014
EN 10028-7:2016
EN ISO 9444-2 / ASTM A480M

Consignee, Empfänger, Lieu de livraison
Outokumpu Stainless AB

Mark of Manufacturer Zeichen des Lieferwerkes Signe de producteur	Process Erschmelzungsart Mode de fusion	Inspector's stamp Zeichen des Sachverständigen Poicon de l'expert	Grade, Werkstoff, Nuance
outokumpu	E+AOD	AJA	Outokumpu Forta SDX 2507 UNS S32750 1.4410

Product, Erzeugnisform, Produit
Stainless Steel Hot Rolled, Coil-Plate
finish 1D, cut edge

Line Reihe Ligne	Item Position Poste	Heat-Lot No Schmelze-Lot Nr Coulée n° - Lot No	Size Abmessungen Dimensions	Pieces Stückzahl Nombre	Quantity / Unit Menge / Einheit Quantité / Unité	
1	5	564513-005	6,00 X 1500 X 3000 mm	1	212 KG	

Chemical composition – Chemische Zusammensetzung – Composition chimiques

	C	Si	Mn	P	S	Cr	Ni	Mo	Cu	N
Heat	.012	.37	.81	.031	.001	24.94	6.88	3.79	.28	.283

Radioactive contamination check acc. IAEA recommendations: Approved

Test results – Prüfergebnisse – Results dessais (1N/mm² = 1 MPa) F = Front – Anfan – Debut B = Back – Ende – Fin T = Transverse – Quer – Travers

	Test Ref		Temp °C	RP 0.2 N/MM2	RP 1.0 N/MM2	RM N/MM2	A5 %	2" %	HB HB	FEH %
Min			+20	550		795	20	15		
Max						1000			310	
	F	T	+20	697	778	890	34	34	274	46.0
	B	T		691	775	891	33	33	274	50.0

Corrosion acc. EN ISO 3651-2C: Approved
PREN: Cr + 3,3Mo + 16N = 42
Heat treatment / Solution annealed: Material temp minimum 1040 °C / Quenched (forced air + water)
Steel grade verification (PMI-spectroscopic): Approved
Marking, visual insp. and gauge measurement: Approved
Certified acc. Pressure Equipment Directive (2014/68/EU) by TÜV CERT-Certification body
for pressure equipment of the TÜV NORD Systems; notified body, reg-no. 0045.
Microstructure acc to ASTM A 923-A: Approved

Outokumpu Stainless AB
Business Area Europe
AVESTA WORKS
SWEDEN
Regoffice: Stockholm SWEDEN, Regno. 556001-8748

Telephone: + 46 (0)226 811 73
Fax: + 46 (0)226 816 46
V.AT no: SE556001874801

This material is found to comply with order requirements

Joakim Johansson
Authorized Inspector

C Welding parameters

Manual TIG (GTAW) welding used Zeron 100X filler wire material with a diameter of 2.4 mm, batch no. U2TG17100, produced by Metrode Products Ltd. Argon 5.0 was used as shielding gas, the gas speed was 15 L min^{-1}, the internal gas nozzle diameter was 12 mm, and the electrode used was a 2.4 mm type red electrode. Ceramic backing tape was also used. The welding parameters for each part of the weld are shown in Table C.1 where "1st filler" corresponds to the passes on both sides of the root and "2nd filler" corresponds to the cap, which in total amount to four passes.

Pass	Current [A]	Voltage [V]	Welding speed [mm s^{-1}]	Wire consumption [m min^{-1}]	Heat input [kJ mm^{-1}]
Root	90	10.05	1.1922	0.0771	0.7583
1st filler	120	11.200	1.4288	0.1443	0.9409
2nd filler	160	13.375	1.9486	0.2435	1.1008

Table C.1: Welding parameters during manual TIG welding of samples.

D XPS

Figure D.1 shows the relative atomic percent as a function of sputtering time of Fe, Cr and O found in the base material, HAZ and weld of TIG-welded pickled and not pickled samples obtained through XPS.
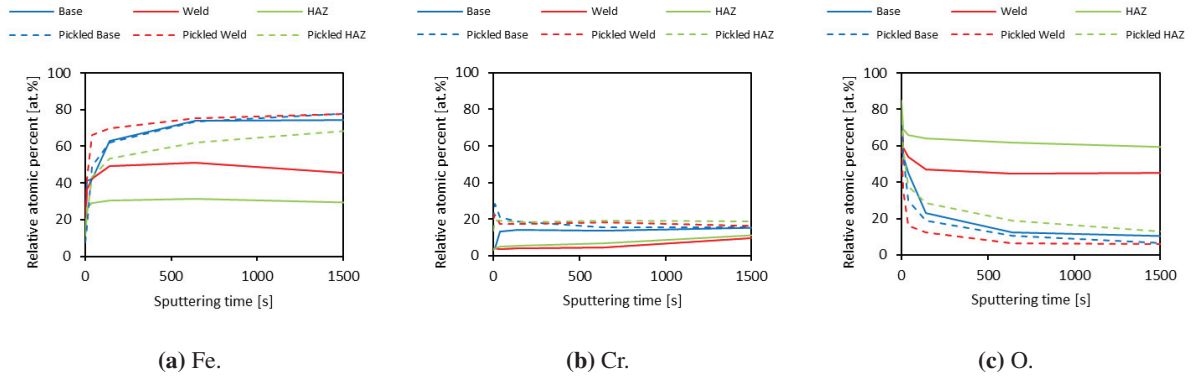

(a) Fe. **(b)** Cr. **(c)** O.

Figure D.1: Relative atomic percent of each element (Fe, Cr and O) as a function of sputtering time, expressed in seconds, in the base material, HAZ and weld of TIG-welded pickled and not pickled samples when sputtering the sample surfaces.

Alejandra Cristina Rueda Urdaneta

Critical temperature of welded 25Cr duplex stainless steel in seawater

NTNU
Norwegian University of
Science and Technology